Numerical Simulation of Oblique Droplet Impact onto a Deep Liquid Pool

by

Bo Liu

Submitted in fulfillment of the degree of

Master of Science

in Mechanical Engineering
Report number: 2841

Delft University of Technology
Faculty of Mechanical, Maritime and Materials Engineering

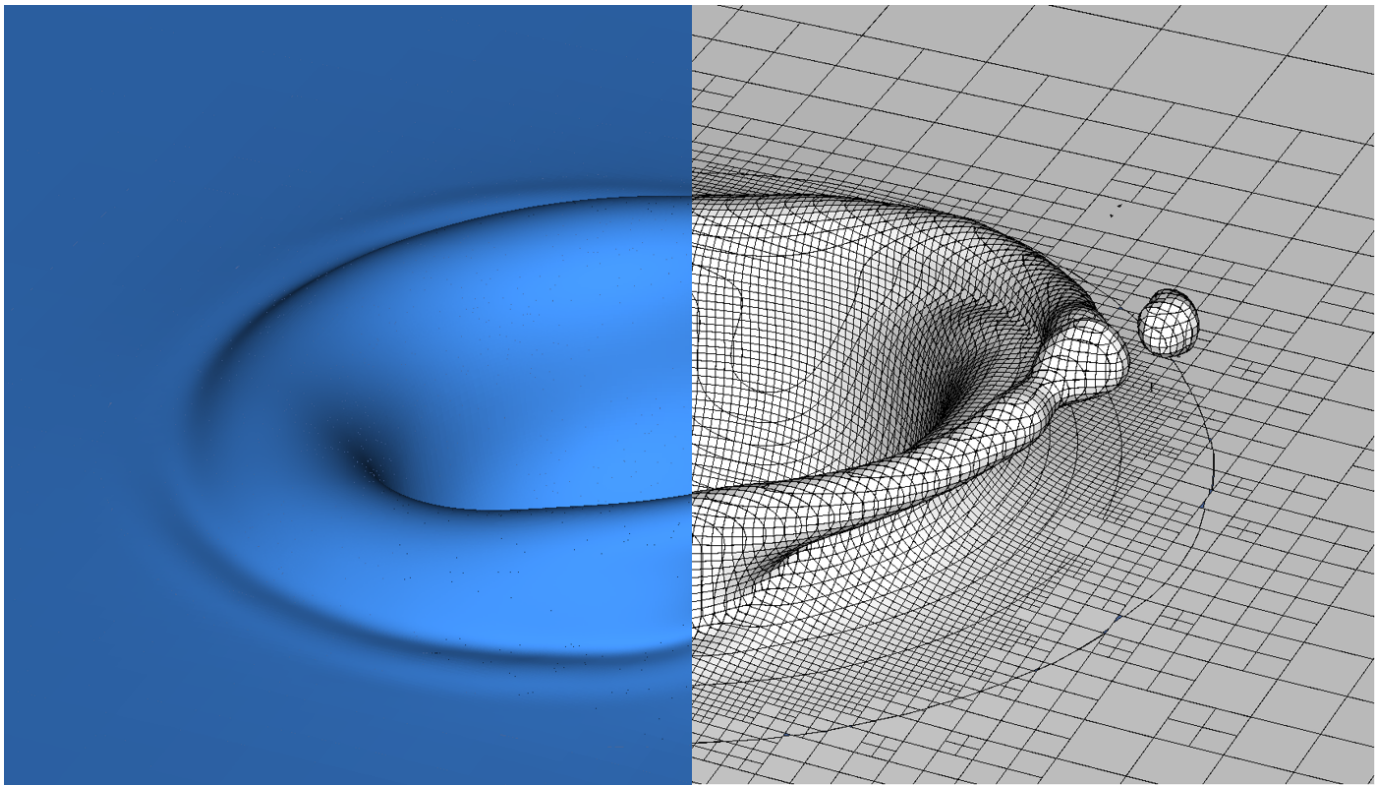

Supervisors:
MSc S. A. Reijers
Dr. ir. H. Gelderblom
Dr. ir. W.P. Breugem

Committee:
Prof. dr. ir. C. Poelma
Dr. ir. W.P. Breugem
Dr. ir. H.B. Eral
MSc S. A. Reijers
Dr. ir. G.H. Keetels

Abstract

Oblique impact of droplet onto a deep liquid pool is frequently observed in nature. As for engineering applications, the subsequent phenomenon of oblique droplet impact is of great significance for a proper design of the vanes in the extreme ultraviolet (EUV) chamber of ASML to prevent contamination. During the impact, the pool surface deforms and a cavity is generated, which later on collapses into a jet that shoots upward. Meanwhile, a liquid crown will be visible above the surface. When this crown becomes unstable, splashing occurs. We study these phenomena numerically by using fully three-dimensional simulation in Basilisk C, an open source CFD package, coupled with an adaptive Cartesian grid and volume-of-fluid (VOF) method. The simulation is validated by both qualitative and quantitative comparison with the available experimental results and theory. In both simulation and experiment, three types of impact phenomena are identified: smooth coalescence of droplet with the pool, splashing in the impact direction only, and splashing in all directions. We quantify these three regimes by accounting for the Weber number and the droplet impingement angle, and compare the results with the experimental data and scaling argument proposed in the previous literature. We also study cavity dynamics and shape. The growth of the cavity angle is captured by our simulation. In analogy to the perpendicular drop impact, we give a model for the cavity expansion, from which we obtain a temporal function for the cavity depth which is in agreement with the simulation. The magnitude of the cavity depth and the displacement match with the available experimental data. Besides, our simulation captures the scaling dependence of both the depth and the displacement on the Weber number. We further point out the connection between the descent of the crown and the initiation the cavity collapse.The three-dimensional details about the crown behavior and cavity formation from our simulation provide an insight of the phenomena which could cause contamination in the EUV chamber, and offer an opportunity for a further research on this subject.

Contents

CHAPTER 1

Introduction

1.1 Motivation

Oblique droplet impact is frequently encountered in daily life. The subsequent phenomenon is of great significance for both nature and industrial applications. During rain, for example, droplet impact onto puddles could trigger air entrainment, which accounts for the global vapor/liquid exchange [6]. In agriculture, the uptake efficiency of nutrients on the surface of plants is affected by droplet impact and the consequent splashing when spraying the pesticides on the field [7]. In industrial applications, the study of oblique impact can benefit e.g. oil spills, spray cooling, ink-jet printing, and forensic analysis [8–10, 45].

The study of the phenomena involved in the droplet impact could be traced back to the pioneering work of Worthington in [21]. Over the last century, this subject continues to attract the researchers around the different disciplines. Perpendicular droplet impact onto different substrates has been discussed in [21–54]. The impact phenomenon is mainly characterized by the Weber number $We = \frac{\rho_l D U^2}{\gamma}$ and the Reynolds number $Re = \frac{\rho_l U D}{\mu_l}$ with the droplet diameter D, droplet velocity U, surface tension γ, liquid density ρ_l and liquid dynamics viscosity μ_l. Gravity-related effects on the impact are defined by the Froude number $Fr = \frac{U^2}{gD}$ or by the Bond number $Bo = \frac{\rho_l g D^2}{\gamma}$ with gravitational acceleration g. A typical phenomenon of perpendicular droplet impact onto a pool is presented in Fig. 1.1. As shown in Fig. 1.1a, a cavity is visible below the surface [21, 22, 29, 51, 53, 54]. Meanwhile, an axisymmetric crown is developed above the surface [21, 22, 29, 51, 53], see Fig. 1.1b. The splashing threshold upon this crown has been discussed in [43, 44, 48, 54, 71], which has a standard form of $Re^{x_1} We^{x_2} = K$, with characteristic constants x_1, x_2 and a constant K whose value depends on the experimental environment, e.g. the surrounding vapor pressure. The capillary waves traveling along the cavity surface [29, 31, 51] (Fig. 1.1c) collapse at the cavity bottom, which could lead to an upward jet and the pinch-off of drops [29, 51, 71], see Fig. 1.1d.

The droplet impact onto a pool is also encountered in the Extreme Ultraviolet (EUV) chamber of ASML. Always regarded as an epoch-making lithography technology, Extreme Ultraviolet Lithography (EUVL) has been introduced into the semiconductor industry recently, and ASML is the primary EUVL maker [3]. Fig. 1.3 shows a sketch of the EUV source chamber from ASML [4]. To produce a hot dense plasma which accounts for the multi-charged ions and the consequent EUV light, a microscopic droplet made of molten tin is produced by the droplet generator on the top of the chamber. When the droplet falls, a laser beam impacts on the tin, followed by a violent phenomenon such as droplet deformation, fragmentation and splashing. As a consequence, the splatter droplets could flee to the collector mirror and the intermediate focus. This unwanted phenomenon puts forward a challenging problem to prevent the contamination at the inside surface of the chamber. One solution is to add some internal vanes whose geometry is specially designed to capture the splashing droplets. The initial splashing would cover the surface of the vanes, forming a liquid film on which the later splashing droplets will impinge. This film can be regarded as a deep liquid pool as compared to the splashing droplets (film thickness $\delta > 10D$). Besides, the splashing drops could impact on the catcher (at the chamber bottom presented in Fig. 1.3), which is a container filled with liquid tin. Hence the phenomena following droplet impact on a pool, e.g. ejection of a liquid crown which could cause a widespread contamination should be taken into account. Given that complicated flow inside the chamber and the uncontrolled directions of splashing after the laser impact, the droplets always approach the pool with the velocity non-

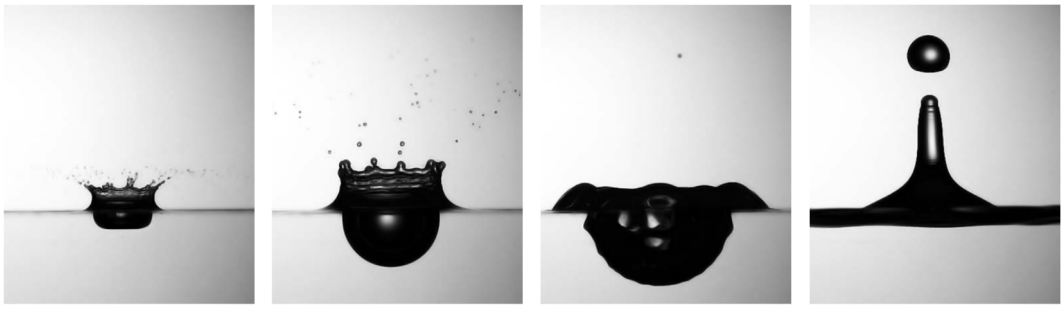

Figure 1.1: Photograph of perpendicular droplet impact onto a liquid pool. The image is taken from [29]. The snapshots are presented in chronological order. During the impact, we can observe an axisymmetric crown. In the case presented the crown destabilizes and breaks into splashing. Meanwhile, the impact leads to a cavity below the surface. The collapse of the cavity could result in an upward-jet above the water surface.

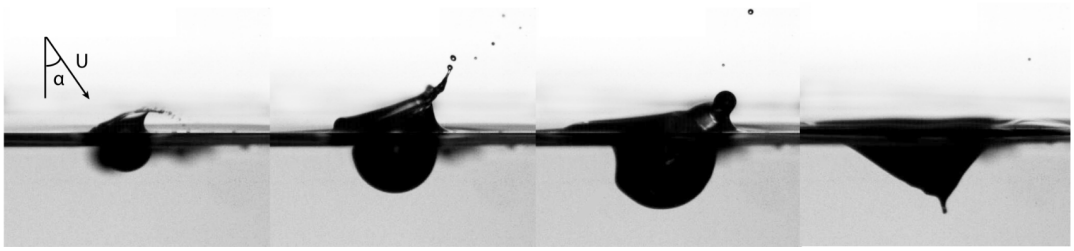

Figure 1.2: Photograph of oblique droplet impact onto a liquid pool. The snapshots are presented in chronological order from left to right. The image is taken from [71]. A droplet approaches a pool with a velocity U and an impingement angle α. In contrast to perpendicular impact, we observe asymmetric phenomena both for the cavity formation and the splashing.

perpendicular to the surface, i.e. oblique impact. In contrast to the perpendicular impingement, an asymmetric crown and splashing are visible in oblique impact, see Fig. 1.2. These asymmetric phenomena increase the uncertainty of the contamination. Therefore, ASML has a direct interest on the physical principal behind oblique droplet impact onto a pool to make an intelligent design for the geometry of the vanes.

Only few papers have dealt with oblique impact [11–13, 71, 80, 85]. In [85] the consequent crown behavior of oblique droplet impact onto a pool has been studied experimentally for different impact angles and Weber numbers. However, given the small range of $We \in [15, 249]$, the droplet always coalesces with the pool, hence no splashing appears. The first experimental study on the splashing threshold for this subject is done by Gielen et al. [71], in which water droplets with $D \approx 100\mu m$ are produced and approach a water surface. Given that $Fr \sim 10^5$ and $Bo \sim 10^{-3}$, the gravity is neglected in the experiments. From [71] three distinct types of crown behavior: deposition, single-sided splashing and omni-directional splashing are identified for $We \in [40, 1056]$ and $\alpha \in [0°, 80°]$. A model is developed in [71] to explain the threshold quantified by the experimental data. Also, Gielen et al. pointed out that cavity formation and the subsequent geometry when the capillary waves collapse is directly associated with the upward jet, which could account for the contamination in the EUV chamber. An energy argument is then proposed in [71] and concluded by a scaling law between the cavity dimensions and the Weber number. To extend the research on oblique impact, numerical simulations are required. Ray et al. [80] provide a description of the crown height and the geometry of the cavity. However, their work is performed in a two-dimensional domain to reduce the computational cost. Hence the simulation in [80] is incapable of an accurate description of the impact when a more sophisticated interface appears, e.g. crown splashing. Although there are several simulations discussing oblique droplet impact on a thin film [11–13], there is no fully three-dimensional numerical study of oblique droplet impact on a pool.

1.2 Goal and Outline

Here, we present a numerical study of oblique droplet impact onto a deep liquid pool in a three-dimensional domain. We simulate a spherical droplet with $We \in [187.5, 1400]$ that impacts a liquid pool consisting of the same liquid. The impact angle ranges from 0° to 75°. In line with the experimental setting of [71] where $Fr \gg 1$ and $Bo \ll 1$, we disable the

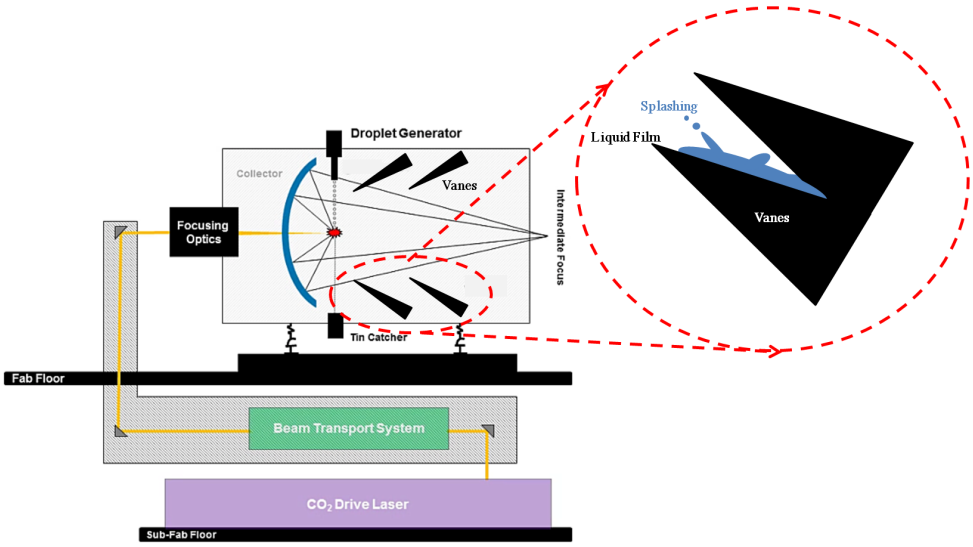

Figure 1.3: Sketch of Extreme Ultraviolet Lithography source chamber. The image is taken from [4] and modified. A small tin droplet is produced by the drop generator on the top of the chamber. Then a laser beam is projected on this droplet, inducing EUV light. Accompanying this process is a violent behavior of the droplet such as deformation and splashing. Several vanes are added to prevent the contamination on the collector and the intermediate focus. The initial splashing will coat the vanes, leading to a liquid film on the surface. This film can be regarded as a deep liquid pool for the splashing droplets impact on the vanes.

gravity in the simulation. We assess the feasibility of Basilisk C, an open source CFD package adopted in the present study to simulate a droplet. For a proper design of the vanes, one needs to understand the primary source of the contamination in the EUV chamber, i.e. the splashing occurrence in the crown and the upward jet due to the collapse of the cavity. To answer these questions, we focus on the crown behavior in order to capture the splashing threshold theoretically proposed in [71]. By using a three-dimensional setting, we attempt to make an accurate judgment on the splashing occurrence, which has been complicated in the experiment by, for instance, the observation plane taken by the camera. Besides, we will quantify the cavity formation (i.e. the cavity angle, the depth and displacement of the cavity) at the collapse moment, taking into account the importance of the cavity geometry to the upward jet. To validate our simulation, we make both quantitative and qualitative comparisons between the numerical results and the phenomena experimentally observed in [71]. In addition, our simulation provides additional three-dimensional information about the crown and the cavity such as the initiation process of cavity collapse, and offers the opportunity to explore a broader parameter regime.

The thesis is organized as follows. In chapter 2, we provide the theoretical background of oblique impact using literature review. Furthermore, we discuss two auxiliary problems in the regime of capillary flow: perpendicular droplet impact onto a pool/solid-substrate. These two cases are used as validations for the numerical methods we used. In chapter 3, we mainly describe Basilisk C, which offers a C-like programming environment for writing discretisation schemes on an adaptive Cartesian grid [1,2]. We will present the volume-of-fluid (VOF) method, the mesh configuration and the Navier-Stokes solver used in this work. To estimate the CPU time and the memory we potentially request, this chapter will be concluded by a scalability analysis of Basilisk when simulating a droplet impact in a three-dimensional domain. In chapter 4, we present the numerical results of two validations as discussed in chapter 2. Based on the comparison between the data in this chapter and the literature referred to in § 2.1 and § 2.2, we will estimate the capability of Basilisk to handle the droplet impact problem. In chapter 5, we provide details of the simulation with oblique droplet impact on a liquid pool and the comparison with the experiments in [71]. We introduce the computational setting of a three-dimensional domain in § 5.1. The impact angle and the Weber number are varied systematically to capture the typical crown behavior and the splashing threshold, see § 5.2. The evolution of the cavity angle will be discussed in § 5.3. We will discuss the cavity dimensions in § 5.4. Finally, we summarize the findings of our study and give recommendations for further research.

CHAPTER 2

Theoretical Background

In this chapter, we provide theoretical background we will use to interpret the numerical results in chapter 4 and chapter 5. We carry out two validations to support our numerical methods. In § 2.1 we present the scaling analysis for a perpendicular droplet impact on a solid substrate. We primarily focus on the spreading process and the maximum spreading diameter. Then we give a description of perpendicular droplet impact onto a liquid pool in § 2.2. The theoretical models and the literature referred to in § 2.1 and § 2.2 will be compared with the numerical validations in chapter 4.

The primary subject of our study is oblique droplet impact onto a liquid pool. We will discuss the characteristic phenomena of this problem in § 2.3. By using an energy argument, scaling laws for the cavity dimensions are obtained (§ 2.3.1), which will be validated in chapter 5. Besides, we will discuss the splashing threshold in § 2.3.2 and focus on the model developed by Gielen et al. [71].

2.1 Perpendicular Droplet Impact onto a Solid Substrate

We start this chapter with the discussion of normal droplet impact on a solid substrate. Although the phenomena can seem diverse with different properties of the substrate and the involved liquid, this process can always be defined by the competition between the inertial force, gravity, surface tension, and the viscous force [23]. After the impact on the substrate, the droplet will radially spread, driven by its initial kinetic energy and the surface properties (e.g. the contact angle). Later on, the droplet can deposit, bounce or splash depending on the kinetic energy and the wetting properties of the substrate [23]. Here we give a description of the maximum spreading diameter based on an energy argument.

2.1.1 Maximum Spreading Diameter

The spreading process is schematically shown in Fig. 2.1. Due to the surface tension and the energy dissipated by the viscosity, this spreading will slow down, reaching a maximum diameter D_m in final [23,32]. This outcome can be defined by several relevant parameters.

As presented in Fig. 2.1, a droplet with a diameter D approaches the solid wall with a velocity U, under the influence of the gravity g. Here ρ_l, ρ_g, μ_l and μ_g stand for the density and the dynamic viscosity for the liquid and surrounding vapor respectively. We use γ to present the surface tension of this vapor-liquid system. The variables mentioned above can be expressed by three independent physical units, i.e., m, s, kg. According to the Buckingham π theorem, the maximum spreading ratio $D^* = D_m/D$ could be defined by a function with five non-dimensional numbers constructed from the above physical parameters. In the problem considered in this work, we neglect any contribution from the vapor phase since the density ratio $\rho_l/\rho_g \sim 1000$ and the viscosity ratio $\mu_l/\mu_g \sim 100$. Furthermore, the negligible effect from gravity on this problem has been validated given that $Fr \gg 1$ [23]. Therefore, only two parameters are relevant in this case.

We expect that the spreading ratio D^* is a sole function of

$$D^* = f(Re, We), \tag{2.1}$$

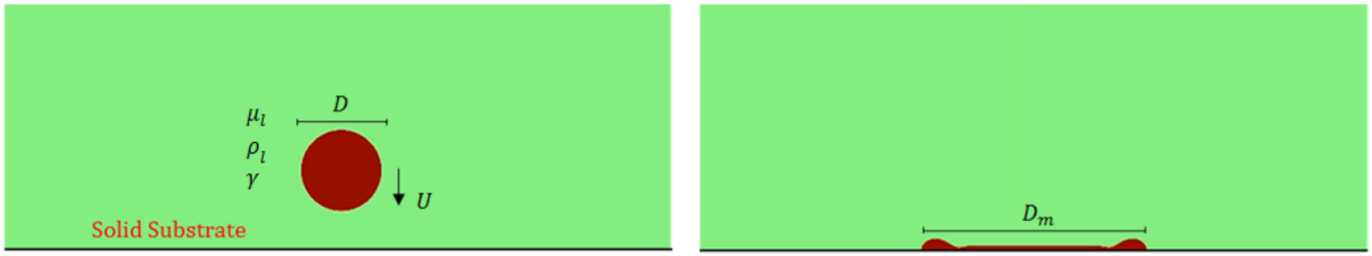

Figure 2.1: A schematic sketch of droplet impact on the solid bottom. **Left:** A droplet having a diameter D approaches the wall with a vertical velocity U. **Right:** The droplet will have a radial spreading after the contact with the solid bottom. Due to the surface tension effect and the viscous dissipation, the spreading process will slow down. The droplet will finally reach a maximum spreading diameter D_m.

where

$$Re = \frac{\rho_l U D}{\mu_l} \quad \text{and} \quad We = \frac{\rho_l U^2 D}{\gamma} \tag{2.2}$$

are the impact Reynolds number and Weber number. Quite a few models have been established based on the energy balance between the inertial force with the surface tension or the viscosity [23,25,33–35]. The transition between these two regimes are defined by the impact number $P = \frac{We}{Re^{4/5}} \approx 1$ [25]. When $P \ll 1$ the spreading process is dominated by the competition between the inertial force and the surface tension, hence, the Weber number. The relation between the spreading ratio D^* and the Weber number can be obtained by assuming that all the initial kinetic energy of droplet is transferred into the surface energy:

$$\rho_l U^2 D^3 \sim \gamma D_m^2, \tag{2.3}$$

which leads to

$$D^* \sim We^{1/2}. \tag{2.4}$$

This energy argument offers a straight-forward analysis of the impact problem. However, the presence of the viscous dissipation for this regime would lower the validity of (2.4). Furthermore, a correction accounting for the initial surface of the droplet, which could be comparable to the spreading area for small Weber numbers, is not considered in (2.4) [23].

When the Weber number increases, the impact process will shift into a regime where viscosity dominates ($P \gg 1$). A model then has been established in [33] which includes the boundary layer dissipation and the retraction of the rim, leading to a semi-empirical formulation:

$$D^* \sim 0.87 Re^{1/5} - 0.4 P^{-1/2}. \tag{2.5}$$

With a large Weber number, (2.5) can be reduced to $D^* \sim Re^{1/5}$. Using the similar approach, a formulation in both regimes

$$D^* \sim Re^{1/5} f(P), \tag{2.6}$$

has been presented in [35]. Besides the non-dimensional numbers mentioned above, the effect of the contact angle on the expansion process was studied. Wildeman et al. [32] researched on the energy balance in the expansion process by using an open source solver Gerris [2]. In their study, the static contact angle is assumed to equal the dynamic angle during the simulation. This research is concluded with the formulation describing the expansion ratio under the different bottom conditions. For a free-slip substrate,

$$D^*(We, \theta) = \sqrt{\frac{4}{1-\cos\theta}\left(\frac{We}{24} + 1\right)} \quad (We > 30), \tag{2.7}$$

while for the no-slip bottom,

$$\frac{3(1-\cos\theta)}{We} D^{*2} + \frac{\beta}{\sqrt{Re}} D^{*2}\sqrt{D^* - 1} = \frac{12}{We} + 0.5 \quad (We > 30), \tag{2.8}$$

where β is a fitting parameter and is determined as $\beta \approx 0.7$ in [32]. The value of β can also be estimated by comparing (2.8) with (2.5) at $We \to \infty$, which leads to $(2\beta)^{-2/5} \approx 0.87$ and $\beta \approx 0.708$.

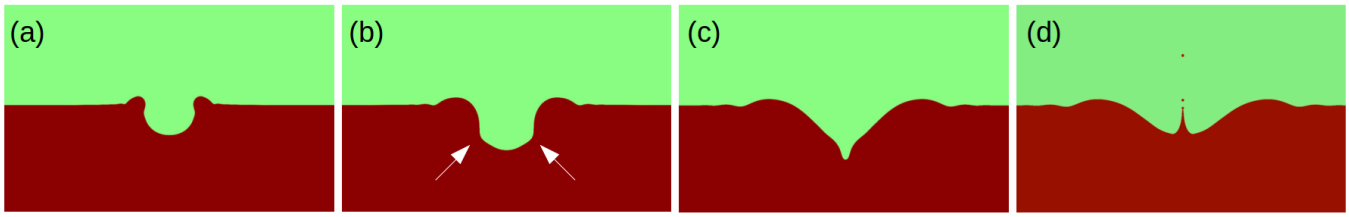

Figure 2.2: Temporal evolution of a droplet impact on a liquid pool. $D = 0.04, U = 1, We = 150, Re = 1000, Fr = \infty$. At the initial time, a droplet is set with the distance of $0.1D$ between the pool level. **(a):** Once contact with the target liquid, a radial expanding crown with its height h_{crown} (Fig. 2.4) is generated. **(b):** Later a capillary wave (highlighted by arrows) will be developed along the peripheral rim, traveling to the cavity bottom. **(c):** During this period an explicit deformation of the cavity shape can be observed, from spherical to a cone shape. The capillary waves will collapse at the bottom of the cavity. **(d):** Later on, a high-speed jet is formed at the center axis. Notice that the break-droplets are visible in the given condition.

2.2 Perpendicular Droplet Impact onto a Liquid Pool

The perpendicular droplet impact onto a pool has been discussed in several papers in terms of experimental studies [21, 26–29, 43–45, 48] and numerical simulations [37, 45]. By using an energy argument, this problem can be described by a dimensionless group including Weber, Froude and Reynolds number. A consensus exists that in most of the experimental cases the effect of viscosity is negligibly small with a large Reynolds number, then the problem could be completely defined by using Weber and the Froude number alone [29]. A temporal evolution of a droplet impinging on a liquid pool is presented in Fig. 2.2. A spherical droplet with diameter D is put above the pool. The droplet is then approaching the pool with a perpendicular velocity U. The impact will produce an expanding, nearly spherical cavity underneath the pool level. Meanwhile, a growing crown above the pool surface around the impact point will be created with a crown height h_{crown}. If the impact velocity is large enough, this crown will present a lid-like shape [21, 29], see Fig. 2.3. Then the crown falls and generates a capillary wave traveling from the peripheral rim to the bottom of the cavity. During this period, the cavity will deform to a cone shape. Later on, the capillary waves will collapse at the bottom of the crater, followed by a retraction of the cavity. The surface energy stored accounting for the deformation of the cavity will then be converted into the kinetic energy during the collapse, leading to high-speed jet. Note that with the parameters in Fig. 2.2, this jet breaks into several droplets.

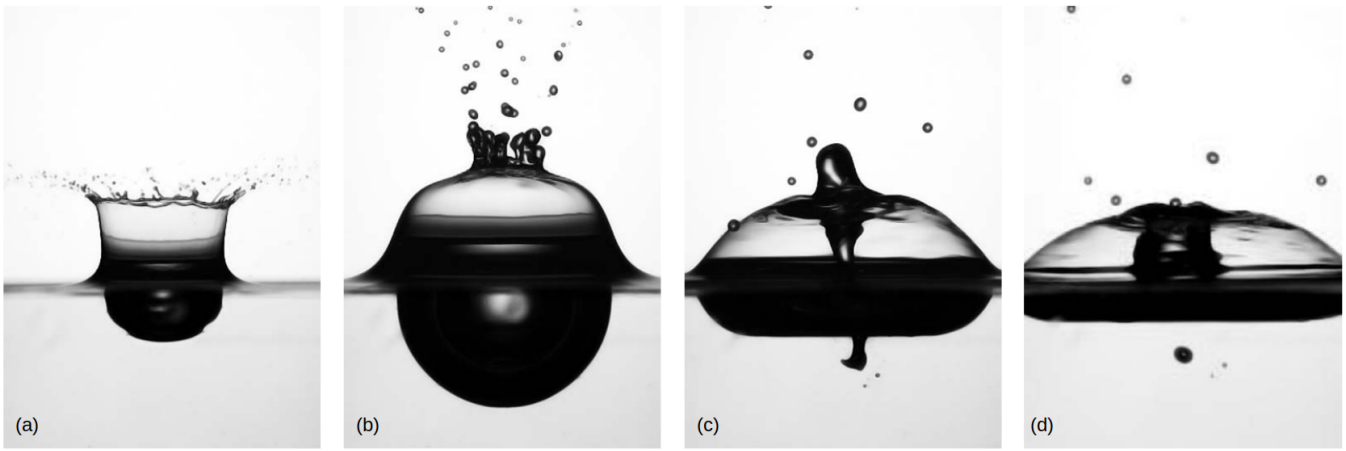

Figure 2.3: The lid-shaped crown above the pool surface after a perpendicular droplet impact on a pool. Image is taken from [29]. Impact parameter are: $D = 2.9mm, U = 4.4m/s, We = 2177, Fr = 691, Re = 12642$. The snapshots are presented in a time sequence from panel (a) to panel (d).

2.2.1 Maximum Cavity Depth

We primarily focus on the maximum depth of the cavity h_m, which is shown in the Fig. 2.4. In contrast to the droplet impact onto a solid substrate, the gravity could play an important role in the formation of the cavity. During the growth of the crater, the kinetic energy of the droplet can be converted into the increased surface energy or the gravitational potential. A non-dimensional number $Bo = \frac{We}{Fr} = \frac{\rho_l D^2 g}{\gamma}$, referred to as Bond number, discriminates the transition between the different regimes [27, 28]. When $Bo \gg 1$, the gravitational potential E_p is the primary receiver of the kinetic energy. By assuming that the impact cavity is approximately hemispherical and is centered at the impact point, the scaling of this potential energy has

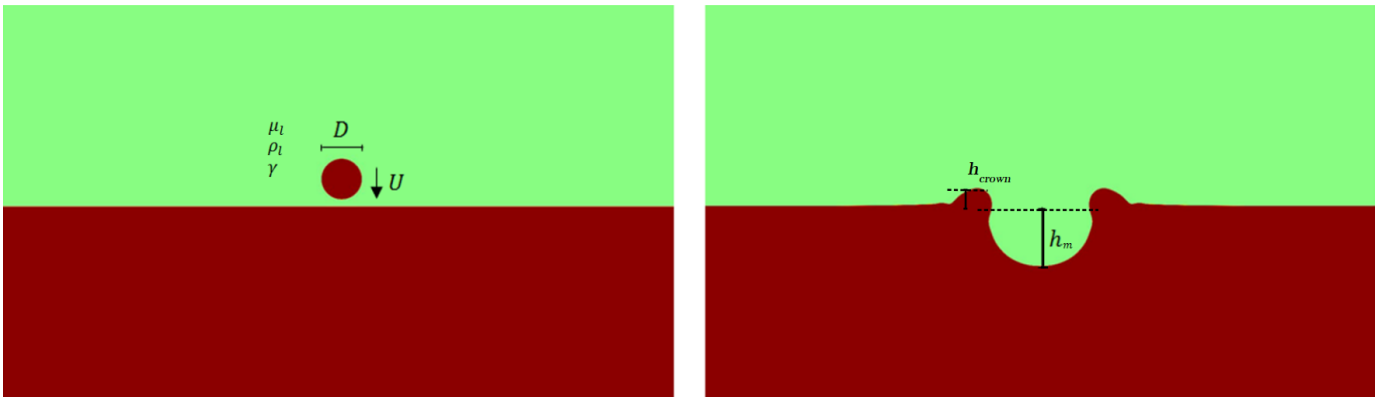

Figure 2.4: Schematically plot of maximum cavity depth h_m for a droplet impact on a liquid pool. **Left:** The droplet with a diameter D and density ρ_l approaches the liquid pool with a velocity U normal to the pool surface. We use γ to indicate the surface tension. **Right:** After the impact a hemispherical crater cavity is generated below the pool level. Its geometric property is defined by the depth of the cavity. Meanwhile, a crown with its height h_{crown} is produced above the surface. In the present work the cavity depth is the distance between the deepest point of the cavity and the initial pool surface. Due to the surface tension, the cavity reaches a maximum depth h_m, which is followed by the cavity retraction.

been deduced in [22], given by

$$E_p \sim \rho_l g h_m^4. \tag{2.9}$$

When $Bo \ll 1$, the balance between the kinetic energy and the increased cavity surface will define the depth of the cavity. The scaling of this increased surface energy

$$E_\gamma \sim \gamma h_m^2 \tag{2.10}$$

is also offered in [22]. Remembering that in the problem considered in our work, gravity is neglected, then it is fair to assume that all the initial kinetic energy is converted into the growing surface energy, leading to

$$\rho_l U^2 D^3 \sim \gamma h_m^2. \tag{2.11}$$

From (2.11) we obtain the dependence of the maximum cavity depth h_m on the Weber number

$$\frac{h_m}{D} \sim We^{1/2}. \tag{2.12}$$

We emphasize that viscosity is absent in scaling (2.12), which is reliable when the surface tension overmatches against viscosity and dominates the cavity formation. While as surface tension decreases, the viscous dissipation could come into play and lower the validity of (2.12). This viscosity-effect will be discussed in § 4.2.

2.2.2 Splashing Threshold: Perpendicular Droplet Impact onto a Pool

One of the purposes of our simulation is to capture the splashing behavior of the crown. Therefore, we will present a scaling argument for the splashing threshold, and we start our discussion with the perpendicular impact. Although many studies have dealt with the splashing occurrence when the droplet hits on a dry surface or a liquid film, a liquid pool as a substrate can only be found in few papers [44, 45, 47, 48, 71] in which inertial force is much stronger than gravity, that is, $Fr \gg 1$. Typically, the splashing threshold can be regarded as a mathematical expression to discriminate between the different crown behavior [44]. Most of the models select a group of non-dimensional parameters, including Weber number and Reynolds number to form a threshold

$$We^{x_1} \cdot Re^{x_2} = K, \tag{2.13}$$

considering a negligibly small effect from gravity. In (2.13) x_1, x_2 are the characteristic constants, and K stands for the critical number of splashing [44, 45, 47, 48, 71]. Given different experimental conditions and the definition of splashing, model constants vary from each other. The values of x_1, x_2 and K for different models are listed in Table 2.1.

Among the approaches to get (2.13), Huang et al. [48], Zhao et al. [44] and Mundo [43] came up with their models based on experimental observations. An effort made by Gielen et al. [71] focuses on the competition between the crown velocity V and the capillary retraction Taylor-Culick velocity V_{TC}, by which the crown behavior is characterized. In analogy

Table 2.1: The parameter in (2.13) describing splash threshold. These models are applicable in perpendicular droplet impact onto a deep liquid pool.

Ref.	x_1	x_2	K
Huang & Zhang [48]	0.375	0.25	70
Zhao et al. [44]	0.715	0.57	1707
Mundo et al. [43]	0.5	0.25	90
Gielen et al. [71]	0.5	0.25	130

to the threshold for the destabilization of a liquid sheet—which has been reported in several literatures [37, 81, 82]—Gielen et al. assume that the crown velocity should be larger than the Taylor-Culick velocity

$$\frac{V}{V_{TC}} > K, \tag{2.14}$$

in order to attain splashing, with $V_{TC} = \sqrt{\frac{2\gamma}{\rho_l e}}$ constructed by the thickness of the crown e [23, 71], see Fig. 2.5. The value of the splashing critical number K relies on the specific experimental conditions, e.g. categories of the substrates [23, 42, 43, 45, 71]. In the case of perpendicular impact on a liquid pool, Mundo et al. [43] point out $K \approx 90$ based on the experimental study. Gielen et al. [71] obtain $K \approx 130$ by measuring the critical Weber number for splashing. Inequality (2.14) indicates that the behavior of the crown is bounded by the balance between the kinetic energy and the resistance force (i.e. the capillary force and the viscosity). To quantify (2.14), a model aimed to describe the crown velocity is developed in [71]. As shown in Fig. 2.5, by assuming the mass of the droplet submerged into the pool is proportional to the volume of the crown

$$D^2 U \sim eDV, \tag{2.15}$$

a scaling of the crown velocity for the perpendicular impact is provided:

$$V \sim \frac{DU}{e}. \tag{2.16}$$

The description of e can be obtained by analogy with the ejecta sheet when the droplet hits on a liquid film. Josserand et al. [37] pointed out that e can be determined from the viscous boundary layer developed at the basis of the sheet, leading to a length scaling as a function of time t:

$$e(t) \sim \sqrt{\frac{\mu_l t}{\rho_l}}. \tag{2.17}$$

This outcome is in agreement with the experiments done by Thoroddsen [38]. Furthermore, it is observed in the experiments that the splash starts at the same time scale as the inertial time $t_i = D/U$ [71], leading to

$$t \sim \frac{U}{D}. \tag{2.18}$$

From eqs. (2.16) to (2.18) and the definition of V_{TC}, we get the splashing threshold for the perpendicular droplet impact on a pool

$$\frac{V}{V_{TC}} \sim We^{1/2} Re^{1/4} > K. \tag{2.19}$$

It is noteworthy that the mass conservation argument (2.15) between the droplet and the crown is valid only for $t < D/U$ [71]. At a later time a pronounced cavity will be produced, and the volume of the crown could be approximated as the volume of the cavity (instead of the droplet) [22].

2.3 Oblique Droplet Impact onto a Liquid Pool

In this section, we will show the characteristic phenomena of oblique impact, and discuss the fundamental principal behind the scaling laws we are about to present concerning the literature available. The theoretical aspect shown in this section will support the validity of the numerical results in chapter 5.

Fig. 2.6 provides an overview of oblique droplet impact on a liquid pool. We put a spherical droplet with diameter D above the pool surface. The droplet approaches the liquid pool with a velocity U and an impact angle α. Due to this oblique

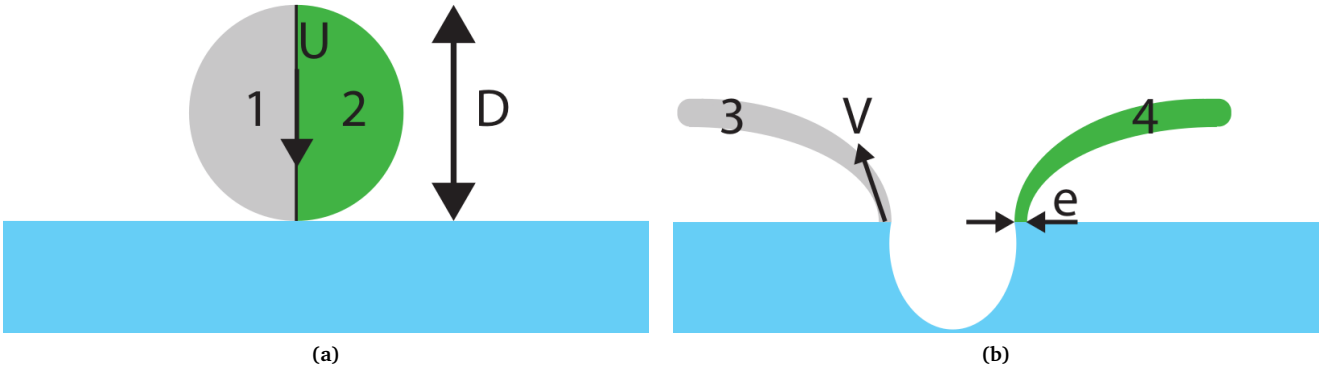

Figure 2.5: Schematic plot of mass distribution in the crown for perpendicular droplet impact onto a pool. The image is taken from [71]. **(a):** A droplet with diameter D and a vertical velocity U approaches a liquid pool. Volume 1 represents the original droplet which flows into the crown volume 3 (indicated in panel (b)). Volume 2 indicates the original droplet that accounts for the crown volume 4 (indicated in panel (b)). **(b):** After the droplet contacts the pool, an axisymmetric crown with its thickness e at the crown basis is formed. The crown velocity V accounts for the flow across the crown basis.

angle, the droplet will possess not only a vertical velocity $U_\perp$, but also a component parallel to the surface $U_\parallel$. As illustrated in Fig. 2.6, these parameters are related by

$$U_\perp = U\cos\alpha, \quad U_\parallel = U\sin\alpha. \tag{2.20}$$

In contrast to the perpendicular case, we expect an asymmetric phenomenon for the oblique impact. In this work, we primarily focus on the cavity dynamics below the surface, and the asymmetric crown developed above the pool.

2.3.1 Cavity Dynamics

Fig. 2.7 shows the different stages of the cavity formation with $We = 200$ and $\alpha = 15°$. After the contact between the surface and the droplet, a cavity with a triangular cross section is developed below the pool surface, see panel (a). We use three parameters to define the cavity shape: the cavity depth h, the cavity displacement d and the corresponding cavity angle α_c. These three parameters are related by

$$\alpha_c = \begin{cases} \arctan\left(\frac{h}{d}\right), & \alpha_c < 90°, \\ 180 - \arctan\left(\frac{h}{d}\right), & \alpha_c > 90°. \end{cases} \tag{2.21}$$

The displacement d is denoted as the horizontal distance from the deepest point of the cavity to the center line, and h is the depth of this deepest point (see Fig. 2.6). At early stage as presented in panel (a) ($t^* = 0.8$ where $t^* = \frac{t}{D/U_\perp}$), the deepest point of the cavity directs toward the leading side, in contrast to its later direction shown in panel (e). When $t^* = 3.5$ (panel (b)), a hemisphere cavity is formed, and it continuously grows at $t^* = 7.2$, see panel (c). We capture a capillary wave traveling from the leading side toward the cavity bottom, which is indicated by an arrow in panel (c). At the later time $t^* = 16.6$, another capillary wave developed on the trailing side is visible, and the consequent crest is highlighted by an arrow in panel (d). These waves travel from the rim of the crown and collapse at the cavity bottom when $t^* = 25.8$ (panel (e)). We record the cavity displacement and the cavity angle at this collision moment, named d_m and α_{cm} respectively. In this period the cavity will deform from a hemisphere to a cone-shaped geometry. After the waves collapse, the cavity tip will retract rapidly due to the high local curvature, see panel (f) ($t^* = 29.1$). Depending on the energy conversion and the impact parameters, this retraction could lead to a Worthington jet [21, 71].

The time series shown in Fig. 2.7 indicates that the angle α_c will increase from zero to α_{cm} during the impact process. Ray et al. [80] concluded from their simulation that the angle α_{cm} is monotonically increasing to the impact angle α. Gielen et al. [71] observed

$$\alpha_{cm} \approx \alpha + 90° \quad (\alpha \lessapprox 30°), \tag{2.22}$$

in their experiments. When the impact angle α is approaching 90°, α_{cm} becomes increasingly smaller compared to α. Besides, Gielen et al. [71] point out that α_{cm} is closely related to the direction of Worthington jet as the cavity collapse, which leads to a widespread contamination in the EUV chamber when droplets impact on the vanes.

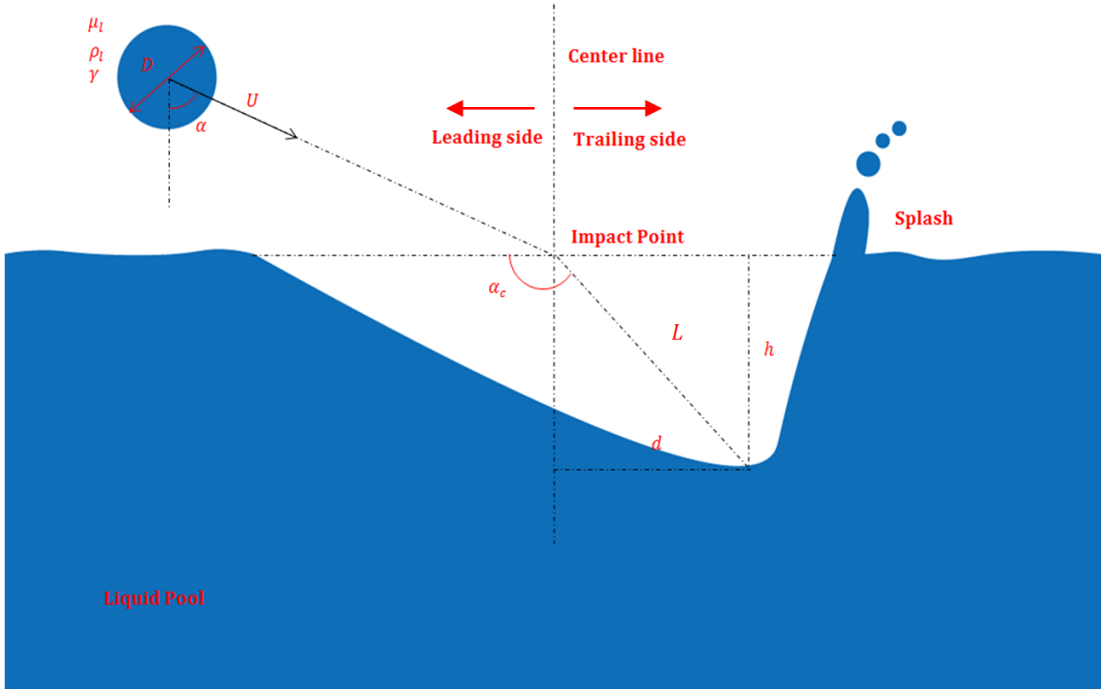

Figure 2.6: A sketch of oblique droplet impact onto a liquid pool. A droplet with diameter D moves toward the pool with an impact angle α. Its velocity is denoted as U. After the impact, an asymmetric cavity is visible below the pool surface. Three parameters are used to define the cavity geometry: the cavity depth h, displacement d, and the corresponding cavity angle α_c. Length L is the characteristic dimension of the cavity. The cavity angle can be determined by Eqn. (2.21). An asymmetric crown will be generated above the pool level, accompanied by a splash depending on the impact parameters. We divide the cavity and the crown into leading side and trailing side, separated by a perpendicular line going through the impact point (hereafter called center line). These two regions are highlighted by the arrows in the figure.

In addition, the analysis about d_m, i.e. the cavity displacement when the capillary waves collapse, is presented in [71]. Assuming that the droplet kinetic energy is converted to the additional surface energy, we can obtain an energy scaling:

$$\rho_l D^3 U^2 \sim \gamma L^2, \tag{2.23}$$

hence

$$\frac{L}{D} \sim We^{\frac{1}{2}}. \tag{2.24}$$

Here L is the characteristic length of the cavity, see Fig. 2.6, and it can be determined by $L = d_m/\sin(\alpha_{cm} - 90°)$. Combining this geometric expression of L with (2.22) we can get

$$\frac{L \cdot \sin(\alpha_{cm} - 90°)}{D} \sim We^{\frac{1}{2}} \sin\alpha, \tag{2.25}$$

and hence

$$\frac{d_m}{D} \sim We_{\parallel}^{1/2}, \tag{2.26}$$

where $We_{\parallel}^{1/2} = \frac{\rho_l U_{\parallel}^2 D}{\gamma}$. As for the maximum cavity depth, Gielen et al. [71] defined it as the crater depth when the capillary waves collapse, say $h_m^{'}$. Therefore this maximum depth can be presented as $h_m^{'} = L \cdot \cos(\alpha_{cm} - 90°)$. From (2.22) and (2.24) we can obtain

$$\frac{L \cdot \cos(\alpha_{cm} - 90°)}{D} \sim We^{\frac{1}{2}} \cos\alpha. \tag{2.27}$$

We introduce the Weber number with respect to the perpendicular momentum $We_{\perp}^{1/2} = \frac{\rho_l U_{\perp}^2 D}{\gamma}$, then (2.27) can be expressed as

$$\frac{h_m^{'}}{D} \sim We_{\perp}^{1/2}. \tag{2.28}$$

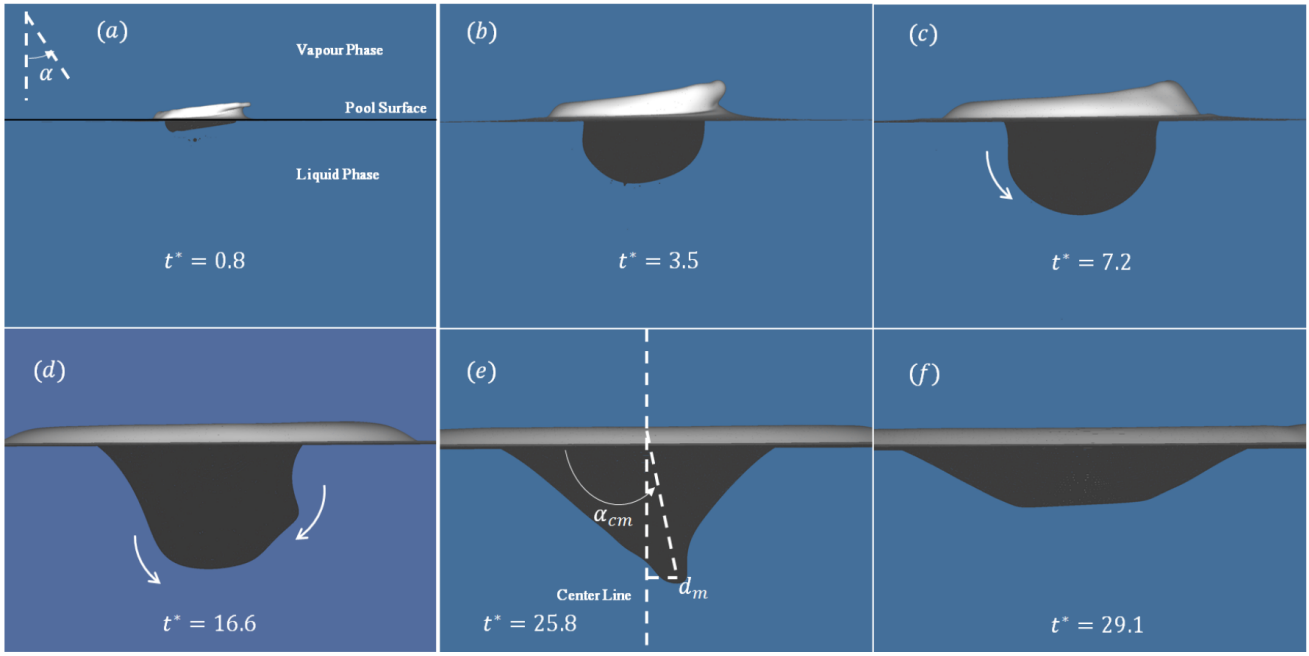

Figure 2.7: Numerical simulation of oblique droplet impact on a liquid pool, with $We = 200$ and an impact angle $\alpha = 15°$. The non-dimensional time t^* is given by $t^* = \frac{t}{D/U_\perp}$, and we denote $t^* = 0$ as the moment when the droplet contacts the pool. **(a):** The deepest point of the impact cavity is developed on the leading side, when $t^* = 0.8$. **(b):** At $t^* = 3.5$, the cavity and the crown are still growing. **(c):** Later on ($t^* = 7.2$) a capillary wave prolongates from the leading side of the crater, moving toward the bottom of the cavity. This process is indicated by a traveling crest, highlighted with an arrow. **(d):**A more pronounced capillary wave is visible, moving from the trailing side to the cavity bottom, at $t^* = 16.6$. **(e):** When $t^* = 25.8$, these capillary waves collapse at the bottom of the cavity with a horizontal distance with respect to the center line (as defined in Fig. 2.6). We measure the cavity displacement d_m and the angle α_{cm} at this moment. **(f):** Following the collision of the capillary waves is a rapid retraction of tip. When $t^* = 29.1$, an upward jet is developed with an ejection angle (not visible in the figure).

Scaling (2.28) provides an approximation for the vertical dimension of the cavity. In this work, the coordinate of the cavity bottom is recorded in each time step, among which we extract the maximum cavity depth h_m. In the simulation, we observe that $h_m \geqslant h_m^{'}$ with a small deviation ($< 3\%$ of h_m). In fact, in most of the cases the maximum depth is attained at the moment that the waves collapse, i.e. $h_m = h_m^{'}$. In line with (2.28), we propose

$$\frac{h_m}{D} \approx \frac{h_m^{'}}{D} \sim We_\perp^{1/2} \tag{2.29}$$

in our simulation.

2.3.2 Splashing Threshold: Oblique Droplet Impact onto a Pool

We now present a scaling argument of splashing threshold for oblique drop impact on a pool. Due to the parallel velocity $U_\parallel = U \sin\alpha$, the mass distribution among the crown will be asymmetric. Consequently, we should add a corrected term

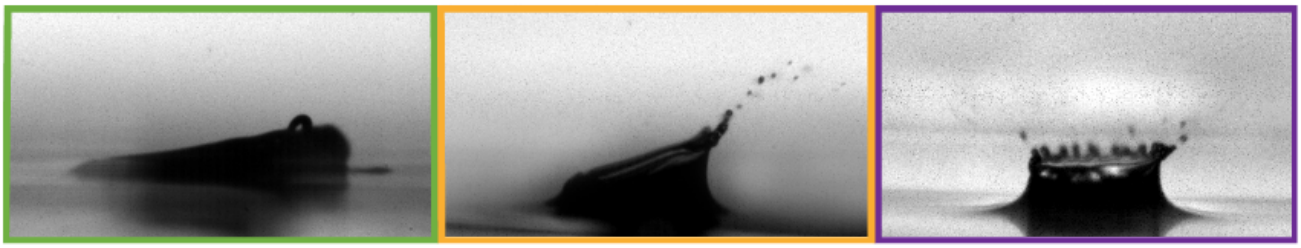

Figure 2.8: Three different categories of the splashing behavior (image is taken from [71]). **Green Frame:** deposition; **Yellow Frame:** single-side splash; **Purple Frame:** omni-direction splash.

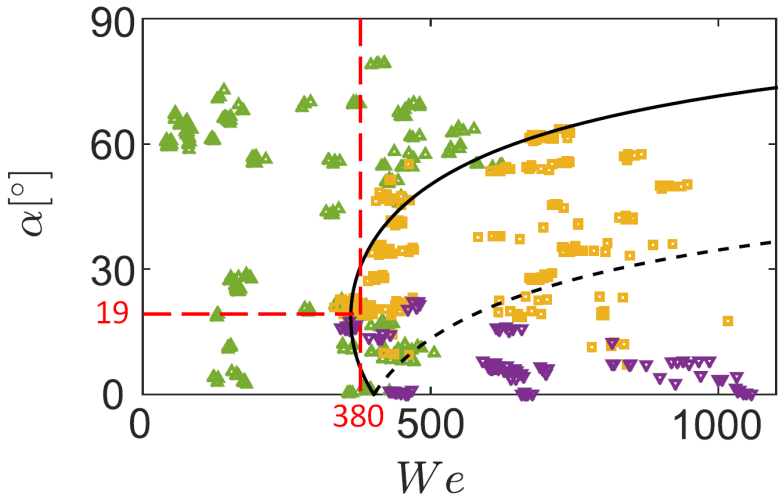

Figure 2.9: A phase diagram of the crown behavior plotted as a function of Weber number and the impact angle. The image is taken from [71]. The domain is divided into three regions: deposition crown, single-sided splashing, and omni-directional splashing. Eqn. (2.33) is presented by a solid line (with a plus sign in Eqn. (2.33)) which represents the transition from deposition to single-sided splashing, and a dashed line (with a minus sign in Eqn. (2.33)) indicating the threshold from single-sided to omni-directional splashing. When we increase the impact angle along $We = 380$, the crown destabilizes on the trailing side from deposition to single-sided splashing at first, and returns to deposition. This result is associated with the monotonic property of $f(\alpha)$ with respect to the trailing side, which obtains a maximum at $\alpha = 19°$ (see text). We plot symbols representing the experimental data: deposition (green upward triangle), single-sided splashing (yellow square) and omni-directional splashing (purple downward triangle). The experimental results are in agreement with the threshold (2.33) when describing the transition from deposition to single-sided splashing. However, an ambiguous boundary occurs in the experiment data when discriminating from single-sided to omni-directional splashing.

$f(\alpha)$ to (2.13) which accounts for the impact angle,

$$We^{x_1} Re^{x_2} f(\alpha) = K. \tag{2.30}$$

After the droplet hits on the surface, more liquid will be squeezed to the trailing side, resulting in a higher local crown velocity. By following the same mass conservation applied in the perpendicular impact, Gielen et al. [71] give a scaling of the volume flow for both leading side and trailing side:

$$eDV \sim \begin{cases} D^2 U_\perp (1 - c\frac{U_\parallel t}{D}), & \text{leading side;} \\ D^2 U_\perp (1 + c\frac{U_\parallel t}{D}), & \text{trailing side,} \end{cases} \tag{2.31}$$

where c is the fitting parameter, and its value depends on the way the mass redistributed around the crown [71]. Prefactor $D^2 U_\perp$ determines the total volume flows into the crown, and factor $(1 \pm c\frac{U_\parallel t}{D})$ accounts for the redistribution ratio of the liquid between the leading/trailing side. From (2.31) and the definition of Taylor-Culick velocity, we get a scaling of the crown velocity in the oblique impact case

$$\frac{V}{V_{TC}} \sim \begin{cases} We^{1/2} Re^{1/4} (\cos^{5/4}\alpha)(1 - c \cdot \tan\alpha), & \text{leading side;} \\ We^{1/2} Re^{1/4} (\cos^{5/4}\alpha)(1 + c \cdot \tan\alpha), & \text{trailing side.} \end{cases} \tag{2.32}$$

By using (2.14)(2.32) the splashing threshold for oblique impact can be obtained:

$$\frac{V}{V_{TC}} \sim We^{1/2} Re^{1/4} f(\alpha) > K, \tag{2.33}$$

with $f(\alpha) = \cos^{5/4}(\alpha)(1 \pm c \cdot \tan\alpha)$. Factor $\cos^{5/4}(\alpha)$, which is a monotonically decreasing function of α, accounts for the droplet submerged by the pool. Factor $(1 \pm c \cdot \tan\alpha)$ which corresponds to term $(1 \pm c\frac{U_\parallel t}{D})$ in (2.31) characterize the mass redistribution among the crown. For an increasing impact angle from 0° to 90°, i.e. a droplet moving more parallel to the surface, the total mass converted from the droplet into the crown will be decreased, leading to a smaller crown velocity on the leading side, while the ratio of mass redistributed to the trailing side will increase. These two opposite effects lead to a maximum of trailing-crown velocity at $\alpha = 19°$.

Here we can distinguish three categories of crown behavior from (2.33). First, when the crown velocity in both leading and trailing side are lower than the splash criterion, the droplet will coalesce with the surface after hitting the pool, which we call deposition. Second, as the impact velocity increases or the droplet is more parallel to the surface, the crown velocity in the trailing side will exceed ($V_{TC} \cdot K$), resulting in single-sided splashing. The increased magnitude of the deceleration of the crown will trigger a Rayleigh-Taylor-like instability, forming several fingers normal to the rim of the crown (we will present the numerical phenomenon in chapter 5) [39, 55]. Due to Rayleigh-Plateau instability, narrow necks are visible in the fingers, which, at a later time, break into droplets. The final phenomenon is the splash in all orientations, reflecting that the crown velocity in the leading side has been elevated over the threshold as well. We classify this phenomenon as omni-directional splashing. This analysis of (2.33) is consistent with the observation in [71], see Fig. 2.8.

In the experiments of [71], the Weber number is varied by giving a different velocity to the droplet. Hence the Reynolds number will be changed simultaneously and can be regarded as a function of the Weber number $Re = We^{1/2}Oh^{-1}$ with a constant $Oh = \frac{\mu_l}{\sqrt{\rho_l \gamma D}}$. As a consequence, (2.33) is rewritten as $We^{5/8} f(\alpha) > Oh^{1/4} K$. We hereby plot (2.33) in a $We - \alpha$ plane. Fig. 2.9 presents the threshold diagram using $K = 130$ and $c = 0.44$ [71]. The plot is separated into three regimes: deposition, single-sided splashing, and omni-directional splashing, by (2.33). It is noteworthy that the trailing side crown is destabilized at first when we increase the impact angle with a constant Weber number. At $We = 380$, for example, the crown destabilizes on the trailing side from deposition to single-sided splashing when the impact angle increases from 0°, and returns to deposition region. This result accounts for that $f(\alpha)$ for the trailing side is monotonically increasing to the impact angle at $\alpha < 19°$, while monotonically decreasing for $\alpha > 19°$.

The experimental data from [71] has been indicated by the colored dots in Fig. 2.9. Model (2.33) shows an agreement with the experiment when discriminating between deposition and single-sided splashing, while a deviation in the transition between single-sided and omni-directional splashing. Besides, we observe an area near the intersection point of (2.33) (i.e. $We \approx 400, \alpha = 0°$) where all the three impact behavior overlap, which is absent in the threshold. The deviation could come from the difficulties in judging the crown behavior accurately due to the camera resolution or the observation plane taken in the experiments [71]. In fact, one of the motivations of our work is to clarify the boundary between the single-sided and the omni-directional splashing regime.

CHAPTER 3

Numerical Methods

In this chapter, we will discuss Basilisk, an open source numerical solver for the partial differential equations. By using an adaptive Cartesian mesh, the program is apt to solve the incompressible Navier-Stokes equations. We use volume-of-fluid (VOF) method to support the two-phase flow in our work. In § 3.1 we discuss the cell-centered finite volume scheme used in Basilisk to discretize the Navier-Stokes equations. In § 3.2 and § 3.3 we briefly explain the VOF method coupled with the octree/quadtree adaptive refinement. This chapter will be concluded by the scalability analysis in § 3.4.

3.1 Basilisk: An Incompressible Navier-Stokes Solver

In a system containing a two-phase incompressible fluid, the flow motion is governed by the Navier-Stokes equations and the continuity equation. In the present study, we restrict ourselves to the regime where $Bo \ll 1$ and $Fr \gg 1$. We hereby neglect the effect of gravity on the flow. The governing equation for the flow is given by

$$\rho \frac{D\mathbf{u}}{D\mathbf{t}} = -\nabla p + \mu \Delta \mathbf{u} + \mathbf{T}_\gamma, \tag{3.1}$$

$$\boldsymbol{\nabla} \cdot \mathbf{u} = 0, \tag{3.2}$$

where p represents the mechanical pressure, $\mathbf{u}$ is the velocity field, and $\mathbf{T}_\gamma$ stands for the stress tensor associated with the surface tension γ. We use a method known as pressure-correction scheme which is one of the firstly developed schemes to obtain the numerical solutions of (3.1) and (3.2) [15]. The method was originally applied by Harlow and Welch in the marker-and-cell scheme for the convenience of handling multi-phase flows [16]. The process of pressure correction is an example of the fractional-step method, in which one time step is split into sub-steps [15]. In Basilisk, a semi-implicit scheme is adopted for the time integral, in which the viscous flux is treated implicitly, while the advection term is handled with the Bell-Collela-Glaz formulation [1].

Pressure-correction Method We now demonstrate the basic approach of the pressure correction method. We assume that the fluid is incompressible with a constant density ρ. Since surface tension only acts along the interface, we can obtain the governing equation for the bulk fluid by writing (3.1) in the absence of surface tension

$$\rho \frac{D\mathbf{u}}{D\mathbf{t}} = -\nabla p + \mu \Delta \mathbf{u}. \tag{3.3}$$

From (3.3) it follows a coupled system of the velocity field $\mathbf{u}$ and the pressure p. The pressure-correction is an iterative scheme to solve (3.3). We decouple the pressure and the velocity field by using a prescribed pressure. Typically, the pressure

obtained at the previous iteration is used as the best guess [15]. To present the basic property of pressure-correction, we just consider an explicit method of first order accuracy in time. Here hereby discretize (3.3) into

$$\frac{\mathbf{u}^{n+1}-\mathbf{u}^{n}}{\delta t}+(\mathbf{u}^{n}\cdot\nabla)\cdot\mathbf{u}^{n}=\nu\Delta\mathbf{u}^{n}-\frac{1}{\rho}\nabla p^{n+1}, \tag{3.4}$$

where the pressure and the velocity in the next time step, i.e. $\mathbf{u}^{n+1}$ and p^{n+1}, should be the final solutions. The superscript n presents the parameters in the previous time step, and δt stands for the time interval. We introduce an intermediate velocity $\mathbf{u}^{*}$, which should be the solution of

$$\frac{\mathbf{u}^{*}-\mathbf{u}^{n}}{\delta t}+(\mathbf{u}^{n}\cdot\nabla)\cdot\mathbf{u}^{n}=\nu\Delta\mathbf{u}^{n}-\frac{1}{\rho}\nabla p^{n}. \tag{3.5}$$

Note that the single time step in (3.4) for the velocity update now has been divided into two sub-steps: $\mathbf{u}^{n}\xrightarrow{\text{step 1}}\mathbf{u}^{*}\xrightarrow{\text{step 2}}\mathbf{u}^{n+1}$. We should correct both intermediate velocity

$$\mathbf{u}^{n+1}=\mathbf{u}^{*}+\mathbf{u}', \tag{3.6}$$

and pressure field

$$p^{n+1}=p^{n}+p' \tag{3.7}$$

by adding the correction terms $\mathbf{u}'$ and p', respectively, such that the solution $\mathbf{u}^{n+1}$ of (3.4) satisfies the divergence-free condition:

$$\boldsymbol{\nabla}\cdot\mathbf{u}^{n+1}=0. \tag{3.8}$$

Consequently, we can obtain the relation between $\mathbf{u}'$ and p' by combining (3.4-3.7), which gives

$$\mathbf{u}'=-\frac{\delta t}{\rho}\nabla p'. \tag{3.9}$$

Eqn. (3.9) implies that we can obtain $\mathbf{u}'$ if the pressure correction p' can be determined. Remembering that $\mathbf{u}^{n+1}$ satisfies the continuity equation, we can take the divergence of (3.9), which gives a Poisson equation relating the intermediate velocity to the pressure correction

$$\Delta p'=\frac{\rho}{\delta t}\boldsymbol{\nabla}\cdot\mathbf{u}^{*}, \tag{3.10}$$

from which field $p^{'}$ can be obtained.

We can conclude the updating process presented by (3.4 - 3.10) as following:

1. Determine the intermediate velocity via (3.5), in which the pressure obtained in the last time step is considered as the initial guess.
2. Obtain the pressure correction term p' by solving the Poisson equation (3.10).
3. Detemine the velocity correction $\mathbf{u}'$ through (3.9).
4. Then the velocity at the time step $n+1$ can be determined by (3.6).
5. Update the pressure by (3.7).

Besides the time integral, we should consider a scheme of the spatial discretization. The solver we used in Basilisk defines all flow parameters in the cell center, while a staggered mesh is applied to connect the values at the cells center with the auxiliary face-defined variables [1, 15].

Surface Tension In (3.1), the stress tensor $\mathbf{T}_{\gamma}$ can be written as

$$\mathbf{T}_{\gamma}=\gamma\kappa\mathbf{n}+\nabla(\gamma), \tag{3.11}$$

where κ, $\mathbf{n}$ stand for the mean curvature, and the normal vector of the interface, respectively. Term $\gamma\kappa\mathbf{n}$ accounts for a force which is normal to the interface, and $\nabla(\gamma)$ is the tangential tensor associated to the gradient of the surface tension. In Basilisk, a height function is calculated in the given dimension (i.e. x, y, z in the present work), from which the curvature is obtained, see [1, 72].

Stability The spatial discretization and the time integral are closely related to the stability of the simulation. A necessary condition for the stability of an discretization scheme is that the numerical domain of dependence should contain the physical domain of dependence [5,14]. This requirement is known as the Courant–Friedrichs–Lewy (CFL) condition [5,14]. For a n-dimensional case, with its spatial length δx_i in the i-th direction, the CFL condition requires that the non-dimension number C, called CFL number, should satisfy

$$C = \sum_{1}^{n} \frac{u_i \delta t}{\delta x_i} < C_{max}, \tag{3.12}$$

where δt stands for the time interval. The CFL number is bounded by a constant C_{max}, whose value depends on the particular numerical scheme.

In Basilisk, the CFL condition is applied to compute the time step δt for the Navier-Stokes equations. Furthermore, the explicit time scheme adopted in Basilisk for the surface tension term gives an extra constraint on the time step which accounts for that the translation of capillary wave should be smaller than the minimal cell size δx_{min}

$$\sqrt{\frac{\gamma}{\bar{\rho}\delta x_{min}}}\delta t \leq \delta x_{min}, \tag{3.13}$$

where $\sqrt{\frac{\gamma}{\bar{\rho}\delta x_{min}}}$ is the capillary wave speed with wavelength δx_{min}, and $\bar{\rho}$ stands for the average density of the fluids on both sides of the interface. Eqn. (3.12)(3.13) will be the basic criteria of the stability in this work, both of which indicate the connection between the resolution and time step, i.e. with a higher mesh level, a smaller time interval δt will be required to maintain the stability of the simulation.

3.2 Volume of Fluid: A Front-capturing Method

The interface tracing methods can be divided into two numerical approaches depending on the types of the grids utilized [30,56–59]. In a front-tracing method, the interface is presented explicitly by a mesh deformed with the flow [30,60]. While in front-capturing methodologies, which include the level-set and the volume-of-fluid method (VOF), the discretization will be implemented in a fixed grid [56–59]. Although the level-set method can present interface accurately, it is subject to lack of discrete mass conservation [61]. The VOF method, however, possesses the property of mass conservation [57–59,61], and is the basis of this work.

Two early descriptions of VOF are given by Noh & Woodward [19] and Hirt & Nichols [57]. In their work a volume fraction field appears which aims to indicate the distribution of different fluids. Supposing that we want to track the liquid phase in a liquid-vapor flow, then the fraction field can be defined as

$$f(\mathbf{x}) = \begin{cases} 1, & \text{if } \mathbf{x} \in \text{liquid}, \\ 0, & \text{if } \mathbf{x} \in \text{vapor}, \end{cases} \tag{3.14}$$

where $\mathbf{x} = (x, y)$ presents the space coordinate. The evolution of the fraction field is described by the advection equation

$$\frac{\partial f}{\partial t} + \boldsymbol{\nabla} \cdot (\mathbf{F}) = 0. \tag{3.15}$$

where $\mathbf{F} = \mathbf{u} f(\mathbf{x})$ indicates the fraction flux per area.

There are two major steps to implement the VOF method: the interface reconstruction and the fraction flux computation. Fig. 3.1 illustrates the updating steps of the fraction field from time t^n to t^{n+1} in a 2D discretization mesh, where we want to trace the fluid colored green. Fig. 3.1a shows a prescribed fraction field at the beginning, in which the volume ratio of a cell occupied by the green fluid is presented by the local fraction value. Consequently, the cells located on the interface have $f(\mathbf{x}) \in (0,1)$. In Fig. 3.1b a linear interface is reconstructed. Next, we calculate the fraction flux $\mathbf{F}$ caused by the convection. These fraction flux will lead to a fraction volume flowing through the cell boundaries between the time interval, see Fig. 3.1c.

A clear reconstructed interface is necessary to prevent numerical diffusion when we discretize (3.15) [19,57–59,61,62]. As schematically shown in Fig. 3.2, a fraction field (red bulk) is convected from left to the right, in a one-dimensional coordinate system. The initial distribution of the volume fraction is shown in Fig. 3.2a. After one time step, a partial amount of the fluid enters the grid $i+1$. Meanwhile, the fraction remained in the cell $i-1$ and i can be determined, see the transition process presented in Fig. 3.2b. Then, as shown in Fig. 3.2c, the updated fluid fraction is spread uniformly over the cell,

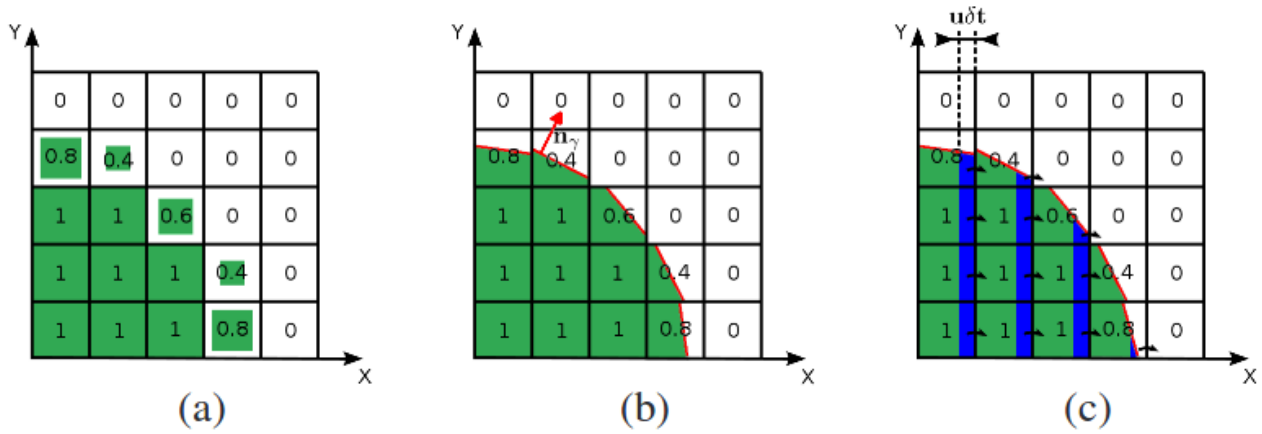

Figure 3.1: A sketch for the VOF method applied in the 2D geometry. The image is taken from [58]. **(a):**The fraction field distributed in the domain is defined in advance. Cells which are fulfilled by the green fluid have the fraction value of unity, while the value of zero in each empty cell. **(b):** The interface is reconstructed using the PLIC method. In each interface cell, the area sealed by the constructed interface (the red lines) and the mesh border equals to the volume fraction occupied by the green fluid. **(c):** In this step the fraction flux is determined. Here only the x components of the flux vectors are presented, indicated by the arrows crossing the cells' boundary. The blue region represents the fraction volume flowing from the upwind cells to their neighbors. The new fraction distribution can be obtained later on, and the reconstruction step shown in panel (b) is duplicated.

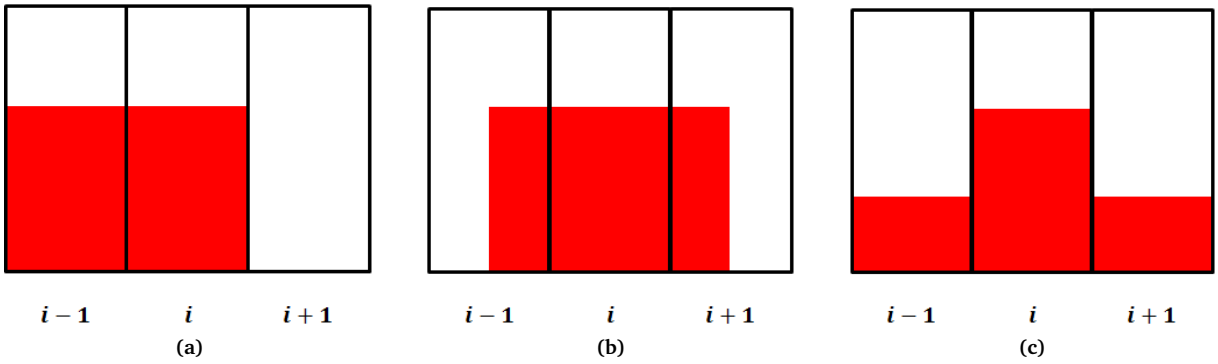

Figure 3.2: A sketch interpreting the numerical diffusion of the fraction field when there is no interface reconstruction. **(a):** The fraction field (red buck) distribution at the beginning. **(b):** The translation of the fraction field. We can determine the amount of the volume fraction entering and leaving the local cells. **(c):** The fraction field after re-distribution, which spreads uniformly over the cells, leading to an increased length of the fraction profile. This behavior results in numerical dispersion of an advected fraction field.

leading to a dispersion regarding the fraction profile. In the early work of Noah and Hirt, the interface is presented by a plane (a straight line in 2D) either parallel or perpendicular to the cells boundaries [19]. Although this algorithm works well if the flow is initially aligned to one of the coordinate orientation, it fails to describe the interface accurately for a more sophisticated flow. An improvement algorithm, which is known as Piecewise Linear Interface Construction (PLIC), presents the interface by a portion of a plane (a line segment in 2D) with an arbitrary direction within the cell containing multi-material [20, 59, 62, 68]. These reconstructed linear interfaces can be uniquely determined by the local volume fraction and a normal vector. Basilisk follows the Mixed Young Centered method (MYC) to determine the normal vectors [1]. Originally described in [59], the MYC approximation optimizes the selection between Young's method and the centered-column method, both of which estimate the normal vector according to the fraction gradient, see [59].

3.3 Octree Adaptive Refinement and Parallelisation

Compared to the uniform grid, adaptive-mesh-refinement (AMR) can considerably reduce the memory consumption and the CPU time [70, 74, 76, 77]. The researchers handling a multiphase flow problem will typically use a block-based AMR approach, which creates patches of refined grids overlying the original mesh. Each patch has an equal or a close number of the cells with others [65, 77, 78]. Besides the block basis, an alternative is the use of the octree/quadtree AMR coupled

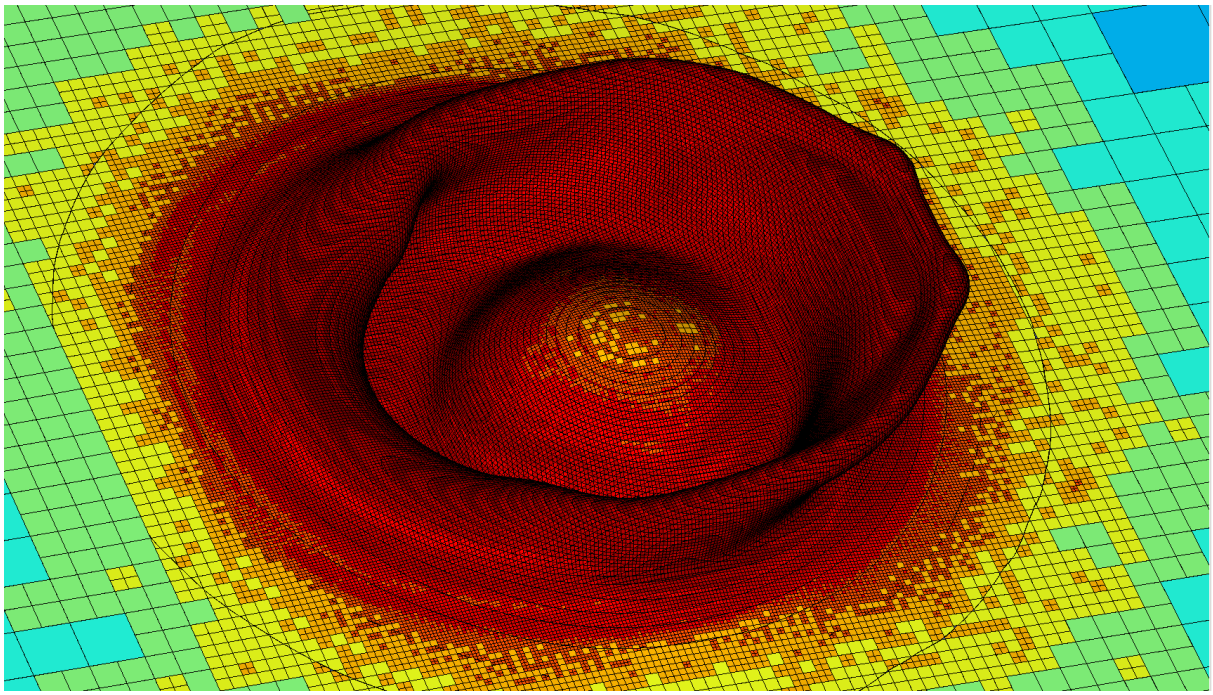

Figure 3.3: Octree Adaptive Refinement Mesh implemented in the current work. The grid distribution and the cell size are visible on the interface. The grid resolution increases corresponding to the color scale from blue to red. The spatial discretization is allowed to be locally varied based on the wavelet analysis of the fraction field and the velocity.

with the Cartesian grid [73, 75, 76, 78]. Tree structure AMR is an example of the cell-based scheme, which typically leads to less amount of the cells created when compared to the block-based method [70]. Furthermore, the tree refinement allows for a spatial discretization which can be locally refined or coarsen in a more efficient way [78]. Fig. 3.4 offers a view of the quadtree AMR (octree in 3D) in terms of the spatial discretization and its corresponding logical structure. An initial domain is divided into four quadrants, called the children cells of their parent cell, with an identical geometry size. By duplicating this process, the tree root is refined into branches, and finally, to the leaf cells. Therefore, a refined mesh hierarchy is directly represented in the tree structure, which permits an efficient algorithm for some spatial-implicit problems such as the Poisson equation [73, 78].

Another advantage of the tree refinement is that it benefits from the easy execution of the interface-tracking methods coupled with the Cartesian grid, such as VOF with PLIC reconstruction mentioned above. Popinet et al. [73] developed a solver combining the tree adaptive refinement with the VOF method, and it is succeeded by Basilisk [1, 2, 66, 67, 78]. The resulting method allows a full adaptivity along the interface based on the wavelet analysis of the local field [1], e.g. the volume fraction and the velocity field in the current work. The performance of this adaptive refinement scheme in this work is presented in Fig. 3.3. The grid configuration is visible at the interface, and the mesh density is indicated by different colors. The region near the crater where we are more interested is refined to a higher resolution which corresponds red or yellow, while the region far away from the impact point is coarsened, shown in color green and blue.

Domain Partition The parallelization scheme used in Basilisk is the spatial decomposition, where the global domain is decomposed into several sub-regions, within each of them an identical instruction will be executed by a parallel core [1, 78]. Therefore the selection of the domain partition scheme is of great significance to the solver performance.

In Basilisk the option is coarse-grain domain partition, in which the domain separation is executed by the unit of the entire tree [78]. This means that the leaf cells (i.e. the finest cells) from a single tree will always belong to one sub-domain and handled by one processor, see Fig. 3.4. This is in contrast to the refined-grain scheme, where the leaf cells are under high flexibility in terms of the distribution among the parallel processors, leading to an intricate tree structure.

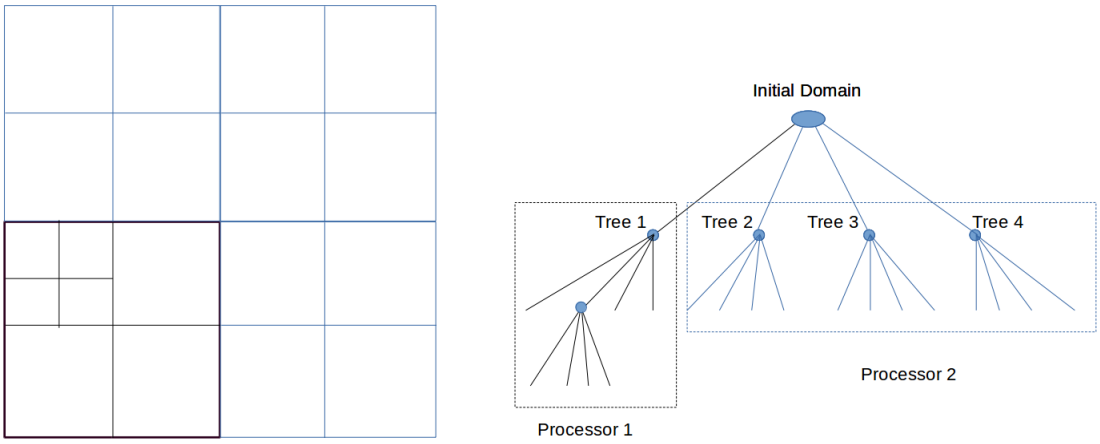

Figure 3.4: A sketch interpreting the domain partition by two processors with coarse-grain parallelism, implemented in a quadtree refinement mesh. **Left:** The spatial decomposition. The initial domain, say level 0, is divided into four sub-domains with an identical size. These four blocks (level 1) are considered as the children cells for their parent. Here the cells are colored based on the different processors they belong to. The parallel processors will execute the identical instruction, but only on their own subdomains [78]. **Right:** The corresponding logical structure. Four octrees are derived from the initial domain, and three of them are included in processor 2. The rest quadtree will be handled by processor 1.

3.4 Scalability

We conclude this chapter by the scalability analysis in order to estimate the CPU time and memory of the simulations in this thesis. The evaluation is based on a benchmark simulation, where we run 5000 time steps on the case of perpendicular droplet impact on a liquid pool. We simulate this impact problem in a three-dimensional setting, which is identical to the final oblique impact case. We will discuss this computational setting in chapter 5. The impact Weber number is given as $We = 150$. Considering that the parallel efficiency is affected by the amount of the cells handled by a single processor [78], we vary the mesh level i, that is, 2^i grid points per dimension and $(2^i)^3$ cells in total in a three-dimensional domain, from level 9 to level 11. The CPUs number increases from 4 to 64. After 5000 steps the time scale in the simulation will attain: $t^* = \frac{t}{D/U} \approx 0.82$ for mesh level 11; $t^* \approx 3.14$ for mesh level 10; $t^* \approx 28.6$ for mesh level 9 where D and U stand for the droplet diameter and its initial velocity, respectively. Although the impact process is incomplete at $i = 5000$, the droplet is partially submerged by the pool, and a crown above the surface is readily visible. Therefore we assume that the time steps of 5000 are qualified to the scalability estimation. The whole benchmark simulations have been done on the cluster of Eindhoven University of Technology, and the results have been summarized by Fig. 3.5.

Computation Time The parallel performance of a parallelizable program is formulated by Amdahl's Law [63], which states that the theoretical parallel efficiency η to be obtained by applying N processors will be bounded by

$$\eta \leqslant \frac{T_1}{N(f + \frac{1-f}{N})T_N}. \tag{3.16}$$

In (3.16), f stands for the fraction of the code which cannot be parallelized. T_1 and T_N correspond to the code execution time when we apply one and N processors respectively. Although there have been some arguments about its accuracy, Amdahl's law remains a straight-forward approach to point out a potential speedup through parallelism. In Basilisk, the main function and most of the auxiliary events are executed in parallel, hence $f \approx 0$. Therefore, the benchmark program should ideally scale linearly, i.e. $T_N \sim N^{-1}$. Fig. 3.5a presents the running time T_N as the function of the mesh level and the CPUs number N. The straight lines are obtained by the linear fitting in a double logarithmic plot. For all grid resolution, T_N decreases for the increasing processor number. Nevertheless, the exponential of the linear fitting result, which is shown in table 3.1, indicates an undesirable parallel efficiency.

Memory Per Core As discussed in the § 3.3, the computation domain of the simulation in this work will be divided into several sub-regions, and each of them will be handled by one parallel processor. A load-balancing algorithm in Basilisk allows the total memory to be almost equally distributed between the parallel cores [78]. Consequently, the memory per core M_N should scale as $M_N \sim N^{-1}$ when we apply N processors to the code. Fig. 3.5b gives a double logarithmic plot for M_N as

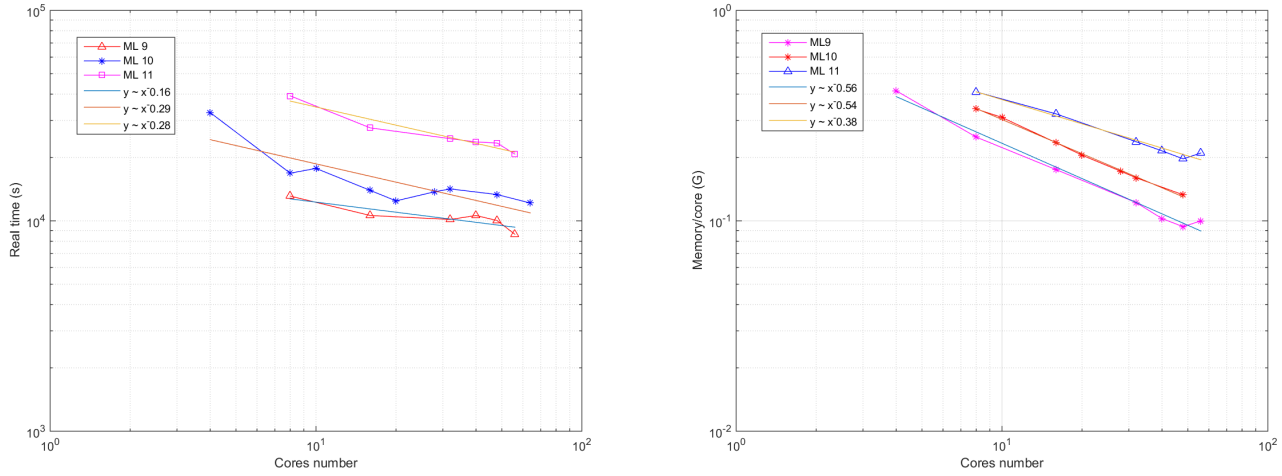

(a) **(b)**

Figure 3.5: Scalability results using the cluster at Eindhoven University of Technology. The test simulation is the perpendicular droplet impact on a deep liquid pool(see Fig. 2.12). The mesh level is changed from 9 to 11. We run this test case for 5000 steps, after which the droplet will partially submerged by the pool (see text). Given the available computational resources and the fact that the crown is visible after $i = 5000$, we think the benchmark is qualified to estimate the scalability. **(a)**: The CPU time as a function of cores number. We offer the linear fitting function in log-log scale, see table 3.1. For different resolution, the running time decreases for the increasing cores number. However, the wiggle of the connection line and the small exponential of the fitting results reflect the undesirable parallel efficiency. **(b)**: The memory consumption for each core as a function of the CPUs number. When distributing the simulation into the parallelism processors, the memory load for each core will declines. Nonetheless, it is still away from the ideally linear decrease $y \sim x^{-1}$, see table 3.1. This result refers that the total memory for the simulation will have a substantial increase if we apply more processors.

the functions of the mesh level and N. For the different resolutions, the memory per core decreases for the increasing CPUs number, while it diverges from the linear scaling $M_N \sim N^{-1}$, see table 3.1. The scalability analysis anticipates a substantial increase in the total memory when we apply more cores, which in turn, prolongs the simulation time in comparison to $T_N \sim N^{-1}$. The extra memory could come from the connection and the synchronization between the different nodes. Yet another memory source is the communication between the parallel processors. It occurs when the fraction field (e.g. a splashing drop) is adevected from the territory of one processor to another.

Table 3.1: Linear fitting results for the CPU time T_N, and for the memory per core M_N.

Mesh Level	$T_N \sim N^x$	$M_N \sim N^x$
9	$T_N \sim N^{-0.16}$	$M_N \sim N^{-0.56}$
10	$T_N \sim N^{-0.29}$	$M_N \sim N^{-0.54}$
11	$T_N \sim N^{-0.28}$	$M_N \sim N^{-0.38}$

In the benchmark simulation the time scale should achieve $t^* \sim 35$ if we want to get a full impact. As a result, we expect $i \sim 10^5$ of time steps to complete the simulation when applying mesh level 11, leading to about 10 days of CPU time when we run the simulation on 32 cores. Assuming that we submit ten missions with the identical setting of the benchmark case. Each job is run on 32 cores. Then the total CPU time is around three months. In the case of oblique impact, we push the resolution to a higher level of 12. We aim to get more accurate results (especially for the splashing of the crown) at the cost of significantly increased CPU time and the memory. Furthermore, when we have a higher Weber number, more area of the cavity surface will be created, extending the cavity growing time. In this case, the time scale t^* as well as CPU time should be longer (as compared to the benchmark) to complete the impact. The increased amount of the splashing droplets occurring with a larger Weber number also causes a larger workload, and, as a consequence, a longer CPU time. The runtime of oblique droplet impact in this work is nearly 60 days, along with approximately 50 GB memory for a single job. In fact, the balance between the available cluster resources and the expected accuracy of the simulation is one of the key issues in this work.

CHAPTER 4

Numerical Validations

In order to estimate the capability of Basilisk to cope with capillary flow, we carry out two validations and compare the numerical results with the reference data presented in chapter 2. First of all, we will show a simulation with perpendicular droplet impact on a solid substrate in § 4.1. We record the maximum spreading diameter of the droplet for a wide range of Weber numbers. The results will be compared to the available models for the spreading dynamics as referred to in § 2.1. Later on, we show the simulations of perpendicular droplet impact onto a liquid pool in § 4.2. We compare the maximum cavity depth to the scaling argument described in § 2.2. We simulate these two validations in a cylindrical coordinate system.

4.1 Droplet Impact onto a Solid Substrate

In this section, we focus on the spreading process of droplet impact on a solid substrate for a wide range of Weber numbers. We record the spreading ratio $D^* = \frac{D_m}{D}$, where D_m and D are the maximum spreading diameter and the initial size of the droplet respectively. The simulation output is compared with the literature referred to in § 2.1.

Fig. 4.1 presents the computational setting for the perpendicular droplet impact on a solid substrate. We put a droplet with a diameter $D = 0.04$ and its density ρ_l above the bottom. The initial distance between the droplet and the substrate is $0.1D$. We expect an axisymmetric spreading of the droplet in the perpendicular impact. Hence we carry out the simulation in a cylindrical domain with a symmetry axis. When the simulation starts, the droplet approaches the substrate along the symmetry axis with a downward velocity $U = 1$, see 4.1a. In Basilisk, the cylindrical coordinate system is visualized by its square cross-section as shown in 4.1b. The computational domain has a length of $12D$. We implement an adaptive refinement mesh (with its maximal mesh level 11, i.e. 2048^3 cells number in total) in which the volume fraction and velocity field account for the local refinement, see the previous discussion in chapter 3. In order to diminish the effect from the surrounding vapor on the impact process, we set the density and the viscosity ratio between the droplet and the surrounding vapor as $\rho_l/\rho_g = 1000$, $\mu_l/\mu_g = 100$ respectively. To reduce the number of variables, we fix the Reynolds number $Re = 1000$, and disable the gravity.

4.1.1 Maximum Spreading Diameter

We set an outflow condition on both lateral and the top walls. As for the solid substrate, we set two groups of simulations in terms of the different boundary conditions. In group 1, a droplet will hit on a free-slip bottom, while in group 2 we apply a no-slip bottom for the impact. For both groups the droplet approach the substrate with different Weber numbers ranging from 35 to 350 by varying the value of surface tension. The contact angle is 90° for both groups. To assess our numerical results, we use

$$J^* = \frac{1}{N}\sqrt{\sum_{We\in(35,350)}\left(\frac{D^* - D_r^*}{D_r^*}\right)^2} \tag{4.1}$$

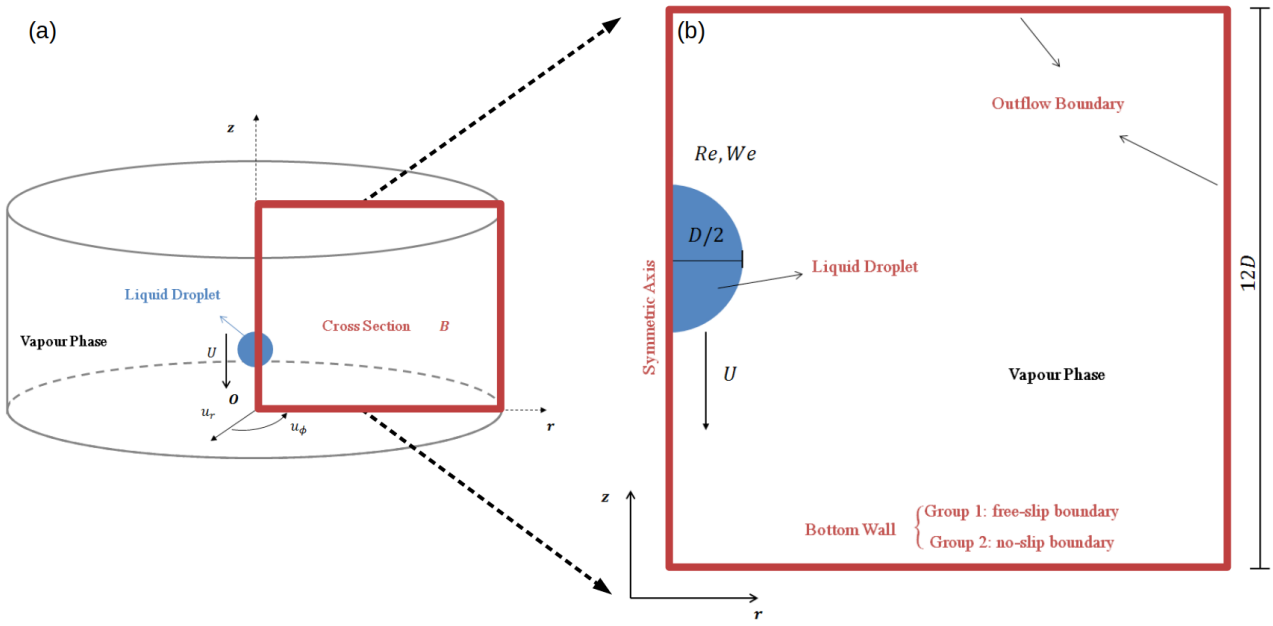

Figure 4.1: Computational setting for the perpendicular droplet impact onto a solid wall (schematic figure). **(a):** The 3D perspective of the computational setting. We set a cylindrical coordinate system for the impact problem. The droplet spreading is simply attributed to the radial velocity u_r concerning the symmetry axis. Therefore, we expect an axisymmetric phenomenon. The droplet is approaching the solid bottom along the symmetry axis, with a vertical velocity of $U = 1$. The diameter of the droplet is $D = 0.04$, then the side length of the domain is $12D$. The lateral walls and top ceil are set with outflow boundary condition. In the group 1, we set a free-slip boundary for the bottom, while in group 2 the droplet hits on a no-slip wall. **(b):** The cross section of the cylindrical coordinate system, presented as a square. This cross section is the visualization of the simulation output, which means only half of the impact is simulated by imposing a symmetry axis.

to determine the standard deviation J^* between our numerical results and the equations referred to in § 2.1 which provide the reference value D_r^* corresponding to different Weber numbers. The values of J^* are presented in table 4.1.

Table 4.1: Comparison between the simulation with the reference data.

Bottom Condition	Contact Angle	Reference	J^*
no-slip	90°	Roisman et al. [33]	4.1%
no-slip	90°	Wildeman et al. [32]	3.5%
free-slip	90°	Wildeman et al. [32]	1.9%

Comparing the data from group 1 (with a free-slip substrate) with (2.7) a relative deviation of 1.9% is obtained, see Fig. 4.2a. Then we apply a no-slip substrate for the impact (group 2), in which we expect an extra restraint force coming from the viscous friction, leading to a smaller spreading ratio than that of the free-slip substrate. We present the comparison between the data of group 2 with (2.5) and (2.8) in Fig. 4.2b, from which we obtain a deviation of 3.5% and 4.1% respectively. In comparison to Basilisk results, the spreading ratio when we apply the no-slip substrate is underestimated by the experiments of [33]. This deviation could come from an artificial numerical-slip near the bottom [64]. After the droplet impact on a solid substrate, a contact line (i.e. the intersection line of solid-liquid, liquid-vapor and vapor-solid interfaces) will be formed when the droplet spreads. This contact line will be stationary if we impose a no-slip boundary on the substrate. The prediction is in contrast to the reality where the contact line does move [64, 86]. This singularity problem is known as Huh & Scriven's paradox, which was firstly pointed out in [87]. To account for the motion of the contact line, several numerical approaches have been developed such as the introduction of a slip length to the substrate [32, 64]. As shown in Fig. 4.3b, the slip length L_s defines a non-zero velocity at the solid surface which accounts for the movement of the contact line. The value of L_s should be small enough compared to the shear boundary layer in the liquid phase, so that this artificial variable does not change the overall spreading behavior for the real no-slip substrate [32].

In our simulation, however, the involved VOF scheme and the staggered mesh (where the flow variables are defined on the interface of the cells) avoid this singularity problem of the contact line. As presented in Fig. 4.3a, the interface velocity

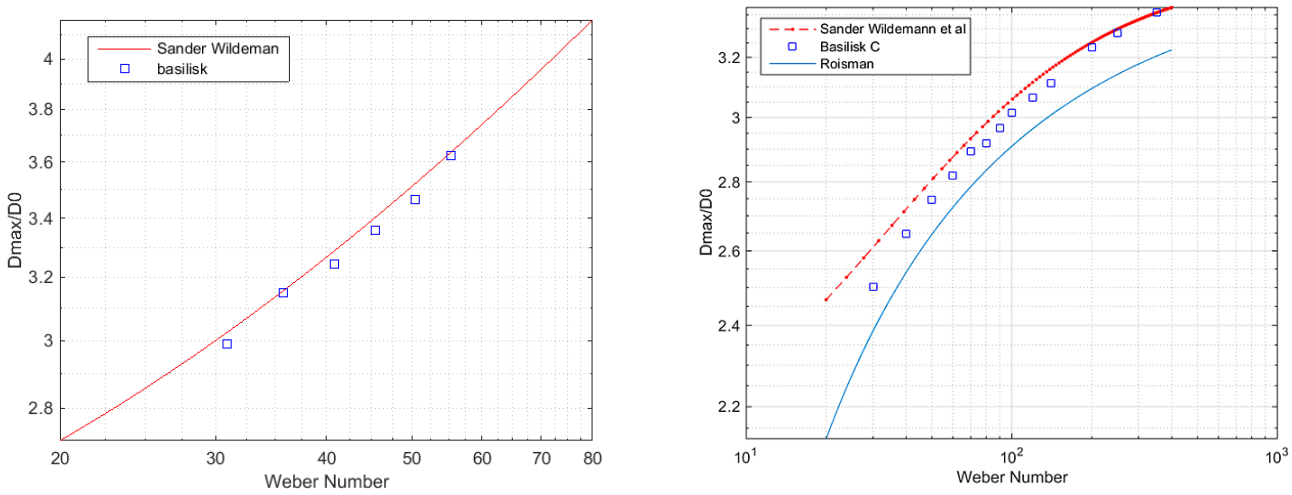

(a) **(b)**

Figure 4.2: Maximum spreading diameter D_m(scale by the droplet diameter) in a double logarithmic plot. The data are scaled by the droplet diameter. **(a):** Comparison between group 1 and the reference data. The bottom wall is set as the free-slip boundary condition, with a contact angle of 90°. Eqn. (2.7) is presented as the solid line. **(b):** Comparison between group 2 and the reference data. The substrate is set as a no-slip wall with 90° contact angle. The red-dashed line corresponds to Eqn. (2.8), while the blue-solid line presents Eqn. (2.5) [32, 33].

along the r-axis $u_{i-1/2,2}$ accounts for the advection of the fraction field. Therefore, if $u_{i-1/2,2}$ has a non-zero value, the contact line can numerically move along r-axis. In this case, the no-slip boundary condition is imposed by extrapolating the velocity of the virtual points in the solid substrate $u_{i-1/2,1}$. In Basilisk, a linear profile is assumed for the boundary velocity, leading to

$$u_{i-\frac{1}{2},1} = -u_{i-\frac{1}{2},2}, \tag{4.2}$$

in which the finite value of $u_{i-1/2,2}$ drives the motion of the contact line. The numerical slip, on the one hand, avoids the problem of the contact line and simplify the simulation, while, on the other hand, the value of $u_{i-1/2,2}$ could be affected by the fields (velocity and the fraction) near the substrate, which could account for the deviation between D^* in group 2 and [33].

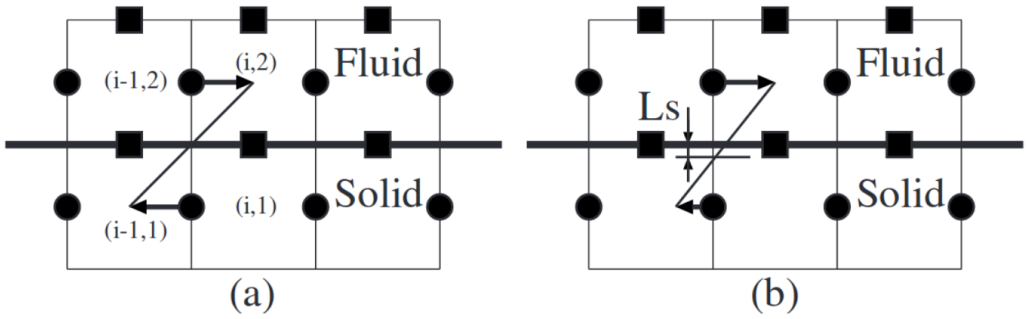

Figure 4.3: Schematically plot of no-slip substrate (panel (a)) and the slip length (panel (b)). Image is taken from [64]. **(a):** The cells on the both sides of the solid-liquid interface. Note that virtual points $i-1,1$ to $i+1,1$ are introduced inside the solid substrate. Black circles and squares stand for the cell-interface velocity along r-axis and z-axis, respectively, where r and z are consistent with the coordinate system in Fig. 4.1. The velocity along r-axis is indicated by arrows. By extrapolating $u_{i-1/2,1}$ from Eqn. (4.2) we impose the no-slip boundary condition on the substrate. **(b):** The slip length L_s which defines a finite velocity on the solid surface.

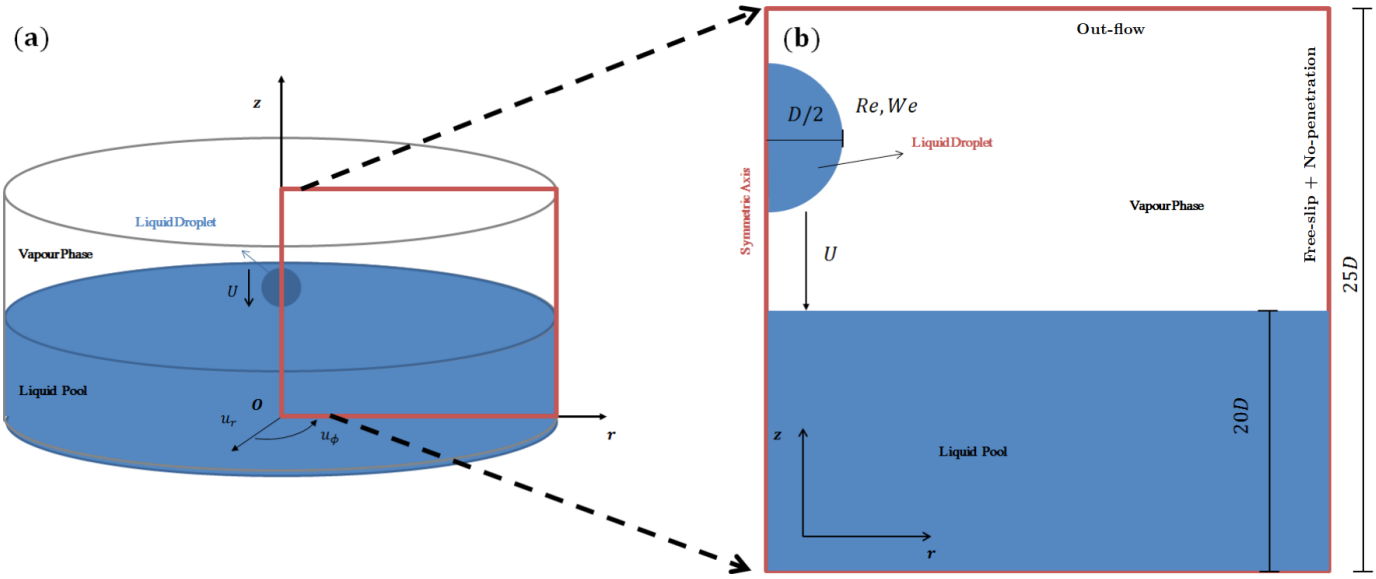

Figure 4.4: Computational setting for the perpendicular droplet impact onto a liquid pool (schematic figure). **(a):** The 3D perspective of the computational setting. We set a cylindrical coordinate system for the impact problem. The droplet is approaching the pool surface along the symmetry axis, with a vertical velocity of $U = 1$. The diameter of the droplet is $D = 0.04$, then the side length of the domain is $25D$. We set a pool with a depth $20D$ below the droplet at the initial time. We apply an outflow boundary condition for the top, while the lateral walls are free-slip plus no-penetration boundaries. As for the bottom of the pool, we apply a no-slip boundary. **(b):** The cross section of the cylindrical coordinate system, presented as a square. This cross section is the visualization of the simulation output, which means only half of the impact is simulated by imposing a symmetry axis.

4.2 Perpendicular Droplet Impact onto a Deep Liquid Pool

Now we focus on the droplet impact on a liquid pool. Among the consequent phenomena, we primarily study the maximum cavity depth h_m/D (as defined in § 2.2), and we compare the numerical results with the equation referred to in § 2.2. In comparison to the impact on a solid substrate, we expect a more sophisticated interface to appear when a droplet hits on a pool. Consequently, the numerical results in this section will directly indicate the capability of Basilisk to perform a droplet impinging on a pool.

Based on the cylindrical coordinate system defined in § 4.1, we keep the droplet diameter $D = 0.04$, while the dimension of the domain is enlarged to $25D$. we add a liquid pool with its depth $20D$ below the droplet, see Fig. 4.4. We apply free-slip plus no-penetration boundary conditions to the lateral walls, and a no-slip wall to the bottom of the pool. The initial distance between the droplet and the pool surface is $0.1D$. The viscosity and the density ratio between the surrounding vapor and the liquid is $\mu_l/\mu_v = 100$, $\rho_l/\rho_v = 1000$, respectively. Likewise, we set $Re = 1000$ and disable the gravity, while the Weber number is changed in $We \in (10, 900)$ by varying the values of surface tension γ. The simulation is done using a mesh level of 11 with adaptive refinement based on the fraction and velocity field.

4.2.1 Maximum Cavity Depth

Fig. 4.5 presents a double logarithmic plot of h_m/D as a function of the Weber number. We observe that for $We \lessapprox 300$, the numerical data are in agreement with $h_m \sim We^{1/2}$, which has been obtained by using energy argument (2.11). However, at a higher Weber number our data are lower than the scaling. This deviation could arise from an additional portion of the kinetic energy dissipated by the splashing and the ripples propagating above the surface. Also, the energy proportion of droplet transferred to the target pool could decrease with a higher Weber number [22]. The experimental data of h_m from most relevant literature were concluded with droplet size comparable to the capillary length $\sqrt{\frac{\gamma}{\rho_l g}}$, and hence we lack the reference data of maximum cavity depth free from gravity, i.e. h_m is always a coupled function of the Weber number and the Froude number [22, 27–29]. As discussed in § 2.2.1, when Bond number $Bo = \frac{We}{Fr} \ll 1$, the capillary force dominates the cavity formation, and h_m is characterized by the Weber number [28]. As for a increases Bond nmuber, more kinetic energy of droplet is converted to the gravitational potential energy [26]. Therefore, the maximum cavity depth cease to increase and begins to be a sole function of the Froude number [29]. In analogy to the energy argument presented above, we could provide a possible qualitative interpretation of the deviation shown in Fig. 4.5.

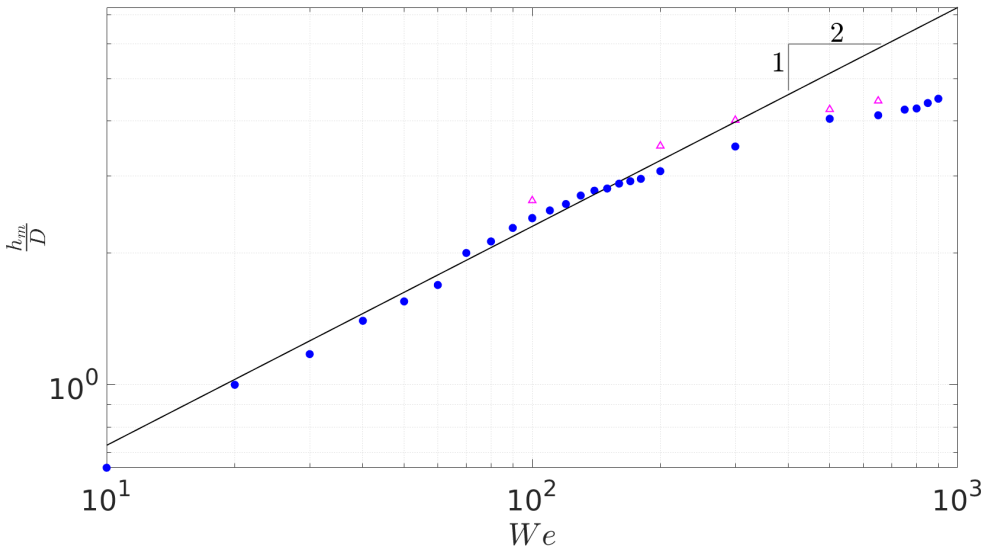

Figure 4.5: Double logarithmic plot of maximum cavity depth h_m (scaled by the droplet diameter D) as a function of Weber number for perpendicular droplet impact onto a liquid pool. The solid line has a slope of $1/2$. We use symbols to present: impact with $Re = 1000$ (blue dots); impact with $Re = 2500$ (upward-triangle). For the Weber number larger than $We \approx 300$, we observe that h_m/D is increasingly smaller as compared to the scaling law $h_m/D \sim We^{1/2}$. This deviation could be explained by the viscous dissipation (see text), which could account for the higher cavity depth when we increase the Reynolds number.

Remembering that we obtain the scaling (2.12) by ignoring viscosity. In our simulation the Reynolds number used to quantify the effect of viscosity is taken constant and high ($Re = 1000$). In line with the Bond number which identifies the comparison between gravity and capillary force, we assume that there is a non-dimensional number constructed by the Reynolds number and the Weber number, say $\frac{We^{\zeta_1}}{Re^{\zeta_2}}$ with a set of specified exponentials ζ_1, ζ_2. As for a small Weber number, i.e. $\frac{We^{\zeta_1}}{Re^{\zeta_2}} \ll 1$ the viscosity-effect could be neglected, which is consistent with the energy argument (2.11). While for an increasing We with a fixed Reynolds number, this viscous dissipation can be comparable to the increased surface energy E_γ in (2.11). When $\frac{We^{\zeta_1}}{Re^{\zeta_2}} > 1$, the viscosity comes into play, and impedes the growth of the maximum cavity depth. This argument could be supported by the results of larger h_m when we increase the Reynolds number from 1000 to 2500, see Fig. 4.5.

Besides the physical factors, the disability of our simulation when describing the splashing could contribute this deviation. The splashing appearing in an axisymmetric geometry presents a liquid ring surrounding the symmetry axis. This artificial phenomenon is in contrast to the physical splashing, in which a breakup droplet is produced instead of the ring. For a small Weber number, the splashing is unlikely to occur, or, once the crown breaks, the mass and the kinetic energy carried by the ring could be negligible in comparison to the total liquid. However, when the Weber number increases, the splashing would be more violent, causing a greater effect on the impact process and the cavity depth.

Another argument is the possible effect from the crown accounting for the total increased surface. The surface energy due to the increased crown $E_{\gamma,crown}$ scales as $\gamma h_m h_{crown}$ where h_{crown} stands for the crown height (as defined in Fig. 2.4). A theoretical model which assumes that the volume of the crown is equal to the volume of the cavity in [22] indicates that h_{crown} is proportional to the maximum cavity depth h_m. This output suggests that the increased crown surface would not affect the scaling law of $h_m \sim We_{1/2}$. In fact, from the simulation with $We \in [140, 900]$ we obtain that h_{crown} is in the range of $0.11h_m$ to $0.22h_m$, resulting in that $E_{\gamma,crown} \sim 0.16\gamma h_m^2$ in average. The small proportion of the total surface accounted by the crown cannot interpret the deviation of the numerical results from $h_m \sim We^{1/2}$, which, for example, is up to $0.55h_m$ at $We = 900$.

4.3 Conclusion

In this chapter, we presented two validations: perpendicular droplet impact on a solid substrate and a deep liquid pool in a cylindrical coordinate system. We quantified the numerical phenomena, and compared them with the reference data as

discussed in chapter 2.

For the impact on a solid substrate, we studied the maximum spreading diameter D_m for a wide range of Weber number with different bottom properties: free-slip and no-slip substrates. An agreement was observed in the comparison between the reference and the numerical data with the free-slip substrate. As for the no-slip substrate, we obtained a higher value in our simulations when compared to the experiments of [33]. This deviation ($\approx$ 4% of the reference data) could be induced by the numerical slip due to the VOF method and the staggered grid used in our work. Then we studied the perpendicular droplet impact on a liquid pool for different Weber numbers. From the simulations, we observed that $h_m/D \sim We^{1/2}$ when $We \lessapprox 300$, which is consistent with the energy argument discussed in chapter 2. When the Weber number is up to 300, the value of h_m/D is increasingly smaller in comparison to $h_m/D \sim We^{1/2}$, probably caused by a more important role of viscous dissipation as we decrease the surface tension. Besides, the disability of a cylindrical coordinate system when describing splashing could be another factor in this deviation.

In conclusion, we obtained an agreement between the validations and the reference data. Based on the numerical solvers adopted in these validations, we extend the code for oblique droplet impact on a liquid pool. As a consequence, the performance of Basilisk in validations enhances the reliability of the simulations for the oblique impact.

CHAPTER 5

Oblique Droplet Impact onto a Deep Liquid Pool

In this chapter, we will present the numerical results of oblique droplet impact onto a deep liquid pool. We perform a series of simulations in a wide range of Weber numbers and impact angles. From the numerical results, we focus on the crown behavior, cavity angle, and the dimensions (the depth and the displacement) of the cavity.

First, we will introduce a three-dimensional computational domain in which oblique droplet impact will be carried out in § 5.1. We will show a sensitivity analysis, from which we determine a doable resolution for our simulation. Then we present three different types of crown behavior in § 5.2. We also quantify the crown behavior into a phase diagram of the Weber number and the impact angle. The evolution of cavity angle will be discussed in § 5.3. We will study the relationship between the collapse angle and the impact angle. As for the cavity dimensions to be discussed in § 5.4, we offer a description of the cavity evolution. During the simulations, we track the deepest point of the cavity, from which we obtain the maximum cavity depth. Later on, we present the data of the cavity displacement. We will show details of qualitative comparison between the simulations and the phenomena experimentally observed in [71].

5.1 Numerical Setup

During oblique droplet impact, we expect an asymmetric phenomenon which cannot be correctly represented by an axisymmetric geometry. Therefore, we construct a fully three-dimensional domain in which the complete oblique impact will be performed. As presented in Fig. 5.1, we set a cubic box containing a system of liquid-vapor. A spherical liquid droplet with a diameter D is set above a liquid pool whose depth is $8D$. A similar size of the pool has been utilized in several numerical studies [45,80]. The cubic domain has a dimension of $12D$. The initial distance from the droplet to the flat interface is $0.1D$. We set the density and the viscosity ratio between the liquid phase and the surrounding vapor as $\rho_l/\rho_v = 1000$, $\mu_l/\mu_v = 100$, respectively. The outflow boundary condition is applied in the top wall of the domain. We simulate half of the impact by using a symmetric wall in the $y-z$ plane, while the rest of lateral walls are free-slip plus no-penetration boundaries. As for the pool bottom, we impose a no-slip wall. We set a homogeneous Neumann boundary condition for the fraction field f, i.e. $\partial f/\partial n = 0$, where n presents the normal direction in respect of the boundary.

When the simulation starts, the droplet approaches the pool along the symmetry plane with a velocity U and an impact angle α. The droplet momentum is decomposed into a parallel velocity $U_\parallel$ and a vertical velocity $U_\perp$ (as defined in (2.20)). We produce the snapshots of the simulations at different t^* where $t^* = \frac{t}{t_i} = \frac{t}{D/U_\perp}$, and we mark $t = 0$ as the moment when the droplet makes the first contact with the pool surface. To keep the simulation away from the unstable regime, we set a constant velocity $U = 1$ for the droplet. To reduce the number of the variables, we fix the Reynolds number 1000, and disable gravity (i.e. $Fr = \infty$). We change the Weber number by varying the values of surface tension. An adaptive refinement mesh is applied in our simulation, see § 3.3 for more information about the spatial resolution and the refinement scheme in Basilisk.

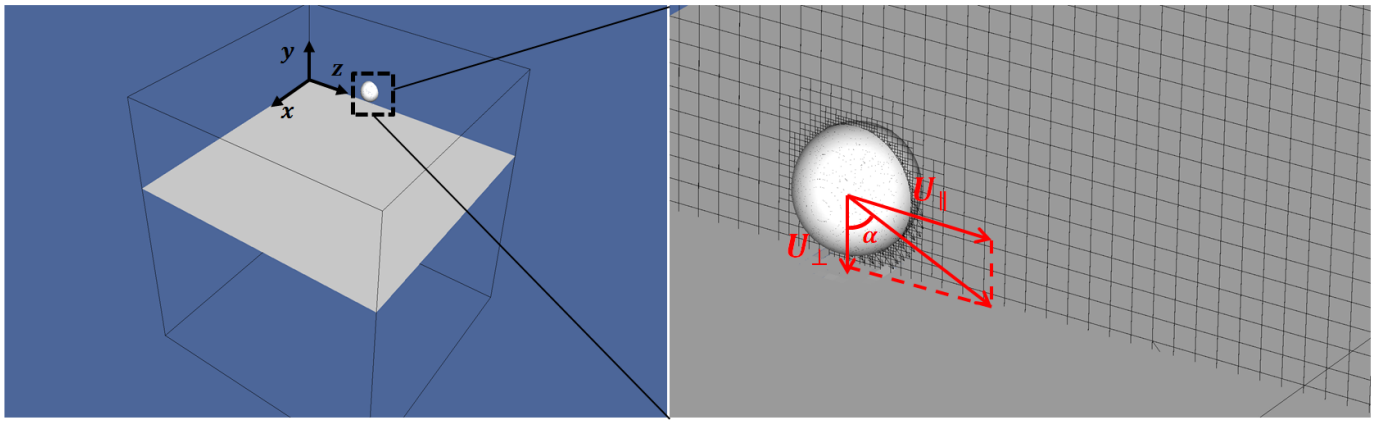

Figure 5.1: The three-dimensional computational setting where oblique impact will be performed in. Only vapor-liquid interface is illustrated. **Left:** A cubic tank whose lower part represents a liquid pool. We set a droplet above the pool surface ($y = 0$) at the initial time. The drop diameter is D. The pool depth is $8D$. The initial distance between the lowest point of the droplet and the pool level is $0.1D$. The length of the computation tank is $12D$. Only half of this impact problem is simulated by imposing a symmetry plane at $x = 0$. The rest of the lateral walls are assigned with free-slip plus no-penetration boundary condition. **Right:** We give an initial velocity U to the droplet, along with an impact angle α. The parallel component and the perpendicular component of the velocity (as defined in Eqn. (2.20)) are denoted as $U_{\parallel}$ and $U_{\perp}$ respectively. Velocity U is fixed as $U = 1$. The impact angle is varied from 10° to 75°, and the Weber number in our work covers the range $We \in [187.5, 1400]$ by changing the surface tension.

Sensitivity to Mesh Resolution In general, the researchers handling numerical simulations should pursue a high resolution to diminish the discretization error [83]. Nevertheless, we should take the high memory and the CPU time required as a consequence into account. Given a limited running time, the balance between the accepted mesh quality for our simulations and the computer resources available is of great significance to the present study.

To estimate the sensitivity of the cavity geometry to the spatial resolution, we carry out a benchmark simulation in an axisymmetric domain, where a droplet hits on a liquid pool with a velocity normal to the interface and $We = 300$. The mesh level increases from 9 to 12, i.e. resolution changes from 512^3 to 4096^3. Fig. 5.2a gives the cavity depth as a function of t^*. The temporal curves for mesh level 11 and level 12 almost coincide with each other. Furthermore, in Fig. 5.2b we present the maximum cavity depth as a function of mesh level, in which a convergence is observed when the grid is refined. We obtain an increase of 0.09% in the maximum depth when the grid is refined from mesh level 11 to 12. Therefore, we consider that the simulations performed with the mesh level 12 give a resolution-independent result for the cavity depth.

Besides the cavity geometry, also the influence of the resolution on the crown behavior is studied. In comparison to the cavity depth, the occurrence of crown breakup and the size of the splashing droplets is much more sensitive to the grid resolution [90, 91]. When the droplet is about to detach from the crown, a situation that two interfaces go through a single cell might happen. In this case, however, the interface cannot be correctly represented in our simulations due to the PLIC scheme (as described in § 3.2) used to reconstruct the interface. Also, the algorithm used to determine the curvature (i.e. the height function) will be invalid once the size of the splashing droplets is comparable to the cell dimension. Considering that the splashing cannot be correctly presented in an axisymmetric coordinate system, we carry out another benchmark simulation in the 3D geometry as described in § 5.1. We set a droplet which approaches a liquid pool with $We = 400$ and an impact angle $\alpha = 30°$. Fig. 5.3 presents the crown behavior in the different resolutions. We observe that the droplet size and its shape converge when the grid is refined. The crown shape and the splashing direction yielded from mesh level 11 and 12 is similar. Although a tiny droplet (which is highlighted by a circle in Fig. 5.3d) is still not properly resolved, the mass and the kinetic energy carried by this droplet are negligible in comparison to the total liquid. Besides, the splashing will move away from the impact region. Therefore, the effect from this unresolved droplet on the impact process is sufficiently small. Supported by the two simulations above, we consider that the mesh level 12 gives an acceptable accuracy of our numerical results with the computational resources available, and is applied in the following simulation for oblique droplet impact.

Results Comparison: Axisymmetric and 3D domain Before we carry out an oblique impact, we validate our 3D computational setup by using a benchmark simulation: the perpendicular droplet impact onto a pool. Later on, we measure the maximum cavity depth and compare them with the data collected from the axisymmetric domain (as described in chapter 4), see Fig. 5.4. We apply mesh level 11 to the 3D domain (instead of level 12 as mentioned above) for this benchmark in order to reduce the workload and run time. While the measurement is still reliable to validate the 3D domain considering that minor change in h_m from mesh level 11 to level 12. From the comparison, we obtain an agreement with a small deviation

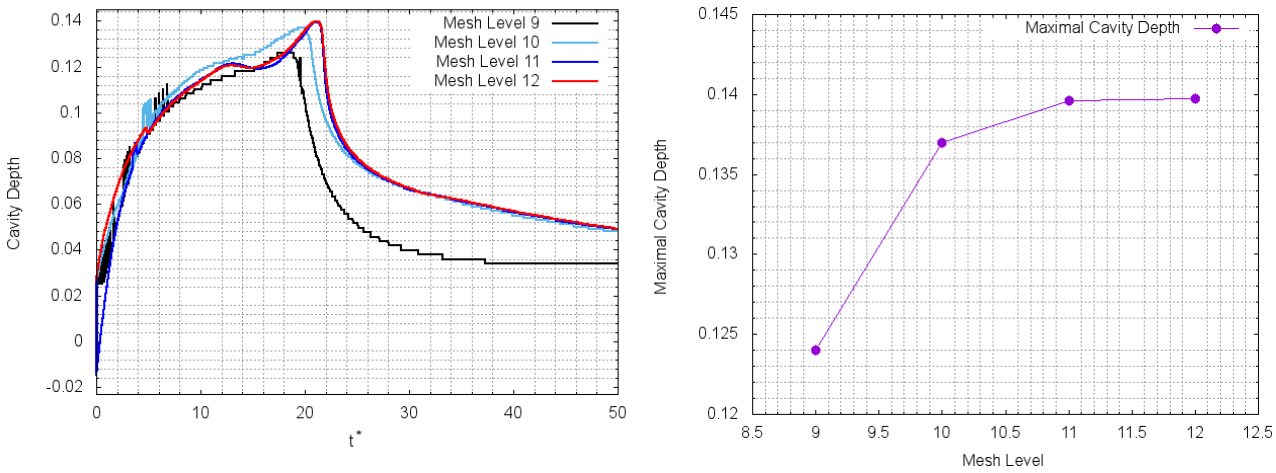

(a) **(b)**

Figure 5.2: Sensitivity of the cavity geometry to the spatial resolution. The analysis is based on a benchmark simulation, i.e. the perpendicular droplet impact on the liquid pool carried out in an axisymmetric domain. We vary the resolution while fix the Weber number $We = 300$. **(a):** Cavity depth as a function of t^* when we change the resolution. **(b):** Maximum cavity depth as a function of mesh level. We obtained a 0.09% increase in this maximum depth when the mesh is refined from level 11 to level 12.

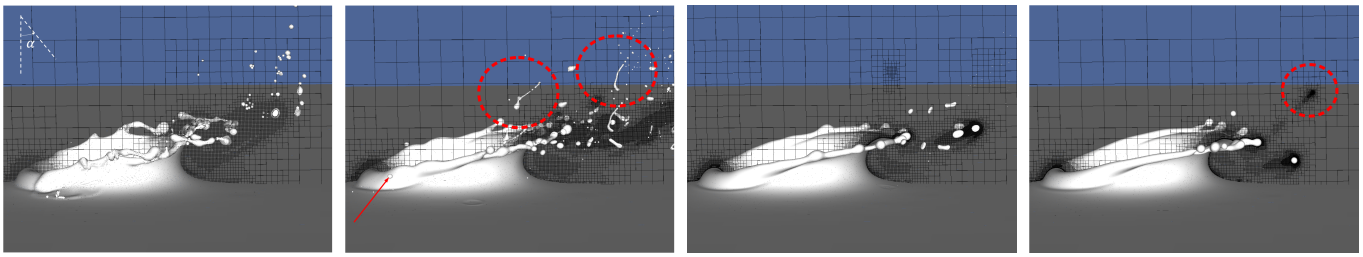

(a) **(b)** **(c)** **(d)**

Figure 5.3: Sensitivity of the crown behavior to the spatial resolution. The analysis is based on a benchmark simulation: an oblique droplet impact onto a liquid pool, with $We = 400, \alpha = 30^\circ$. **(a):** The crown behavior at mesh level 9. The peripheral rim of the crown shows a fluctuation in shape. Also, the grid is not dense enough to capture the splashing droplet accurately. The crown breakup occurs at an early time $t^* \approx 0.45$. On the trailing side, we observe splashing droplets flying with arbitrary directions. **(b):** The crown behavior at mesh level 10. With a higher resolution, the fluctuation in the rim shape is inhibited. Besides, liquid ligaments on the trailing side (as highlighted by red circles) and several tiny droplets on the leading side (as highlighted by an arrow) appear. **(c):** The crown behavior at mesh level 11. We observe a crown with a stable shape and a clear slope of the rim. By comparison, the liquid ligaments and the tiny droplets highlighted in panel (b) disappear. We also observe that the instant when the breakup starts is postponed ($t^* \approx 0.96$). **(d)**: The crown behavior at mesh level 12. The crown has a more smooth outline with an almost identical rim slope when compared to mesh level 11. The breakup droplets become more spherical, and the trigger moment t^* of the crown breakup is further postponed ($t^* \approx 1.15$). With the help of the mesh visualization on the symmetry plane, we still see a tiny droplet (highlighted by a dashed circle) moving in an arbitrary direction. The behavior of this drop could be explained as the invalidity of the algorithm accounting for the height function. As a consequence, Basilisk cannot correctly resolve the capillary force on this tiny drop when it detaches from the crown. See more information in the source code of Basilisk [1].

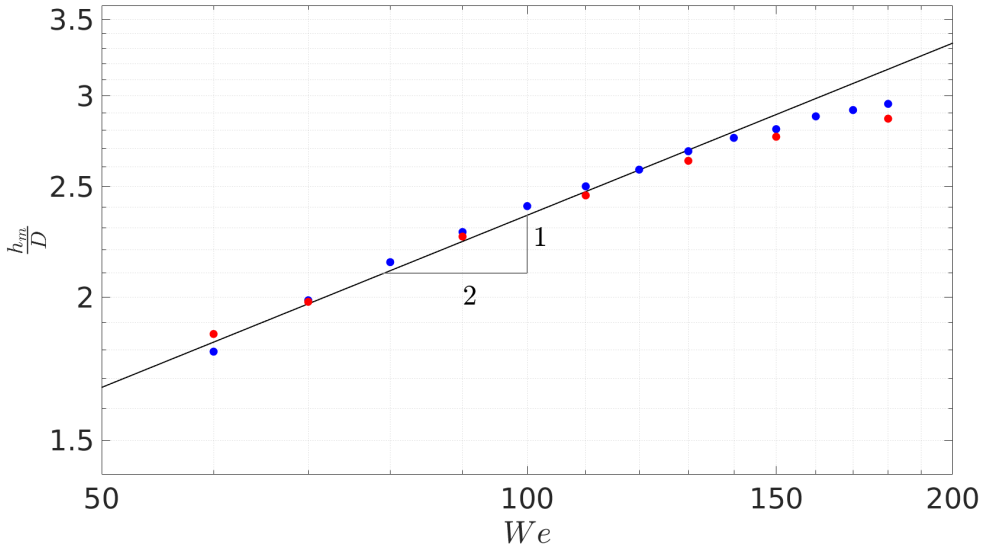

Figure 5.4: Double logarithmic plot of maximum cavity depth h_m (scaled by the droplet diameter D) as a function of Weber number for perpendicular droplet impact onto a liquid pool. The simulation results both from the axisymmetric domain (blue dots) in mesh level 11 and the three-dimensional domain (red dots) with mesh level 11 are plotted. The solid line has a slope of 1/2.

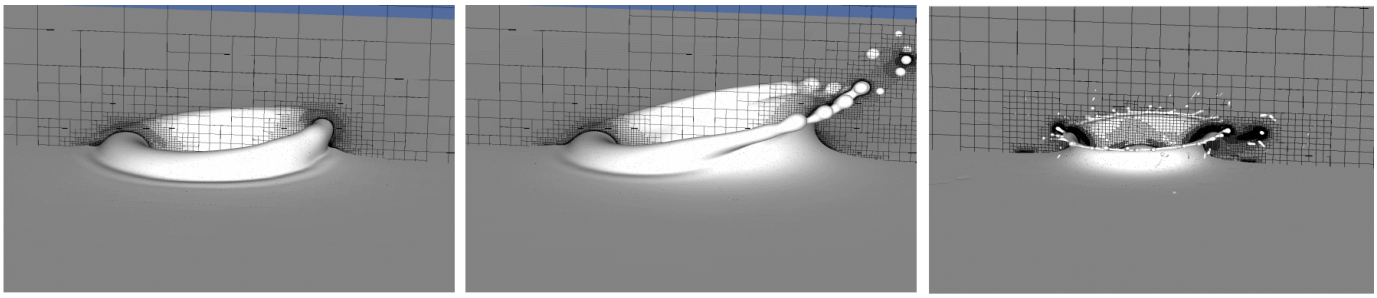

Figure 5.5: Three types of crown behavior observed in our simulations. From left to right: deposition, single-sided splashing, and omni-directional splashing. The impact parameters for the presented cases (from left to right): $We = 200, \alpha = 15°$; $We = 400, \alpha = 30°$ and $We = 600, \alpha = 10°$.

estimated as 0.8% of the data from axisymmetric domain. This difference could come from, for example, the dynamics refinement due to the different threshold value for the wavelet and spatial partition among the parallel cores. To conclude, the agreement between the numerical results verifies the validity of our 3D computational domain.

5.2 Crown Behavior

To study the crown behavior for the different Weber numbers and impact angles, we perform simulations with $We \in [187.5, 1400]$ and $\alpha \in [10°, 75°]$, see table 5.1. We regard the appearance of the breakup in the crown as the discriminant criterion between the deposition and the splashing. We provide qualitative characteristics of the crown in § 5.2.1, which will be quantified into a phase diagram in § 5.2.2.

5.2.1 Typical Features of Crown

As discussed in § 2.3, we expect three types of crown behavior after the droplet impact, see Fig. 5.5. First, the droplet could smoothly coalesce with the surface, which is identified as deposition. Second, given a larger Weber number or an impact more parallel to the surface, the crown destabilizes on the trailing side, leading to single-sided splashing. The third phenomenon is splashing occurs in all directions, indicated as omni-directional splashing.

Now we present a typical deposition crown observed in our simulations. As shown in Fig. 5.6, a droplet approaches

the pool with $We = 187.5$ and $\alpha = 26°$. Within the computational domain, we set two views with different angles: wide-angle-perspective as presented in panel (a.1) to (e.1), and top-view in panel (a.3) to (e.3). We use a color bar to indicate the height attained by the crown (positive in color bar), and the depth reached by the cavity (negative in color bar). After the droplet hits the surface, a distinct crown is ejected on the trailing side of the crater, see panel (a.1, a.3). As time goes by, two capillary waves along the peripheral rim of the crown are gradually visible (as indicated by arrows in panel (b.1, b.3) when $t^* = 2.1$). When $t^* = 5.5$, these waves collapse at the center of the trailing side, i.e. the symmetry plane of the computational domain, see panel (c.1, c.3). After the collapse, the capillary waves merge together, followed by a crown descent at $t^* = 10.1$, see panel (d.1, d.3). The time series of an experiment from [89] is presented from panel (a.2) to (e.2)), which has $We = 169, Re = 1210$ and $\alpha = 26°$. By comparing the crown shapes in the simulation and the experiment, an agreement in the crown behavior, such as the capillary wave on the peripheral rim (panel (b.2)) and the descent of the crown (panel (d.2)) is observed.

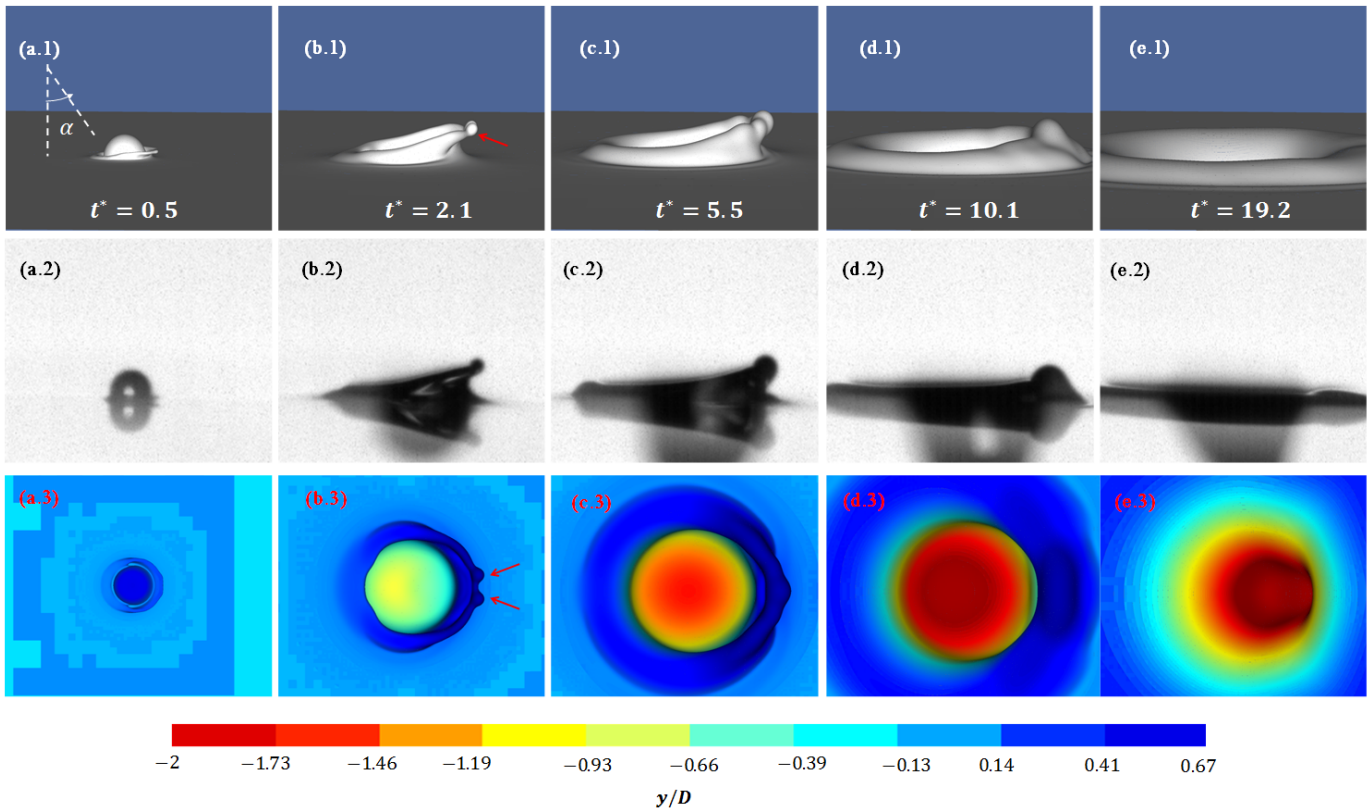

Figure 5.6: Time series of a deposition crown behavior ($We = 187.5, Re = 1000, \alpha = 26°$ for the simulation, and $We = 169, Re = 1210, \alpha = 26°$ for the experiment). The impact starts when $t^* = 0$. Panel (a.1)-(e.1): wide-angle-perspective; panel (a.2)-(e.2): experimental images from [89]; panel (a.3)-(e.3): top-view. A color bar (scaled by the droplet diameter) is used as a reference to indicate the height the crown reaches, and the cavity depth for panel (a.3) to (e.3). **(a):** When the droplet hits on the surface, a crown ejects on the trailing side of the crater. **(b)**: We can see two capillary waves developed on the crater rim, and they travel toward the center of the trailing side. This process is more evident when we look at the corresponding top-view panel (b.3). Both in panel (b.1) and (b.3) we use arrows to highlight these waves. **(c):** The capillary waves collapse at the symmetry plane, and merge with each other, forming a bump above the surface. **(d):** After the collision, the liquid bump falls down to the pool surface. **(e):** A capillary wave travels toward the cavity bottom. It can be distinguished by the red-color distribution in panel (e.3).

Then we increase the Weber number to $We = 400$ while the impact angle remains almost unchanged ($\alpha = 30°$ in this case). The observed crown is presented in Fig. 5.7. In comparison to deposition crown described in Fig. 5.6, a longer and more curved sheet is ejected on the trailing side when the droplet contacts the pool, see panel (a.1). A more angular rim highlighted by arrows in panel (a.3) exhibits the vibrancy of the crown. Due to the capillary instability (as discussed in § 2.3.2), the crown on the trailing side develops into several fingers, which, at a later time, break into a number of droplets. Hence a splash is visible, see panel (b.1) to (c.1) and panel (b.3) to (c.3). After the last droplet detaches from the crown, a liquid bump is produced which is highlighted by a dashed circle in panel (d.1). This bump is pulled back to the pool by the capillary force (panel (e.1)). We present an experimental case with $We = 416, Re = 1904$ and $\alpha = 26°$ in panel (a.2) to (e.2) [89]. Several features of the crown behavior, such as the detachment of the droplets (panel (c.2)) and the final

liquid bump (panel (d.2)), are captured by our simulation. When the droplet moves more perpendicular to the surface, the crown velocity in all directions could exceed the critical value for splashing (see the discussion in § 2.3.2). The simulations for omni-directional splashing are still at the early stage. Hence we lack a complete time series to show the evolution of the crown for this case. However, we can still identify the crown behavior based on the clear breakup visible around the crown (as shown in Fig. 5.5).

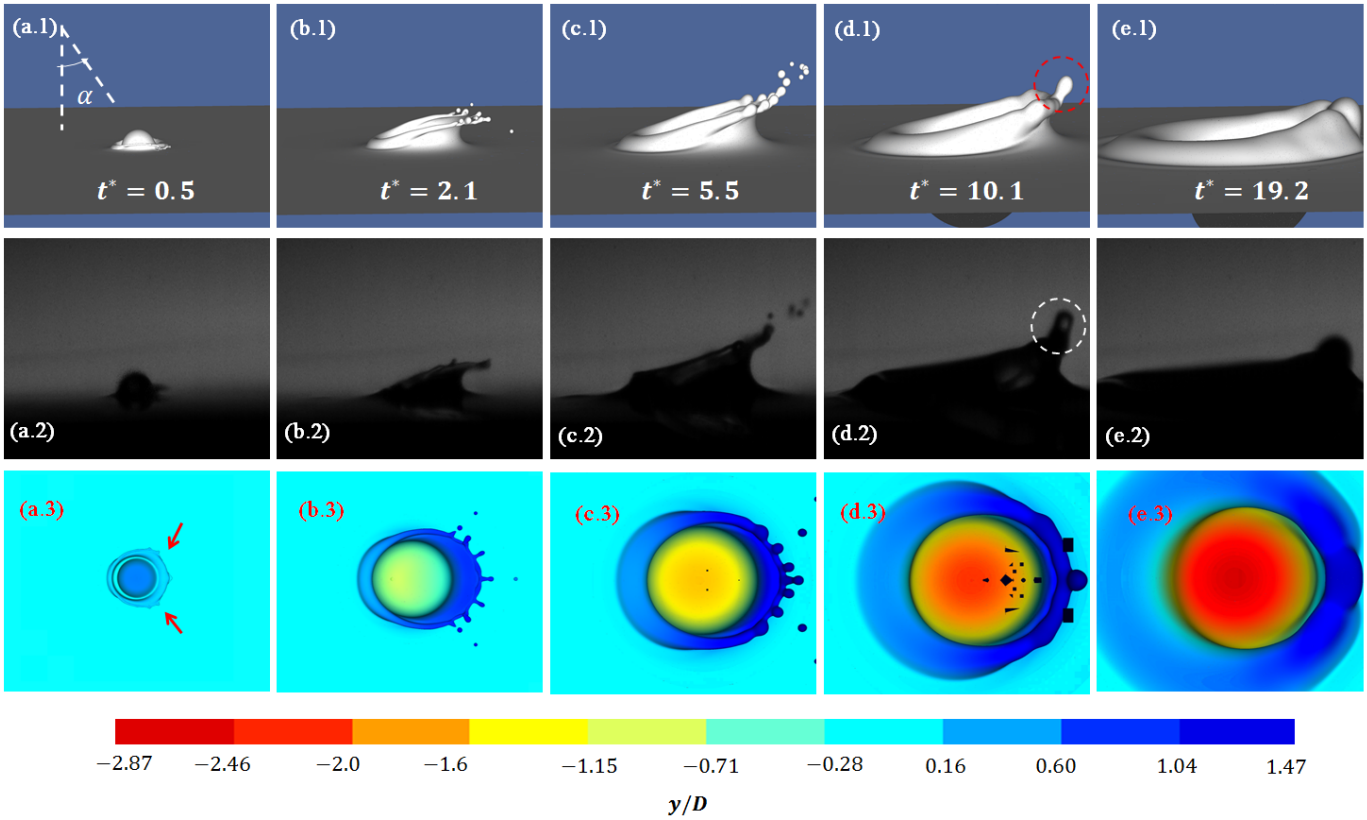

Figure 5.7: Time series of a single-sided splashing crown behavior ($We = 400, Re = 1000, \alpha = 30°$ for simulations and $We = 416, Re = 1904, \alpha = 26°$ for the experimental case). Panel (a.1)-(e.1): wide-angle-perspective; panel (a.2)-(e.2): experimental images from [89]; panel (a.3)-(e.3): top-view. **(a):** After the contact between the droplet and the interface, a more curved and longer sheet (by comparison with Fig. 5.6a) is ejected on the trailing side. From the top-view at this moment, we observe a more angular shape of the crown rim, highlighted by the red arrows in panel (a.3). **(b):** The capillary instability is triggered on the peripheral side of the rim, leading to several breakup droplets. **(c):** The crown expands at this moment, with a more distinct splashing. **(d):** After the final droplet detach from the crown, a liquid bump is formed, and it is highlighted by a circle both in panel (d.1) and panel (d.2). **(e):** The liquid bump falls back to the pool by the capillary force.

5.2.2 Phase Diagram

We quantify the crown behavior observed in our simulations into a phase diagram of the Weber number and the impact angle, see Fig. 5.9. With the fixed Reynolds number ($Re = 1000$) in our simulation, the threshold (2.33) can be rewritten as

$$We^{1/2}(cos\alpha^{5/4})(1 \pm c \cdot tan\alpha) > \frac{K}{1000^{1/4}}, \tag{5.1}$$

where K is the critical splashing number, and c is the fitting parameter. Then Fig. 5.9 is divided into three different regions: deposition, single-sided splashing and omni-directional splashing by (5.1). From (5.1) it follows that the value of K can be determined from critical Weber number We_c for the perpendicular impact ($\alpha = 0°$), i.e. $K = We_c^{1/2} Re^{1/4}$. As shown in Fig. 5.8, our simulation captures the transition from deposition to splashing when $We_c \in (335, 350)$, leading to $K = 104 \pm 1.2$, while $K \approx 130$ is obtained from [71]. In our simulations, the value of K is influenced not only by the spatial resolution but also other numerical parameters, such as the time step and the convergence criterion for the Poisson equation. Furthermore, the K value in the experiments is sensitive to ambient interference, say the change of the air temperature in the laboratory, or the surface roughness due to the wave on the pool interface. Instead, in the simulations we neglect the effect from the surrounding vapor on the impact process, and the pool surface is perfectly flat. For the reasons given above, we do not

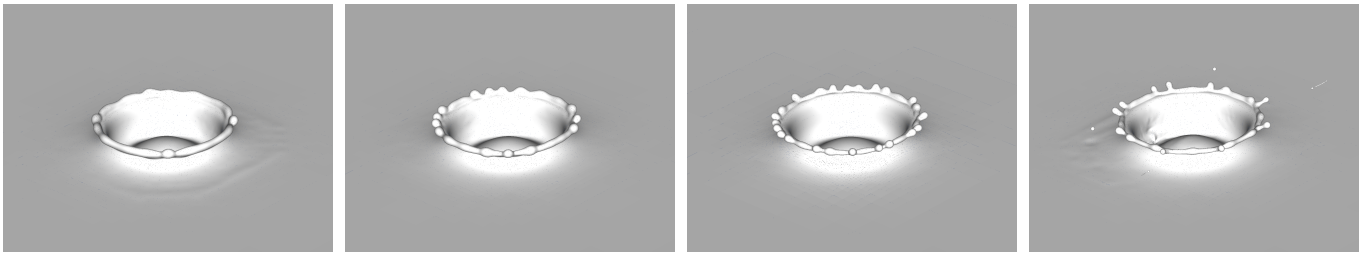

(a) $We = 250$. **(b)** $We = 275$. **(c)** $We = 335$. **(d)** $We = 350$.

Figure 5.8: Transition from deposition to splashing for the perpendicular droplet impact. Under the numerical parameter in this work, this transition is captured in $We \in (335, 350)$, which gives $K \approx 104 \pm 1.2$ in Eqn. (5.1).

surprised by the difference of K under our numerical setting as compared to the experiments. The fitting parameter c in (5.1) accounts for the mass redistribution among the crown. In [71] $c = 0.44$ is determined, which is adopted in the present study.

In Fig. 5.9 we plot (5.1) using $K = 104$ and $c = 0.44$. A solid line stands for the transition from deposition to single-sided splashing (when (5.1) takes plus), and a dashed line discriminates between single-sided splashing with omni-directional splashing (when (5.1) takes minus). Our numerical results show an agreement with (5.1) in the middle of three regions, while three points near the boundary between deposition and single-sided splashing show a deviation from (5.1). This disagreement could come from the sensitivity of the crown, especially the occurrence of the breakup, to the numerical parameters.

We also plot our numerical results and the experimental data from [71] into one phase diagram. As discussed in 2.3.2, the splashing threshold is defined by not only the Weber number but also the Reynolds number. In contrast to the simulations where $Re = 1000$, in the experiments Re and We are varied simultaneously when the droplet velocity is changed. Also, we should take different values of K in the experiments and the simulations into consideration when carrying out the comparison. Therefore, we quantify the crown behavior of the simulations and the experiments into a phase diagram of $Re^{1/4}We^{1/2}K^{-1}$ and α, which is shown in Fig. 5.10. Although we have three numerical results which deviate from (2.33), an agreement is obtained in the comparison with the experimental data both in the bulk region and the transition boundaries. Besides, in the experiment an overlap region for all the three crown behaviors is observed for $Re^{1/4}We^{1/2}K^{-1} \approx 1$ and $\alpha < 20°$, and we see single-side splashing (red upward-triangle) appears in omni-directional region (black upward-triangle). The simulation results, however, clarified this vague area.

5.3 Cavity Angle

We now turn to the phenomena below the interface. In our simulation, we use three parameters which define the shape of the cavity: the cavity angle α_c, cavity depth h, and displacement d. As shown in Fig. 2.6, these parameters are related by (2.21).

5.3.1 Evolution of Cavity Angle

After the droplet impact, the deepest point of the cavity will be developed on the leading side at first, see § 2.3. As a consequence, the cavity angle α_c lies in the range $\alpha_c < 90°$ at the beginning and increases to $\alpha_c > 90$ over time. This dynamic trend is captured by our simulation. In Fig. 5.12 we present the impact angle α_c as a function of t^* for several simulations, for the impact parameters in table 5.1. We observe that the growth of the cavity angle can be divided into three periods, and we name them inertial-growth, saturation-period, and capillary-retraction, respectively, see Fig. 5.11. After droplet impact, the cavity angle experiences a rapid increase in inertial-growth. During this period we have $t \ll t_\gamma$ where the capillary time t_γ scales with $t_\gamma \sim \sqrt{\rho_l D^3/\gamma}$. Parameter t_γ can be regarded as a response time for the capillary force, which is, for example, the time scale of oscillation of a freely released droplet with a diameter D and mass $\rho_l D^3$ [50]. From $t \ll t_\gamma$ it follows that the influence of the inertial force prevails the capillary force in the period of inertial-growth. Later on, the increase of the cavity angle is slowed down by the surface tension. As time goes on, α_c attains a local maximum α_i and reaches saturation-period, in which the cavity angle remains a relatively stable value. We name α_i inertial angle. At the

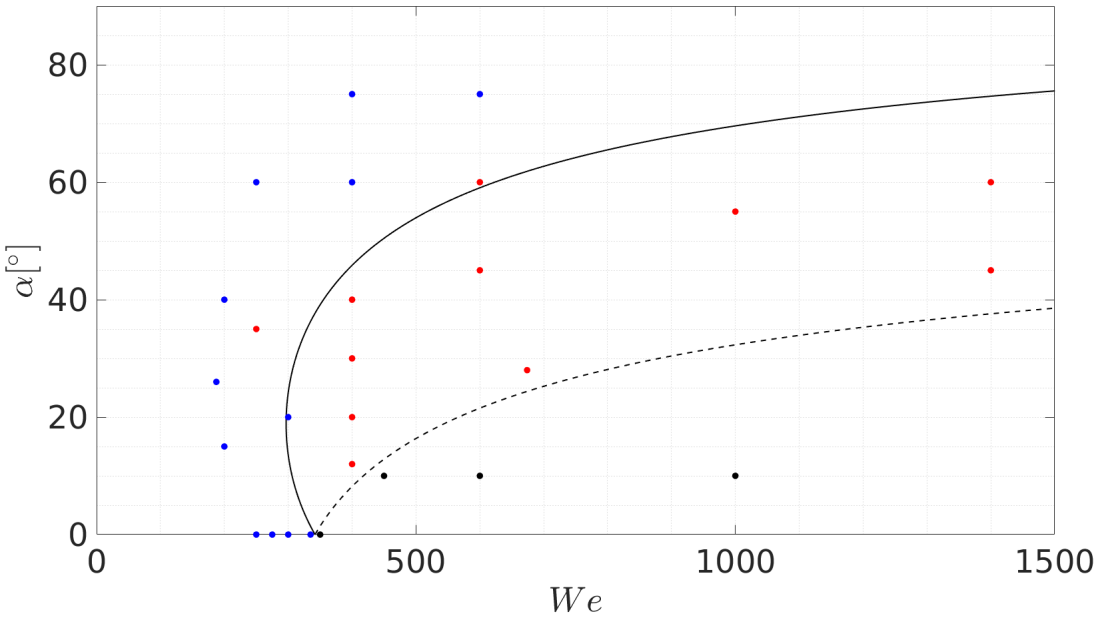

Figure 5.9: The phase diagram of the crown behavior as a function of the Weber number and the impact angle. Eqn. (5.1) using $K = 104, c = 0.44$ is indicted by a solid line (with a plus sign in Eqn. (5.1)) which represents the transition between deposition and single-sided splashing, and a dashed line (with a minus sign in Eqn. (5.1)) discriminating between single-sided and omni-directional splashing. We quantify the phenomena as: deposition (blue dots); single-sided splashing (red dots); omni-directional splashing (black dots).

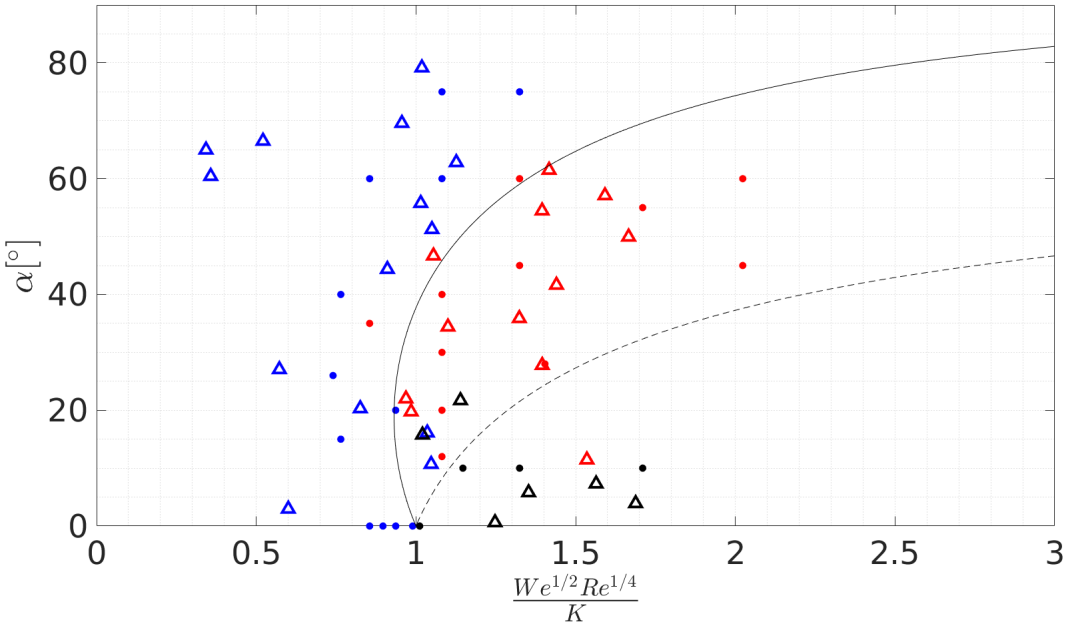

Figure 5.10: The phase diagram of the crown behavior as a function of $Re^{1/4}We^{1/2}K^{-1}$ and α. Dots present the numerical data, and upward-triangle are experimental data from Gielen et al. [71], with different colors — blue: deposition; red: single-sided splashing; black: omni-directional splashing. Note that the experimental data has been clustered for an easy observation.

Table 5.1: Impact parameters for the simulations performed and the corresponding remarks on the crown behavior observed.

Crown behavior in simulations	Name	We	Re	α	Remarks
Numerical Single-sided splashing	Intersection1	400	1000	40°	n/a
	s1	400	1000	30°	n/a
	s2	1400	1000	60°	n/a
	s3	1400	1000	45°	n/a
	s4	600	1000	45°	n/a
	s7	400	1000	20°	almost omni-directional
	s9	600	1000	60°	expected deposition
	d10	250	1000	35°	expected deposition
	Intersection3	400	1000	12°	almost omni-directional
	s5	1000	1000	55°	n/a
	Duplicate	674	1000	26°	n/a
Numerical Deposition	Intersection2	300	1000	20°	expected single-sided splashing
	d1	187.5	1000	26°	n/a
	d3	400	1000	75°	ripple-crown
	d4	250	1000	60°	ripple-crown
	d5	400	1000	60°	ripple-crown
	d6	600	1000	75°	ripple-crown
	d8	200	1000	40°	n/a
	d9	200	1000	15°	n/a
Numerical Omni-directional splashing	o1	600	1000	10°	n/a
	o2	800	1000	20°	n/a
	o3	450	1000	10°	almost single-sided splashing

later time of saturation-period, we observe a slight increase in the cavity angle, followed by another maximum α_{cm}. Next, the cavity angle decreases in capillary-retraction period.

From a view below the pool surface, we can find the cavity geometry corresponding to the different periods. We take case **d1** ($We = 187.5, \alpha = 26°$) as an instance, see Fig. 5.11. Starting with the period of inertial-growth, the increased surface energy is not enough to counteract the kinetic energy. Consequently, the droplet is squeezed around due to the remaining velocity, see the velocity vector field presented in panel (1). As a result, depression is produced on the leading side of the pool surface, resulting in $\alpha_c < 90°$. Within this stage, the droplet gradually penetrates into the pool with a penetration velocity U_p. Several studies point out $U_p \approx U/2$ for perpendicular droplet impact onto a target with an identical liquid at the initial stage, resulting in $t^* \approx 2$ when $h/D \approx 1$ [24, 29, 51, 92]. As indicated by the velocity vector, for oblique impact the droplet penetrates along the impact direction. During this process, the velocity around the cavity bottom (i.e. the deepest point of the cavity) is curved toward the direction normal to the impact direction, which impedes the development of the penetration velocity perpendicular to the surface $U_{p,\perp}$. The value of $U_{p,\perp}$ hereby is smaller than the $\frac{U_\perp}{2}$. Hence we expect $t^* = \frac{t}{D/U_\perp} > 2$ when $h/D \approx 1$ for oblique impact. In our simulations, we obtain $t^* = 2.65 \pm 0.15$ for $\alpha \in [15°, 60°]$. After inertial-growth, the cavity angle reaches inertial angle α_i. Then the cavity angle steps into saturation-period, see panel (2). Within this stage, we observe that the cavity keeps a hemispherical shape along with a displacement d with respect to center line. During this period $\alpha_c \approx \alpha_i$. At the tail of saturation-period, we see an increase in the cavity angle. This is caused by the traveling of the capillary waves, which deforms the cavity shape (panel (3)). When the waves meet at the cavity bottom with a cavity angle α_{cm} as shown in panel (4), we observe a rapid retraction of the cavity tip due to a high local curvature and consequent capillary force (panel (5)). The sequence described above of the cavity captured by our simulation shows an agreement with the experiment from [89], see Fig. 5.13.

5.3.2 Collapse Angle

As pointed out in § 2.3, the collapse angle α_{cm}, i.e. the cavity angle when the capillary waves meet at the cavity bottom, is associated with the direction of the following Worthington jet, which should be eliminated by an intelligent design for the vanes in the EUV chamber. Hence, we have a direct interest on the value of α_{cm}. As described in Fig. 5.11, there are typically two local maxima for the cavity angle: inertial angle α_i and collapse angle α_{cm}. Due to the undesirable scalability

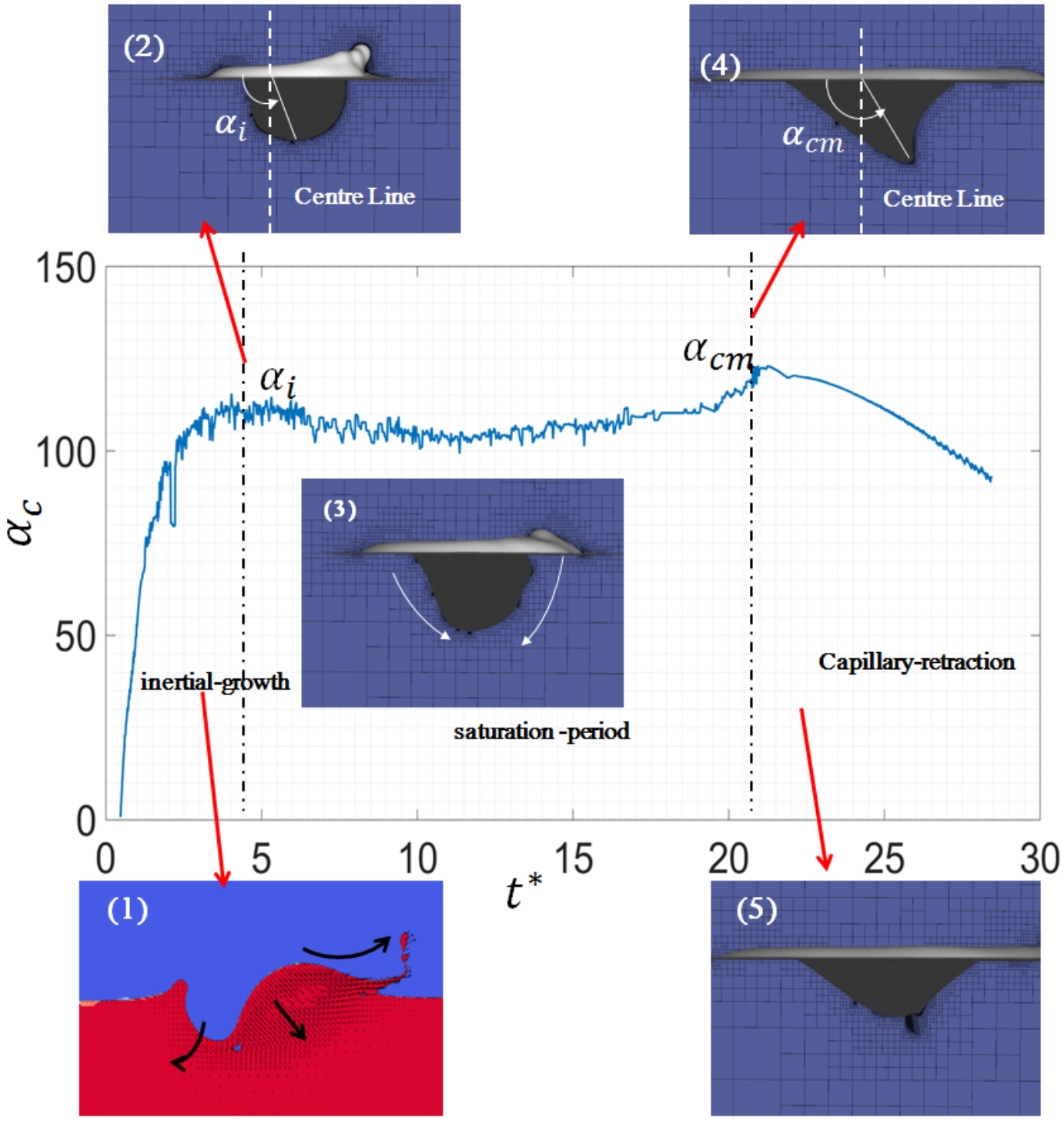

Figure 5.11: Evolution of the cavity angle α_c (central panel), and the cavity shape at the corresponding moments (panel (1) to (5)). The impact has $We = 187.5, \alpha = 26^\circ$. **(Central panel):** Plot of α_c as a function of t^*. **(1):** The velocity vector field at the symmetry plane when α_c is in inertial-growth period. The droplet liquid is squeezed around, resulting in a depression in the leading side of the surface, which accounts for $\alpha_c < 90^\circ$ in this period. **(2):** Later on a hemispherical cavity is developed, with a horizontal displacement in respect of the center line. The cavity angle reaches inertial angle α_i, and goes into saturation-period. **(3):** During the saturation-period, the impact angle has a gentle change. Then the capillary waves are visible along the lateral walls of the cavity. They are highlighted by arrows. The travel of these waves deforms the cavity shape and leads to an increase in α_c. **(4):** The waves encounter with each other, and the cavity angle reaches α_{cm} at this moment. **(5):** The high local curvature in the cavity tip produce a large capillary force, which pulls the cavity upward, and generates an upward jet in the meantime (not visible in figure).

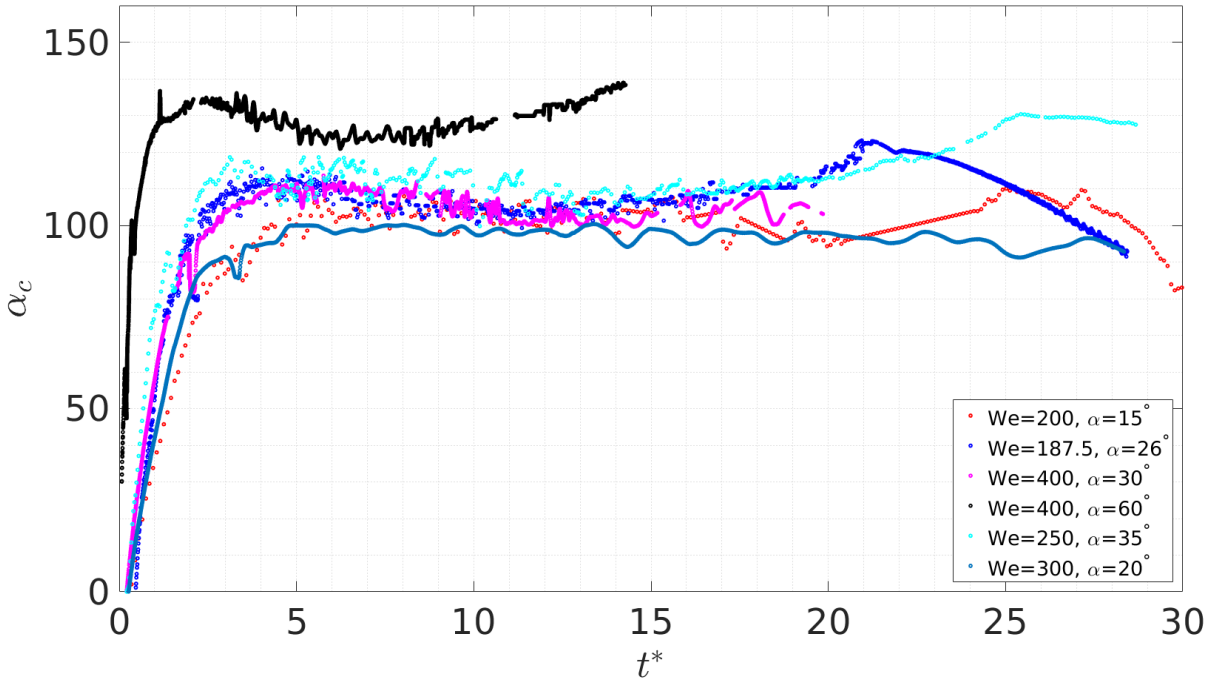

Figure 5.12: Cavity angle α_c as a function of t^*. The cavity angle α_c experiences a rapid increase at the initial stage. Due to the surface tension the increase of α_c is slowed down and almost remains constant over time. Then the cavity angle reaches a maximum when the cavity collapses.

Table 5.2: Collapse angle α_{cm} and the inertial angle α_i for the cases which have reached the collapse moment.

Name	*We*	α	*Re*	α_i	α_{cm}
d1	187.5	26°	1000	(111±0.13)°	(121±0.12)°
d9	200	15°	1000	(103±0.23)°	(109 ±0.13)°
d5	400	60°	1000	(132 ±0.02)°	(138±0.01)°
d10	250	35°	1000	(115 ±0.78)°	(129±0.16)°
intersection2	300	20°	1000	(101 ±0.13)°	(112±0.11)°
s1	400	30°	1000	(114 ±0.23)°	(121±0.05)°

of the simulations, at the time of writing only six impact cases reach the collapsing moment, see table 5.2. Therefore we take α_i as an approximation for α_{cm} with a deviation approximated to 7.4% of α_{cm} for uncompleted simulations. The difference between α_i and α_{cm} is primarily caused by the traveling of the capillary waves accounting for a deformation of the cavity. Fig. 5.14 plots the collapse angle α_{cm} as a function of $(\alpha+90°)$. We present the numerical results and the experimental data from [71] with the corresponding error bars, and we observe that $\alpha_{cm} \approx \alpha + 90°$. However, as α increases ($\alpha \gtrapprox 35°$) we see a deviation between α_{cm} and $(\alpha+90°)$. This could be explained that when the droplet approaches parallel to the pool surface, more kinetic energy, especially the parallel component, will be transferred to the crown above the interface. The impact with a large impact angle will produce a ripple spreading on the trailing side of the crown (i.e., ripple-crown in the remarks of table 5.1), which largely dissipates the kinetic energy of the droplet, see Fig. 5.15. As a consequence, the parallel momentum converted to the cavity surface (which accounts for the cavity displacement) is decreased, leading to a smaller collapse angle as compared to $(\alpha+90°)$.

5.4 Cavity Dimensions

In this section we chronologically present a study of the cavity depth h (§ 5.4.1, § 5.4.2), and the cavity displacement d (§ 5.4.3). As defined in 2.6, the cavity depth is the vertical distance from the deepest point in the cavity to the initial

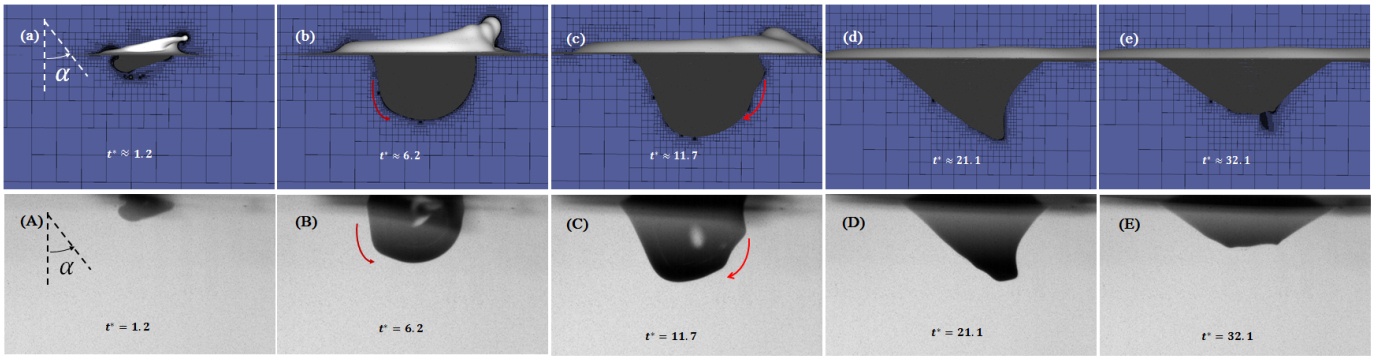

Figure 5.13: Time series for the impact cavity in the simulations (top row), and the comparison with the experiments (bottom row, images taken from [89]). Impact parameters for the simulation: $We = 187.5, We = 1000, \alpha = 26°$. Impact parameters for the experiment: $We = 169, Re = 1210, \alpha = 26°$. **(a, A):** When $t^* = 1.2$, the deepest point of the cavity is visible in the leading side. **(b, B):** When $t^* = 6.2$, we see a capillary wave, as indicated by an arrow, traveling from leading side toward the cavity bottom. **(c, C):** When $t^* = 11.7$, a more pronounced capillary wave is visible. It moves from the trailing side toward the cavity bottom. **(d, D):** At the moment of $t^* = 21.1$, the capillary waves collapse at the cavity bottom. **(e, E):** When $t^* = 32.1$, the cavity tip retracts after the collision of the waves.

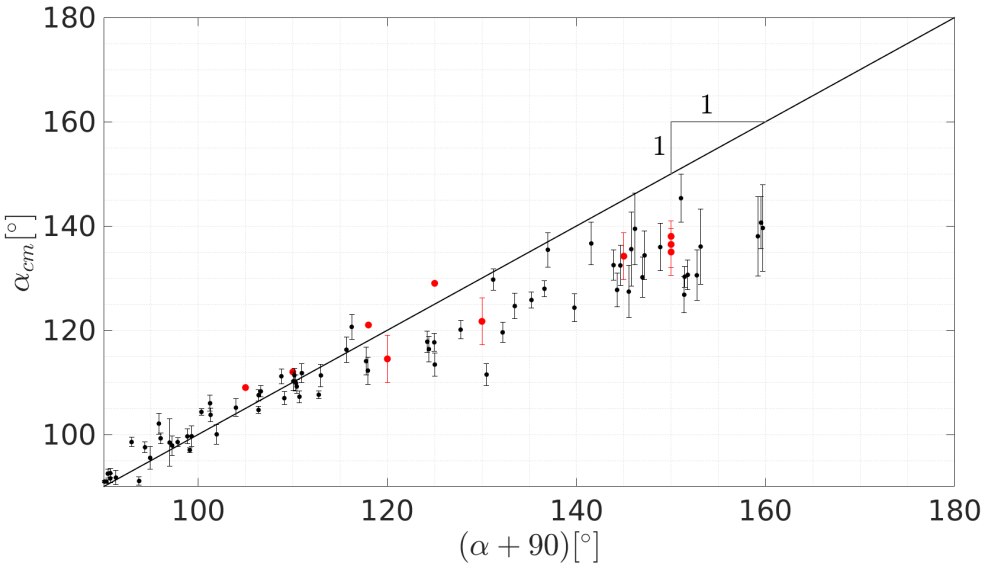

Figure 5.14: Collapse angle α_{cm} as a function of $(\alpha + 90°)$. The solid line presents $\alpha_{cm} = (\alpha + 90°)$. We present the experimental data from [71] by black dots with the corresponding error bars, and present the simulation results by red dots. For the completed simulations (see table 5.2), the error bars indicate the standard deviation, while the error bars for the rest of the simulations stand for the error introduced when we use $\alpha_{cm} \approx \alpha_i$. We observed that when the impact angle increases, the value of α_{cm} gets smaller when compared to $(\alpha + 90°)$. This deviation is also captured by the experiment in [71] (see the description of Eqn. (2.22). This phenomenon could be explained that when the impact becomes more parallel to the surface, more kinetic energy will be converted to the ripple on the trailing side instead of benefiting the growth of the cavity displacement, see Fig. 5.15.

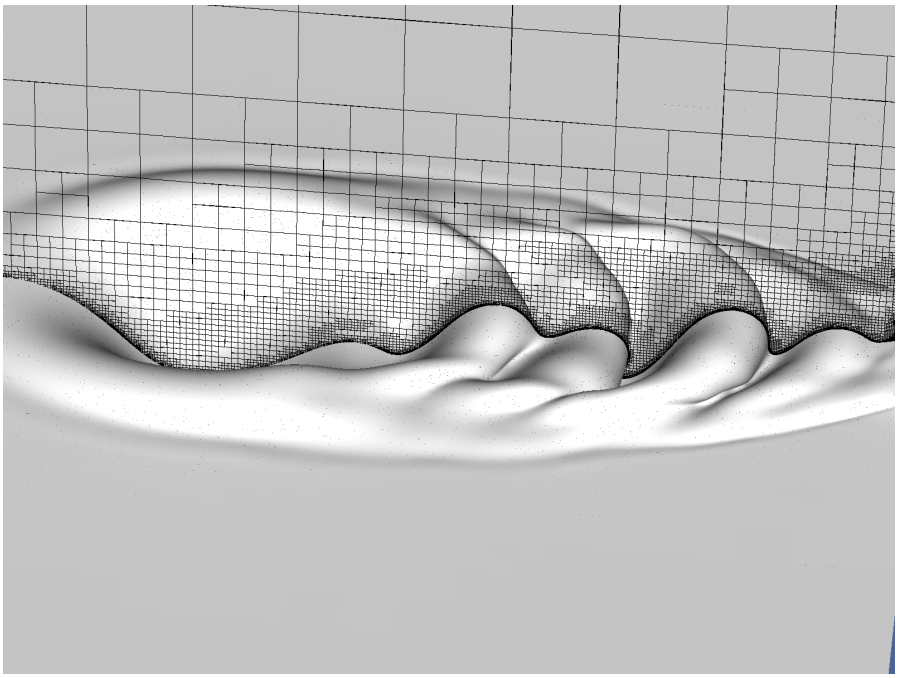

Figure 5.15: Ripple developed on the trailing side of the crown. The impact has $We = 600$ and $\alpha = 75°$. This distinct rippled dissipates the parallel component of the droplet momentum, hence weakens the development of the cavity displacement.

surface, and displacement is the horizontal distance from the deepest point to the center line. During the simulations we track this deepest point. Hence we can obtain the temporal functions for the depth and the displacement, i.e., $h(t)$ and $d(t)$ respectively. Besides, we extract the maximum cavity depth h_m, and the displacement when the cavity collapse, that is, d_m.

5.4.1 Depth Evolution

In Fig. 5.16, the cavity depth h is plotted as a function of t^*. The data suggests that $h/D \approx 0.45(5t^* - 6)^{2/5}$ (black-solid line) at the early stage of impact. This result can be explained by the observation in our simulation. As shown in Fig. 5.17b, for small impact angle ($\alpha \lessapprox 40°$) we observed that the cavity remains a hemispherical shape in the relatively long saturation-period until capillary waves appear. The expansion of this hemispherical cavity is similar to the perpendicular case which is approximated as an expansion hemisphere in most of the relevant models [29, 51, 53, 54], see Fig. 5.17a. In [52], the flow around the crater at the perpendicular case is assumed irrotational. This assumption has been validated by several numerical and experimental studies [29, 51, 53]. Bisighini et al. [29] point out that the vorticity produced at the pool surface can be neglected given $Re \sim 1000$, which is the case in our flow. We hereby assume an irrotational flow for the oblique impact with a small impact angle. As a result, the flow can be characterized by a potential field ϕ, from which the velocity can be determined by $\mathbf{u} = \nabla\phi$. In the range of $\alpha \lessapprox 40°$, the displacement is small as compared to the expansion dimension ($d(t) \leqslant 0.37h(t)$ during saturation-period). Therefore, we propose that the spherical expansion approximation for the cavity is still applicable for the oblique impact with small impact angle. Following the work of [29, 51], we now describe $h(t)$ for perpendicular impact and interpretation on Fig. 5.16.

In [51] it is pointed out that the center of hemispherical cavity is fixed at the impact point if we ignore the influence of the gravity, which is the case in our flow. Therefore we obtain the potential field around the crater by analogy with an expanding bubble

$$\phi = -\frac{h^2}{r}\dot{h} \quad \text{and} \quad \dot{h} = \frac{dh}{dt}, \tag{5.2}$$

where r is the radial component of the coordinate system plotted in Fig. 5.17a. From (5.2) it follows

$$u_r = \frac{h^2}{r^2}\dot{h}, \quad u_\phi = 0, \quad u_\theta = 0. \tag{5.3}$$

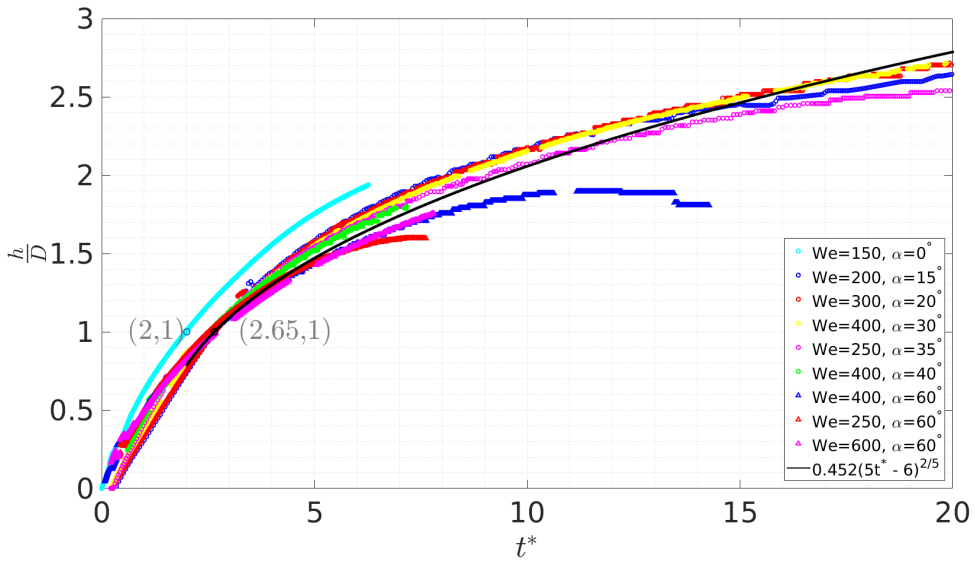

Figure 5.16: Cavity depth h (scaled by the droplet diameter D) as a function of t^* for a wide range of Weber numbers and the impact angles. The black-solid line presents Eqn. (5.9) with $C_1 = 0.45$ and $C_2 = 6$. The value of C_1 is determined from the initial condition $t^* = 2.65 \pm 0.15, h/D = 1$ (as located by a circle). Note that for perpendicular impact, its evolution line goes through $t^* = 2, h/D = 1.01$, which is close to the theoretical penetration depth $h/D \approx 1, t^* \approx 2$ (as located by a circle) proposed in [29, 51, 92].

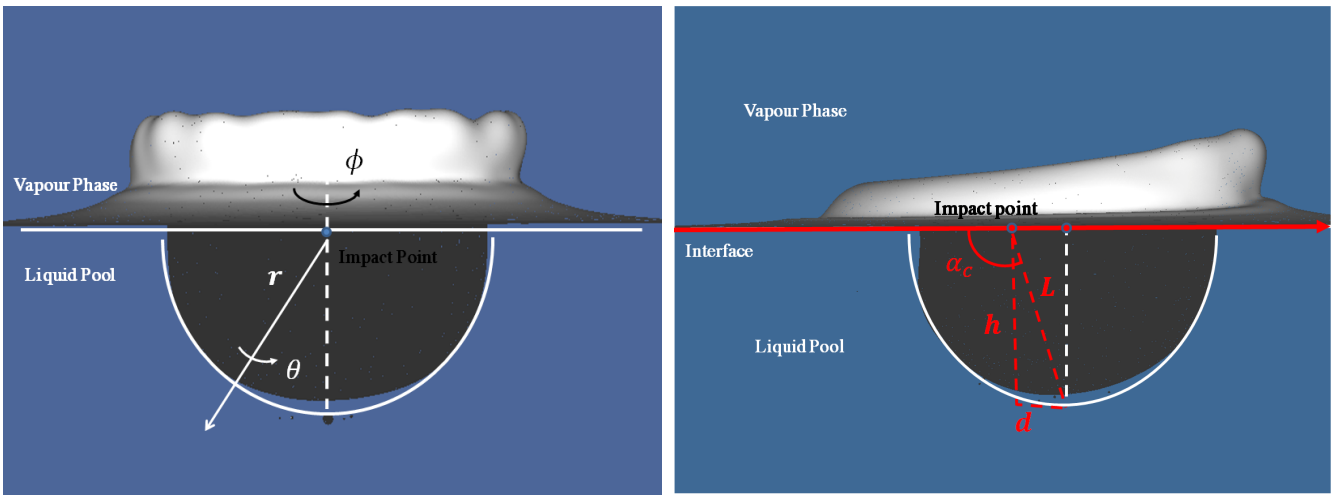

(a) **(b)**

Figure 5.17: Superposition of recorded images from our simulations and a hemispherical geometry. **(a):** Sketch for the droplet perpendicular impact on a liquid pool. The cavity evolution is approximated as an expanding sphere. We set a spherical coordinate system (r, ϕ, θ) with its center fixed at the impact point. **(b):** Sketch of an oblique droplet impact on the pool with small impact angle. From the simulations we observe a hemispherical cavity in saturation-period for $\alpha \lessapprox 40°$. Note that the parameters which define the cavity geometry: cavity depth h, displacement d, characteristic length L and the cavity angle α_c have been indicated in the figure. As compared to $h(t)$, the magnitude of $d(t)$ is always small ($d(t) \leqslant 0.37h(t)$).

From the Bernoulli equation

$$\frac{\partial \phi}{\partial t} + \frac{1}{2}(\nabla\phi \cdot \nabla\phi) + \frac{p}{\rho_l} = f(t) \tag{5.4}$$

where $f(t)$ is a sole function of time, we obtain the pressure distribution on the cavity surface ($r = h(t)$)

$$\frac{p_{ca}}{\rho_l} = \ddot{h}h + \frac{3\dot{h}^2}{2}. \tag{5.5}$$

Note that in (5.5) we have considered $f(t) = 0$, which can be shown from (5.4) when applying that $\phi \to 0$, $\mathbf{u} \to 0$, $p \to 0$ at $r \to \infty$. If we assume that the pressure at the free surface is zero, we can obtain

$$\frac{p_{ca}}{\rho_l} = -\frac{2\gamma}{\rho_l h} = -\frac{2}{We}\frac{U^2}{h^*}, \tag{5.6}$$

in which the right-hand-side is the pressure jump accounts for the surface tension with $h^* = h/D$. Combining (5.5) and (5.6) we get

$$\ddot{h}^* = -\frac{3}{2}\frac{(\dot{h}^*)^2}{h^*} - \frac{1}{We}\frac{2}{h^{*2}}, \tag{5.7}$$

In [51] it is proposed that term $\frac{1}{We}\frac{2}{h^{*2}}$ is negligibly small in comparison to the other terms in (5.7) if $We \gg 1$, hence (5.7) can be reduced to

$$\ddot{h}^* = -\frac{3}{2}\frac{(\dot{h}^*)^2}{h^*}. \tag{5.8}$$

The analytical solution of (5.8) can be determined as

$$\frac{h}{D} = C_1(5t^* - C_2)^{2/5}, \tag{5.9}$$

where constants C_1, C_2 are estimated from the initial conditions. In [51] $C_1 = 0.57$ and $C_2 = 6$ is obtained and the solution is validated by an agreement with the experimental data. In Fig. 5.16 we plot (5.9) using $C_2 = 6$. We use $C_1 = 0.45$ based on the initial condition $h/D \approx 1$ when $t^* = 2.65 \pm 0.15$ (see the discussion in § 5.3). Note that we also plot the cavity depth for the perpendicular impact in Fig. 5.16, which goes through the location $t^* = 2, h/D = 1.01$. This result is consistent with the penetration velocity pointed out in [29, 51, 92]. From Fig. 5.16 the numerical results show a deviation from (5.9) over time, which is expected since the appearance of the capillary waves accounting for a cavity deformation. As a result, the assumption of a spherical shape for the cavity is invalid. Besides, there is no decay term in the exponential of (5.9), suggesting that the predicted cavity depth approaches infinity as time goes by. This output is obviously in contrast to the physical reality, in which the cavity expansion will be slowed down by the surface tension, and finally a maximum cavity depth h_m will be attained. If we increase the impact angle (typically $\alpha \gtrapprox 60°$), a more evident displacement is visible due to a larger parallel momentum. The cavity will be stretched in the direction parallel to the pool surface, leading to a cone-shaped cavity, see Fig. 5.18. Hence the cavity cannot be approximated as a hemisphere anymore. This deformation could account for the deviation visible in Fig. 5.16 for big impact angle.

5.4.2 Maximum Cavity Depth

The maximum cavity depth h_m is defined by the competition between the surface tension and the kinetic energy. As discussed in § 2.3.1, by using the energy argument (2.23) we expect that h_m scales as $We_\perp^{1/2}$ where $We_\perp = \frac{\rho_l D U_\perp^2}{\gamma}$. This scaling shows that the vertical dimension (i.e. the cavity depth) is primarily characterized by the perpendicular momentum $U_\perp$, which is consistent with our assumption in 5.4.1. In Fig. 5.19 the maximum cavity depth h_m is plotted as a function of $We_\perp$. The experimental data from [71] is compared with the simulation. We get an agreement in the comparison concerning the magnitude of h_m/D and the scaling law $h_m/D \sim We_\perp^{1/2}$, although the number of the numerical data we present is subject to the running time of the simulations.

5.4.3 Cavity Displacement

The parallel momentum of the droplet accounts for the formation of the displacement d. For small impact angle, the displacement is always small in comparison to the radial expansion. When α increases, the shape of the cavity deforms along

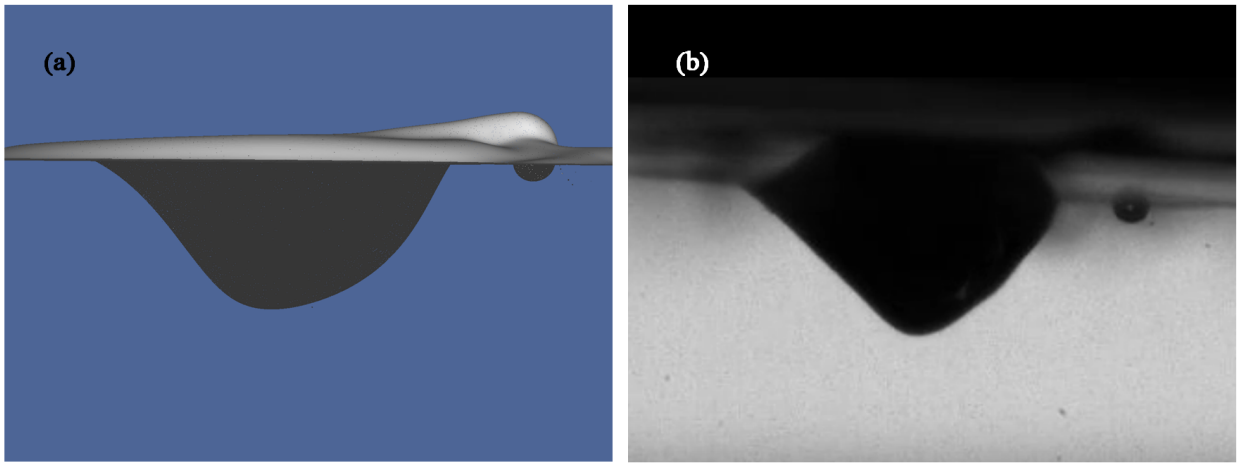

Figure 5.18: Images from our simulations (panel **(a)**) and the experiment taken from [89] (panel **(b)**). **(a):** Cavity shape of case with $We = 400, Re = 1000, \alpha_c = 60°$. We record the instant when the cavity is in saturation-period ($t^* = 7.8$). **(b):** The cavity observed in the experiment with $We = 474, Re = 2054, \alpha_c = 57°$ when $t^* \approx 7.8$. We notice that for a large impact angle, the cavity will be stretched in the direction parallel to the surface, resulting in a cone-shaped geometry.

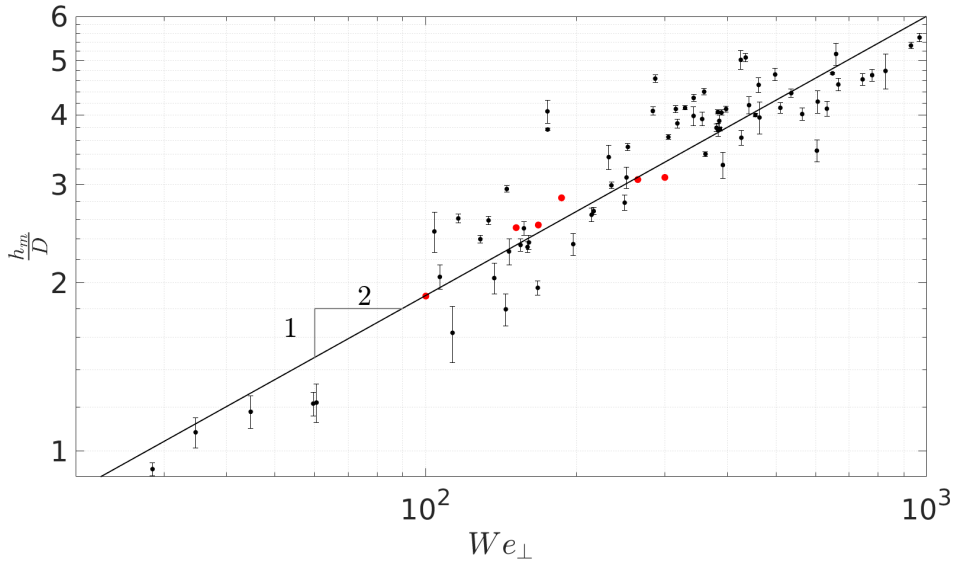

Figure 5.19: Double logarithmic plot of maximum cavity depth h_m (scaled by the droplet diameter D) as a function of $We_\perp$. The solid line has a slope of 1/2 with a prefactor of 0.19. We present the simulation results (red dots) and the experimental data from [71] (black dots) with the corresponding error bars.

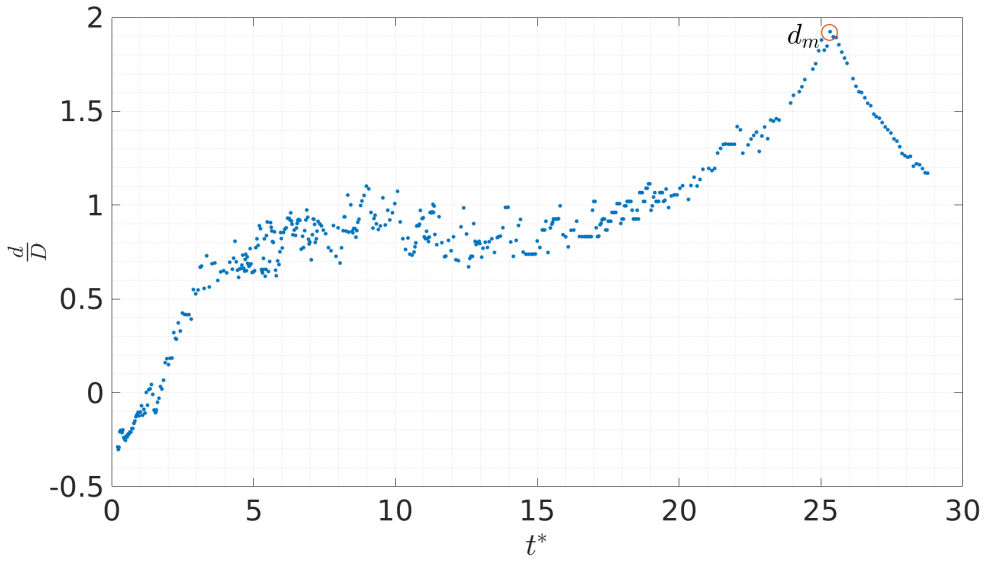

Figure 5.20: Cavity displacement d (scaled by the droplet diameter D) as a function of t^*. $We = 250, \alpha = 30°$. The cavity displacement increases rapidly in a short time period, and approaches to a static status (i.e., $\dot{d} \to 0$). Due the capillary waves traveling to the cavity bottom, the cavity displacement increase, reaching to d_m when the capillary waves collapse.

the parallel direction. In the simulations, an oscillation accompanies the data on the temporal function $d(t)$, while we do observe that $\dot{d} \to 0$ in a short period, followed by an abrupt increase as a result of the capillary waves, see Fig. 5.20. This noise on the data comes from our algorithm tracing the deepest point, for which we capture the coordinate of the cell center instead of the interface. Our implementation simplifies the simulation with a relatively small working load, while an oscillation will appears due to the dynamics refinement near the cavity bottom.

As defined in § 2.3.1, we record the cavity displacement d_m when the capillary waves collapse at the cavity bottom. By using the energy argument (2.23), we expect that d_m scales as $We_{\parallel}^{1/2}$ where $We_{\parallel} = \frac{\rho_l D U_{\parallel}^2}{\gamma}$. Fig. 5.21 shows the comparison between the experiments from [71] and the numerical results, from which an agreement is visible in terms of magnitude of d_m/D and the scaling law.

5.5 Initiation of the Cavity Collapse

As shown in Fig. 5.6 and Fig. 5.7, our simulations capture a liquid bump developed on the trailing side of the crater. Besides, a capillary wave traveling from the trailing side toward the cavity bottom is visible during the impact, see Fig. 5.13. Further analysis indicates a causal connection between the descent of this liquid bump and the capillary wave traveling on the cavity surface which finally leads to the collapse. Based on the slice figures along the symmetry plane, we can observe the evolution of the interface profile, see Fig. 5.22, where $\alpha = 35°$ and $We = 250$.

As presented in Fig. 5.22a, the last droplet attaches from the crown, and a liquid bump is observed (Fig. 5.22b). Due to a lack of kinetic energy, this liquid bump will be pulled back to the pool by the capillary force, see Fig. 5.22c, Fig. 5.22d. The descent of the crown triggers a capillary wave which will travel to the bottom of the cavity, see Fig. 5.22e.

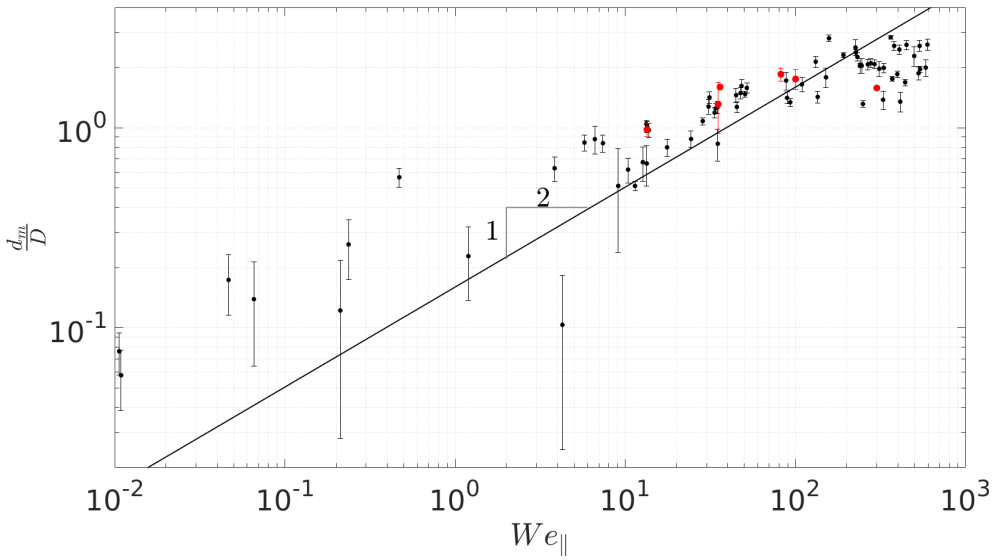

Figure 5.21: Double logarithmic plot of d_m (scaled by the droplet diameter D) as a function of $We_\parallel$. The solid line has a slope of 1/2 with a prefactor of 0.16. We present the simulation results (red dots) and the experimental data from [71] (black dots) with the corresponding error bars.

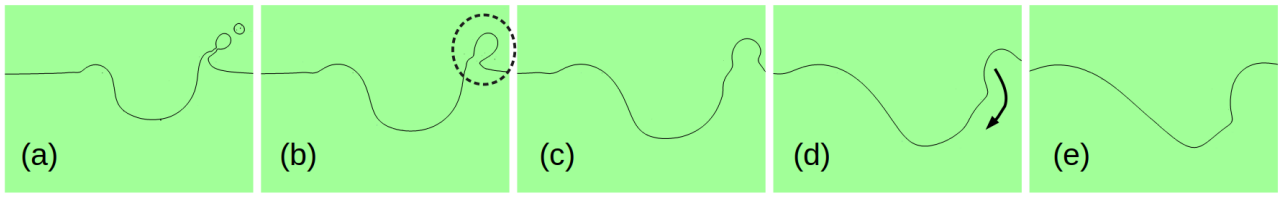

Figure 5.22: Slice snapshots interpreting the connection between the crown and the capillary wave. Figure is taken at the symmetry plane, i.e. $y-z$ plane in Fig. 5.1. The presented impact has $We = 250$ and $\alpha = 35°$. **(a):** The last droplet detaches from the crown. **(b):** A distinct liquid bump indicated by a dashed circle is visible. **(c):** Without enough velocity, this liquid bump will be pulled back to the pool by the capillary force. **(d):** The descent of the crown triggers a capillary wave on trailing side of the cavity, highlighted by an arrow. **(e):** This capillary wave travels toward the cavity bottom.

5.6 Conclusion

In this chapter, we presented the numerical results of oblique droplet impact onto a deep liquid pool. We performed simulations with $We \in [187.5, 1400]$ and $\alpha \in [0°, 75°]$. In the analysis, we focused on the crown behavior, the cavity angle, and the dimensions of the cavity. We quantified the numerical results and compared them with the experiments in [71].

In the simulations, we observed three distinct phenomena for the crown: deposition, single-sided splashing and the omni-directional splashing, which is consistent with [71]. The comparison between the crown phenomena observed in the simulations and the experiments shows an impressive agreement. Furthermore, we quantified the crown behavior into a phase diagram, from which it was concluded that our simulations captured transition of the crown as predicted by the threshold developed in [71]. Besides, we plotted the numerical and the experimental data into a phase diagram of $We^{1/2}Re^{1/4}K^{-1}$ and α, and yet again, we obtained an agreement in the comparison.

As for the cavity geometry, it is defined by three parameters: the cavity depth h, displacement d and the cavity angle α_c. We observed that cavity angle increases from $\alpha_c < 90°$ to $\alpha_c > 90°$ as the cavity developed. Our simulation captured this evolution, which is represented by α_c as a function of time. The growth of the cavity angle consists of three processes: inertial-growth, saturation-period and capillary-retraction, which are divided by two local maxima: inertial angle α_i and the collapse angle α_{cm}. One of our interests lies in the connection between the impact angle α and the collapse angle α_{cm} (i.e. the cavity angle when the capillary waves meet at the bottom of the crater). Our simulation indicated that $\alpha_{cm} \approx \alpha + 90°$ for small impact angle, while $\alpha_{cm} < \alpha + 90°$ when $\alpha \gtrapprox 35°$. Both the linear relation and the deviation between α and α_{cm} have been observed in the experiments [71].

By analogy with the model for the perpendicular impact, we approximated the cavity shape by an expansion hemisphere.

As a consequence, we obtained a temporal function for the cavity depth $h(t)$, which is in agreement with our simulations for $\alpha \in [0^\circ, 40^\circ]$. When the impact angle continuously increases, we observed a deviation between our data and the function $h(t)$. This phenomenon could come from the fact that the cavity will be stretched parallel to the surface with a larger impact angle. Hence the assumption of a hemispherical shape for the cavity is not valid anymore. The numerical data of the maximum cavity depth h_m shows a dependence on the perpendicular Weber number. Finally, we presented data for the cavity displacement $d(t)$, and its value when the waves collapse at the cavity bottom, i.e. d_m. The data shows a scaling law between d_m and the parallel Weber number. The magnitude of h_m and d_m show a good agreement with the experimental data in [71]

In conclusion, we made an effort for the numerical study of oblique droplet impact onto a deep liquid pool. The fully three-dimensional setting, which is applied to this problem for the first time offers details of the crown behavior and the cavity formation. Both quantitative and qualitative comparison between the numerical results and the experiments verify the validity of the simulation.

CHAPTER 6

Conclusion and Outlook

Oblique droplet impact on a deep liquid pool has been numerically studied in this thesis. The work is inspired by the ASML EUV source chamber in which a liquid tin droplet is put into motion by a pulsed laser. Consequently, a violent deformation and splashing would occur. To prevent the splashing contaminating the collector mirror and the intermediate focus, ASML is trying to add internal vanes to block these small drops. The liquid film coated by the initial splashing (on the surface of the vanes) can be regarded as a deep liquid pool in comparison to the droplets impact on the vanes. Therefore, the phenomenon of oblique impact onto the deep pool is critical to an intelligent design for the vanes.

The flow in our work, which is governed by the two-phase Navier-Stokes equations, was simulated using Basilisk, an open source package for CFD. As discussed in chapter 3, we used volume-of-fluid scheme coupled with an adaptive Cartesian grid to capture the interface. To support the numerical methods we opted, two validations were programmed and simulated: perpendicular droplet impact on a liquid/solid-substrate. We carried out these validations with an axisymmetric geometry in chapter 4. For a droplet impact on the solid substrate, we focused on the spreading process, from which we recorded the maximum spreading diameter D^*. As for the impact on a liquid pool, we determined the maximum cavity depth h_m. The numerical data of D^* and h_m are compared with the literature reviewed in chapter 2. To conclude, an agreement was observed in validations, which verified the capability of Basilisk to handle the droplet impact problem. However, the scalability analysis suggests a long running time and a tremendous memory consumption, which has set a bound for the number of the simulations and the resolution we could perform. In chapter 5, we presented the details of the simulation for oblique impact performed in a fully three-dimensional domain. The impact angle and the Weber number were changed systematically in $We \in [187.5, 1400]$ and $\alpha \in [0°, 75°]$ to capture the different crown behavior and the cavity formation. We compared the numerical results with the experiments of [71], from which an agreement has been observed. Our measurements were consistent with the splashing threshold theoretically modeled in [71]. Due to the connection between the Worthington jet and collapse angle α_{cm} [71], we have studied the dependence of α_{cm} on the impact angle α. Besides, the cavity geometry and its dimensions (i.e. the cavity depth and displacement) concerning both qualitative phenomena and quantitative magnitude have been accurately reproduced in the simulation.

Our work allows a prediction for the crown behavior with the parameters uncovered by the experiments. The crown phase for $We > 1000$, for example, has been provided in the thsis, while in the experiment, the upper bound of Weber number (i.e. $We \approx 1000$ in [71]) is set by the maximal flow rate of apparatus to produce the drops. We recommend simulating more cases to provide a more detailed and accurate phase diagram regarding the significance of the crown splashing to the design of the vanes in the EUV chamber. When predicting the transition from omni-directional to single-sided splashing, the threshold developed in [71] deviates from the experiments. Meanwhile, an overlap area between all three crown behaviors is observed near the intersection point of the threshold (i.e. $We^{1/2}Re^{1/4}K^{-1} = 1, \alpha = 0°$). The deviation could be caused by, for example, the camera resolution or the observation plane taken in the experiment which complicate the judgment on the impact behavior. Instead, our simulation offered a three-dimensional profile for the impact phenomenon, which allows a more clear judgment on the splashing transition. Although we have quantified several data for the crown behavior which are in agreement with the threshold near the intersection point, the amount of the simulations within this zone was limited by the undesirable scalability. Our simulation could support a further research into the effect of the surrounding environment on the crown behavior, such as the change of the vapor pressure which is hard to implement in the laboratory. In addition,

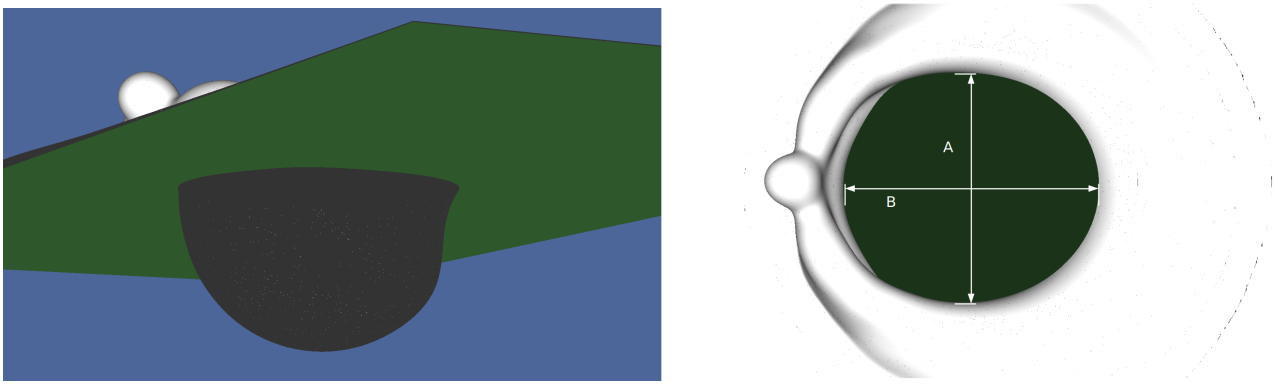

(a) **(b)**

Figure 6.1: Schematically plot of the recommended measurement from the top-view of the crater. **(a):** The cavity is cut by the initial surface of the pool (indicated by a green-colored plane). The view is set below the surface. **(b):** The top-view of the crater. A cross-section is visible accounting for the intersection line between the initial surface and the lateral wall of the cavity. We suggest measuring the dimensions A, B, and analyzing the impact parameters dependence of, e.g., A, B and the ratio A/B.

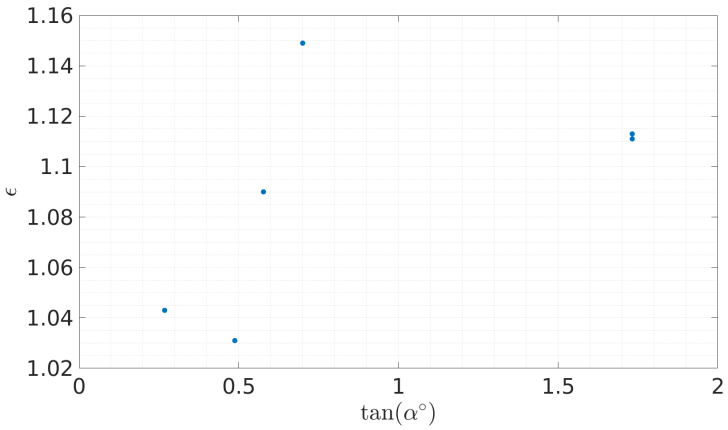

Figure 6.2: Plot of ϵ as a function of $\tan(\alpha)$ when $t/t_\gamma = 1$. The numerical result suggests that the cavity is stretched along the direction of the impact when we increase α. While the connection between the geometrical properties and, for example, the Weber number, is still not clear.

from the simulation we could extract the velocity magnitude of the crown, from which a direct validation on the splashing threshold in [71] could be carried out. Our study indicates that the capillary waves below the surface are triggered by the descent of the crown. It would be interesting to have a further research on the timescale when the capillary waves are initialized by the crown. Given the limited time available for this thesis, most of our simulations haven't reached the collapse moment. Hence the question about the Worthington jet which is one of the major concerns of ASML could not be directly answered in our work. We hereby recommend a further study on the characteristics of the jet, such as the velocity and its direction.

As for the cavity formation, we were able to present the information which is not available in the experiments. The cavity angle evolution, for example, was illustrated in the thesis. From the growth of the cavity angle we obtained three different regimes, where the competition between the inertial force and the surface tension is revealed. We also captured the growth of the cavity depth which has not been recorded in the experiment. We would recommend a further research on the top-view of the cavity that offers the crater dimensions parallel to the water surface. We suggest an analysis concerning the geometry of the cross section of the cavity cut by the initial surface, see Fig. 6.1. This measurement is hard to carried out in the experiment due to, for example, the transparency of the water surface and the setting of the cameras. Actually, during the project we have extracted the data of dimensions A, B and $\epsilon = B/A$ for several different cases when $t/t_\gamma = 1$. Fig. 6.2 shows ϵ as a function of $\tan(\alpha)$. We do observe an growing trend of ϵ when we increase the impact angle α. However, we still lack knowledge or the theoretical model to support the results. It would also be interesting to track the evolution of these parallel dimensions, i.e. $A(t/t_\gamma), B(t/t_\gamma)$ and $\epsilon(t/t_\gamma)$.

In our thesis, a sensitivity analysis to the resolution has been done in the present study, which is concluded with a maximum mesh level 12 (i.e. resolution 4096^3) implemented regarding the computational resources available. It would be very interesting to run the simulation with a higher mesh density, from which a more clear convergence of the impact phenomena would be obtained. Besides the spatial resolution, numerical parameters (such as the converge criterion for the Poisson equation and the time discretization) would also affect the numerical results. For further research, a sensitivity study of the time step and the tolerance of the Poisson equation would enhance the credibility of the simulation. However, we emphasize that the sensitivity analysis to multiple parameters with a three-dimensional setting could be extremely expensive. Rather, we recommend carrying out the study in a two-dimensional domain.

Acknowledgement

"I'm convinced that the only thing that kept me going was that I loved what I did."

Steve Jobs

First of all, I want to thank my daily supervisor Sten Reijers for his guidance through the project. Without his help this thesis would not be completed. Sten helped me to go through the toughest period at the initial stage of the project, and put me on the correct tack with the subject that I have hardly any experience in before. During the project I have encountered so many obstacles and challenges such as the poor scalability of the simulations, the optimization of our algorithm accounting for the post process from a massive amounts of data, and yes, we took on the challenges and made it. Second, I want to expess my gratitude to Hanneke Gelderblom for her patient guidance. She help me to build a substantial theory on the subject, and, most important, inspired my motivation and passion on the study. I have seen all the outstanding properties for a scientific researcher: curiosity, motivations, and patience on her. Hanneke sets an example that I'm striving for in the future. Meanwhile, I would like to thank Wim-Paul Breugem for his organization on my defense and the Committee. I want to thank Marise Gielen, the author of the first experimental study on the same subject. The experimental material that you generously offered make the direct comparison available. It not frequently happens for a simulation guy who can work just beside the original author of the theoretical background. Also, your precious impute and suggestion are of great significance to my thesis. I want to thank Alexander Klein, not only for his input to my work, but also the help for me to get involved the home-like atmosphere of our group.

Since last summer, I moved from Delft to Eindhoven, a new city for me without any friend of mine. Fortunately, I had a chance to make an acquaintance with my new neighbour Zitong Lian and Tianyu Zhou, who have supported me in respect of my life. Besides, I express my appreciation to one of my best friend, my 'comrade-in-arms' on the study in the first year, Jinjun Li. I would not graduate and finish my study without his help. Most important, I want express my appreciation to my parents, who consistently support me throughout my whole studies, not only materially, but also mentally. Your understandings on my decisions are always the best supports in my life.

Finally, I want to thank myself for the things I have done. As said by Steve Jobs, I believe that passion and love to the work I have done are always the motivation that keeps me moving forward. For the last two years I have learned not only the academic knowledge, but also the target for the future, which, without a doubt, is more valuable for me at this point.

Bo Liu, August 2017

Bibliography

[1] Popinet, basilsik, http://basilisk.fr/

[2] Popinet, Gerris, http://gfs.sourceforge.net/wiki/index.php/Main_Page

[3] ASML, Performance and Targets, https://www.asml.com

[4] EUV source, Company ASML, https://www.cymer.com/euv-light-sources/

[5] Stability of Finite Difference Methods, chapter 14, http://web.mit.edu/16.90/BackUp/www/pdfs/Chapter14.pdf

[6] K. Sellegri, C. O'Dowd, Y. Yoon, S. Jennings, and G. de Leeuw, *Surfactants and submicron sea spray generation*, J. Geophys. Res. Atmos. 10.1029/2005JD006658 (2006).

[7] C. Peirce, C. Priest, T. McBeath, and M. McLaughlin, *Uptake of phosphorus from surfactant solutions by wheat leaves: spreading kinetics, wetted area, and drying time*, Soft Matter, 12, 209 (2016).

[8] B. Gopalan and J. Katz, *Turbulent Shearing of Crude Oil Mixed with Dispersant Generates Long Mi- crothreads and Micro-droplets*, Phys. Rev. Lett. 104, 054501 (2010).

[9] S. D. Aziz and S. Chandra, *Impact, recoil and splashing of molten metal droplets*, Int. J. Heat Mass Transfer, 43, 2841 (2000).

[10] A. van der Bos, M. J. van der Meulen, T. Driessen, M. vander Berg, H. Reinten, H. Wijshoff, M. Versluis, and D. Lohse, *Velocity Profile inside Piezoacoustic Inkjet Droplets in Flight: Comparison between Experiment and Numerical Simulation*, Phys. Rev. Appl. 1, 014004 (2014).

[11] Tomio Okawa, *Numerical Simulation of Single Drop Impingement onto a Plane Liquid Surface*, ILASS (2008).

[12] Z. H. Xie, G. F. Hewitt, D. Pavlidis, P. Salinas, C. C. Pain and O. K. Matar, *Numerical study of three-dimensional droplet impact on a flowing liquid film in annular two-phase flow*, Chem. Eng. Sci. 166, 303-312 (2017).

[13] P. Brambilla, A. Guardone, *Assessment of dynamic adaptive grids in Volume-Of-Fluid simulations of oblique drop impacts onto liquid films*, J. Comput. Appl. Math., 281:277-283 (2015).

[14] P. Linz and R. Wang, *Exploring Numerical Methods: An Introduction To Scientific Computing Using MATLAB*, 1st Edition, Jones and Bartlett Publisher (2002).

[15] Charles Hirsch, *Numerical Computation of Internal and External Flows*, 2nd Edition, Butterworth-Heinemann (2007)

[16] F.H. Harlow and J.E. Welch, *Numerical Calculation of Time-Dependent Viscous Incompressible Flow of Fluid with Free Surface*, Phys. Fluids, 8, 2182-2189 (1965).

[17] A. J. Chroin, *Numerical solution of the Navier-Stokes equations*, Math. compute. 23, 341-54 (1968).

[18] R. Temam, *Navier-Stokes Equation*, North-Holland, Amsterdam (1977).

[19] W. F. Noh and P. Woodward, *SLIC (Simple Line Interface Calculation)*. 5th International Conference of Fluid Dynamics, Springer, Berlin, Heidelberg (1976).

[20] H. T. Ahn and M. Shashkov, *Geometric Algorithms for 3D Interface Reconstruction*, Proceedings of the 16th International Meshing Roundtable, 405-422 (2008).

[21] A. Worthington, *A study of splashes*, Longmans, Green, and Co. (1908).

[22] O. G.Engel. *Crater Depth in Fluid Impacts*, J. Community Appl. Soc. 37 (1965).

[23] C. Josserand and S.T. Thoroddsen, *Drop Impact on a Solid Surface*, Annu. Rev. Fluid Mech. 48:365–91 (2016).

[24] T. Tran, H. De Maleprade, C. Sun, and D. Lohse, *Air entrainment during impact of droplets on liquid surfaces*, Fluid Mech, 726, R3 (2013).

[25] Clanet C, Beguin C, Richard D, Quere D, *Maximal deformation of an impacting drop*, Fluid Mech, 517:199-208 (2004).

[26] G. J. Michon, C. Josserand, and T. Seon, *Jet dynamics post drop impact on a deep pool*, Phys. Rev. Fluids, 2, 023601 (2017).

[27] D. Brutin, *Drop impingement on a deep liquid surface: study of a crater's sinking dynamics*,

[28] A. I. Fedorchenko and A. B. Wang, *On some common features of drop impact on liquid surfaces*, Phys. Fluids, 16 (2004).

[29] A. Bisighini and G. E. Cossali. *Crater evolution after the impact of a drop onto a semi-infinite liquid target*, Phys. Rev. 82, (2010).

[30] S. Osher and J. A. Sethian, *Fronts Propagating with Curvature Dependent Speed: Algorithms Based on Hamilton-Jacobi Formulations*, J. Compute. Phys. 79, 12-49 (1988).

[31] B. Ray, G. Biswas and A. Sharma, *Bubble pinch-off and scaling during liquid drop impact on liquid pool*, Phys. Fluids, 768 (2015).

[32] S. Wildeman, C. W. Visser, C. Sun and Detlef. *On the spreading of impacting drops*, under consideration for publication in J. Fluid Mech. (2016).

[33] I. V. Roisman, *Inertia dominated drop collisions. II. An analytical solution of the Navier–Stokes equations for a spreading viscous film*, Phys. Fluids, 21, 052103-052104 (2009).

[34] J. Philippi, P. Y. Largee, and A. Antkowiak, *Droplet impact on the solid surface: short time self-simularity*, J. Fluid Mech. 795, 96-135 (2016).

[35] J. Eggers, M. Fontelos, C. Josserand and S. Zaleski, *Drop dynamics after impact on a solid wall: theory and simulations*, Phys. Fluids, 22:062101 (2010).

[36] C. W. Visser, P. E. Frommhold, S. Wildeman, R. Mettin, D. Lohse and C. Sun. *Dynamics of high-speed micro-drop impact: numerical simulations and experiments at frame-to-frame times below 100 ns*, Soft Matter, 11, 1708 (2015).

[37] C. Josserand, P. Ray, and S. Zaleski, *Droplet impact on a thin liquid film: anatomy of the splash*, Phys. Fluids, 15, 1650 (2003).

[38] S. T. Thoroddsen, *The ejecta sheet generated by the impact of a drop*, J. Fluid Mech. 451, 373-381 (2002).

[39] E. Villermaux and C. Clanet, *Life of a flapping liquid sheet*, J. Fluid Mech. 462, 341-363 (2002).

[40] M. Ali, A. Umemura and M. Q. Islam, *A Numerical Investigation on Dynamics and Breakup of Liquid Sheet*, J. Fluids Eng. 134(10), 101303 (2012).

[41] D. L. Chubb and F. D. Calfo, *A study of thin liquid flow*, NASA Technical Memorandum 106323 (1993).

[42] C. D. Stow, M. G. Hadfield, *Experimental Investigation of Fluid Flow Resulting from the Impact of a Water Drop with an Unyielding Dry Surface*, Proceedings of the Royal Society of London A: Mathematical, Physical and Engineering Sciences 373, 419 (1981).

[43] C. Mundo, M. Sommerfeld and C. Tropea, *Droplet-wall collisions: Experimental studies of the deformation and breakup process*, Int. J. Multiph. Flow. 706, 560 (1995).

[44] H. Zhao, A.Brunsvold and S. T. Munkejord, *Investigation of droplets impinging on a deep pool: Transition from coalescence to jetting*, Exp Fluids. 50:621-635 (2011).

[45] E. C. Orozco, A. Davanlou, P. K. Choudhury, and R. Kumar, *Droplet impact on deep liquid pools: Rayleigh jet to formation of secondary droplets*, Phys. Rev. E 92, 053022 (2015).

[46] R. D. Deegan, P. Brunet and J. Eggers, *Complexities of Splashing*, Nonlinearity, 21, C1 (2008).

[47] M. Hsiao, S. Lichter and L. G. Quintero, *The critical Weber number for vortex and jet formation for drops impinging on a liquid pool*, Phys. Fluids 31, 3560–3562 (1988).

[48] Q. Y. Huang, and H. Zhang, *A study of different fluid droplets impacting on the liquid film*, Pet. Sci. Technol. 5:62-66 (2008).

[49] M. Cheng and J. Lou, *A numerical study on splash of oblique drop impact on wet walls*, Comput. Fluids, 115, 11 (2015)

[50] A. L. Biance, C. Clanet and D. Quere, *First steps in the spreading of a liquid droplet*, Phys. Rev. 69, 016301 (2004).

[51] E. Berberović, N. P. van Hinsberg, S. Jakirlić, Ilia V. Roisman and C. Tropea, *Drop impact onto a liquid layer of finite thickness: Dynamics of the cavity evolution*, Phys. Fluids 79, 036306 (2009).

[52] O. G. Engel, *Initial Pressure, Initial Flow Velocity, and the Time Dependence of Crater Depth in Fluid Impacts*, J. Appl. Phys. 38, 3935 (1967).

[53] H. N. Oguz and A. Prosperetti, *Bubble entrainment by the impact of drops on liquid surfaces*, J. Fluid Mech. 219, 143 (1990).

[54] J. L. Liow, *Splash formation by spherical drops*, J. Fluid Mech. 427, 73 (2001).

[55] N. Bremond, C. Clanet and E. Villermaux, *Atomization of undulating liquid sheets*, J. Fluid Mech. 585, 421-456 (2007).

[56] S.X. Xu and W.Q. Ren, *Reinitialization of the Level-Set Function in 3d Simulation of Moving Contact Lines*, J. Commun. Compute. Phys. 20, pp1163-1182 (2016).

[57] C. W. Hirt and B. D. Nichols. *Volume of fluid method for the dynamics of free boundaries*, J. Compute. Phys. 39(1):201–225 (1981).

[58] G.K. Karch, F. Sadlo, C. Meister, P. Rauschenberger, K. Eisenschmidt, B. Weigand and T. Ertl, *Visualization of Picewise Linear Interface Calculation*, IEEE Pacific Visualisation Symposium (2013).

[59] E. Aulisa, S. Manservisi, R. Scardovelli and S. Zaleski, *Interface reconstruction with least-squares fit and split advection in three-dimensional Cartesian geometry*, J. Comput. Phys. 225, 2301-2319 (2006).

[60] M. Rudman, *Volume-tracking methods for interfacial flow calculations*, Int. J. Numer. Methods Fluids 24 (7) 671–691 (1997).

[61] M. Owkes, O. Desjardins, *A computational framework for conservative, three-dimensional, unsplit, geometric transport with application to the volume-of-fluid (VOF) method*, J. Compute. Phys. 270 (2014) 587–612 (2014).

[62] R. Scardovelli and S. Zaleski. *Direct numerical simulation of free-surface and interfacial flow*, Annu. Rev. Fluid Mech. 31:567–603 (1999).

[63] G. Amdahl, *Validity of the Single-Processor Approach to Achieving Large-Scale Computing Capabilities*, Proc. AFIPS Conf. 483 (1967)

[64] K. Yokoi, D. Vadillo, J. Hinch and I. Hutchings, *Numerical studies of the influence of the dynamic contact angle on a droplet impacting on a dry surface*, Phys. Fluids, 21, 072102 (2009).

[65] U. Ziegler, *Blocked-Structured Adaptive Mesh Refinement on Curvilinear-orthogonal Grids*. J. Sci. Comput. 34, 102-121 (2012).

[66] A. Cohen,*Adaptive Methods for PDE's Wavelets or Mesh Refinement*, Vol.I 607-620 (2002).

[67] R. Glowinski, J. Periaux, M. Ravachol, T. W. Pan, R. O. Wells and X. Zhou,*Wavelet Method in Computational Fluid Dynamics*, Algorithmic Trends in Computational, 259-276 (1993)

[68] D. L. Yong, *Time-dependent multi-material flow with large fluid distribution*, in Numerical methods for fluid dynamics, Morton and Norman,Editor,187-221 (1996

[69] D. Fuster, G.Agbaglah, C. Josserand, S. Popinet and S. Zaleski, *Numerical simulation of droplets, bubbles and waves: state of the art*, Fluid Dyn Res.41(6) (2009).

[70] Jason Z.X. Zheng, *Block-Based Adaptive Mesh Refinement Finite-Volume Scheme for Hybrid Multi-Block Meshes*, Master Theis, Univ. Toronto (2012).

[71] M. V. Gielen, P. Sleutel, J. Benschop, M. Riepen, V. Voronina, D. Lohse, J. H. Snoeijer, M. Versluis and H. Gelderblom, *Oblique Drop Impact onto a Deep Liquid Pool*, physics.flu-dyn, 61 (2016).

[72] S. Popinet, *An accurate adaptive solver for surface-tension-driven interfacial flow*, J. Comput Phys. 228 (16) (2009).

[73] S. Popinet, *Gerris: a tree-based adaptive solver for the incompressible Euler equations in complex geometrie*, J. Comput Phys.190(2) (2003).

[74] M. Sussman, A.S. Almgren, J.B. Bell, P. Colella, L.H. Howell, M.L. Welcome, An adaptive level set approach for incompressible two-phase flows, J. Comput. Phys. 148:81-124 (1999).

[75] G. Agresar, J.J. Linderman, G. Tryggvason, K.G. Powell,*An Adaptive, Cartesian, front-tracking methodd for the motion, deformation and adhesion of circulating cells*, J. Comput. Phys. 43:346-380 (1998).

[76] F. Gibou, L. Chen, D. Nguyen, S. Banerjee, *A level set based sharp interface method for the multiphase incompressible Navier–Stokes equations with phase change*, J. Comput. Phys. 222:536-555 (2007).

[77] R. Lebas, T. Menard, P.A. Beau, A. Berlemont, F.X. Demoulin, *Numerical simulation of primary break-up and atomization: DNS and modelling study*, Int.J. Multiphase Flow 35:247-260 (2009).

[78] G. Agbaglah, S. Delaux, D. Fuster, J. Hoepffner, C. Josserand, S.Popinet, P.Ray, R. Scardovelli and S.Zaleski, *Parallel simulation of multiphase flows using octree adaptivity and the volume-of-fluid method*, C. R. Mecanique 339, 194–207 (2011).

[79] M. J. Aftosmis, *Solution adaptive Cartesian grid methods for aerodynamic flows with complex geometries*, Conference:28th computational fluid dynamics (1997).

[80] B. Ray, G. Biswas and A. Sharma, *Drop Impact on Deep and Shallow Liquid*, Commun. Comput. Phys. 11, 1386-1396 (2012).

[81] G. I. Taylor, *The Dynamics of Thin Sheets of Fluid*, III. Disintegration of Fluid Sheets, Proceedings of the Royal Society of London, A253, 313-321 (1959).

[82] F. E. C. Culick, *Comments on a Ruptured Soap Film*, J Appl. Sci. 31, 1128-1129 (1960).

[83] L. E. Schwer, *Is your Mesh Refined Enough? Estimating Discretization Error using GCI*, LS-DYNA (2008).

[84] National Institute of Standards and Technology:`http://webbook.nist.gov/chemistry/fluid/`

[85] G. Leneweit, R. Koehler, K. G. Roesner and G. Schäfer, *Regimes of drop morphology in oblique impact on deep fluids*, J. Fluid Mech. 543:301-333 (2005).

[86] D. Bonn, J. Eggers, J. Indekeu, J. Meunier and E. Rolley, *Wetting and spreading*, Rev. Mod. Phys. 81, 739 (2009).

[87] C. Huh, and L. E. Scriven, *Hydrodynamic model of steady movement of a solid/liquid/fluid contact line*, J. Coll. Int. Sci. 35, 85 (1971).

[88] F. Batchelor, *An Introduction to Fluid Mechanics*, (Cambridge Universty Press, Cambridge, 1970).

[89] Private communication with M.V. Gielen and P. Sleutel

[90] H.Grosshans, A. Movaghar, L. Cao, M. Oevermann, R.-Z.Szász, and L. Fuchs, *Sensitivity of VOF simulations of the liquid jet breakup to physical and numerical parameters*, J. Comput. Fluids. 136:312-323 (2016).

[91] M. Gorokhovski, M. Herrmann, *Modeling primary atomization*, Annu. Rev. Fluid Mech. 40:343-366 (2008).

[92] G. Birkhoff, D. P. MacDougall, E. M. Pugh, and S. G. Taylor, *Explosive with Lines Cavities*, J. Appl. Phys. 19, 563 (1948).

[93] K. W. T. Christopher, *Computational Aeroacoustics: A Wave Number Approach*, Cambridge University press, Cambridge, UK (2012).